A Dissertation

entitled

Density Functional Theory and Accelerated Dynamics Studies of the Structural and Non-equilibrium Properties of Bulk Alloys and Thin-Films

by

Indiras Khatri

Submitted to the Graduate Faculty as partial fulfillment of the requirements for the Doctor of Philosophy Degree in Physics

Dr. Jacques G. Amar, Committee Chair

Dr. Bo Gao, Committee Member

Dr. Michael C. Cushing, Committee Member

Dr. Yanfa Yan, Committee Member

Dr. Glenn Lipscomb, Committee Member

Dr. Amy Thompson, Interim Dean
College of Graduate Studies

The University of Toledo
May 2022

An Abstract of

Density Functional Theory and Accelerated Dynamics Studies of the Structural and Non-equilibrium Properties of Bulk Alloys and Thin-Films

by

Indiras Khatri

Submitted to the Graduate Faculty as partial fulfillment of the requirements for the
Doctor of Philosophy Degree in Physics

The University of Toledo
May 2022

In this dissertation, the structural properties of bulk alloys and thin films are studied using a variety of different techniques including density functional theory (DFT) and accelerated dynamics. The first part of this dissertation involves the use of DFT calculations. In particular, in Chapter 3 the stability and mechanical properties of 3d transitional metal carbides in zincblende, rocksalt, and cesium chloride crystal structures are studied. We find that the valence electron concentration and bonding configuration control the stability of these compounds. The filled bonding states of transition metal carbides enable the stability of the compounds.

In the second part of this dissertation, we use a variety of accelerated dynamics techniques to understand the properties of growing and/or sublimating thin-films. In Chapter 4, the results of temperature-accelerated dynamics (TAD) simulations of the submonolayer growth of Cu on a biaxially strained Cu(100) substrate are presented. These simulations were carried out to understand the effects of compressive strain on the structure and morphology. For the case of 4% compressive strain, stacking fault formation was observed in good agreement with experiments on Cu/Ni(100) growth. The detailed kinetic and thermodynamic mechanisms for this transition are also explained. In contrast, for smaller (2%) compressive strain, the competition between island growth and multi-atom relaxation events was found to lead to an is-

land morphology with a mixture of open and closed steps. In Chapter 5, we then study the general dependence of the diffusion mechanisms and activation barriers for monomer and dimer diffusion as a function of strain. The results of TAD simulations of Cu/Cu(100) growth with 8% tensile strain are also presented. In this case, a new kinetic mechanism for the formation of anisotropic islands in the presence of isotropic diffusion was found and explained via the preference for monomer diffusion via exchange over hopping. In Chapter 6, we then study the early stages of CdTe thin-film deposition. In particular, molecular dynamics simulations based on a bond-order potential are used to investigate the dependence of the attachment probability and deposition site for Cd and Te_2 clusters deposited on Cd-terminated and Te-terminated (100) and (111) surfaces of zincblende CdTe on deposition angle, energy, and substrate temperature. In general, we find that the deposition of Cd atoms and/or Te_2 dimers on the oppositely terminated surface leads to an attachment probability that is close to 1 and relatively independent of deposition conditions. In contrast, deposition on the same terminated surface leads to a significantly lower attachment probability which generally decreases with increasing deposition angle, energy, and substrate temperature. Our results also indicate that vapor deposition on both the (100) and (111) surfaces, as well as sputter deposition on the (111) surface, leads to a significant excess Te sticking probability. In Chapter 7 we then use the same bond-order potential, along with two different accelerated dynamics methods - to study the process of CdTe sublimation, which is important in the deposition of CdTe thin-film solar cells. Our results explain the temperature-dependence of the experimentally observed activation energies and also elucidate the key mechanisms involved in CdTe(100) sublimation. An analysis of our results also leads to good agreement with experimental results for the total sublimation rate at high temperatures ($T > 360°C$). They also provide a possible explanation for the lower effective activation energy observed for $T < 360°C$. Finally, in Chapter 8 we summarize our results and discuss possible future work.

In addition to the first-author works [1–5] discussed in Chapters 3 - 7 of this dissertation, I am also a co-author on several additional publications [6–11] which have not been included in this dissertation.

This dissertation is dedicated to my family for their unending support and encouragement.

Acknowledgments

I would like to thank my supervisor, Prof. J.G. Amar, for invaluable advice, continuous support, and patience during my Ph.D. study. I have benefited greatly from his immense knowledge and meticulous editing.

I also want to express my gratitude to my committee members Dr. B. Gao, Dr. M. Cushing, Dr. Y. Yan, and Dr. G. Lipscomb for their encouraging words and feedback.

It is my great pleasure to acknowledge all the faculty and staff at the Department of Physics and Astronomy for their support.

I would also like to thank the National Science Foundation and Air Force Research Laboratories, as well as the Ohio Supercomputer Center for their support.

Finally, I would like to thank my wife, Tika D. Khatiwada, and my family for their tremendous support and encouragement to complete my Ph.D. degree.

Contents

List of Tables

List of Figures

List of Abbreviations

COHP	Crystal Orbital Hamiltonian Population
CdTe	Cadmium Telluride
CsCl	Cesium Chloride
DFT	Density Functional Theory
DS	Dynamically Stable
DU	Dynamically UnStable
EAM	Embedded Atom Method
GGA	Generalized Gradient Approximation
ipCOHP	Integrated Projected Crystal Orbital Hamiltonian Population
LAMMPS	Large-scale Atomic Molecular Massively Parallel Simulator
LDA	Local Density Approximation
MD	Molecular Dynamics)
MS	Mechanically Stable
MU	Mechanically Unstable
NEB	Nudged Elastic Band
PDOS	Projected Density of States
RS	Rocksalt
TAD	Temperature Accelerated Dynamics’
TMC	Transition Metal Carbide
TST	Transition State Theory
VASP	Vienna Ab initio Simulation Package
ZB	Zincblende

List of Symbols

$\frac{\partial}{\partial t}$	Partial derivative with respect to time
ϕ	Wave function
$\boldsymbol{\nabla}$	Vector differential operator
Δ	Difference Operator
$\boldsymbol{\xi}$	Random variable
$\sum_{i=1}^{N}$	Sum from 1 to N
$\int d^3r$	Integration with respect to r
$< ... >$	time-averaged quantity
$O(\Delta x^4)$	Fourth order of change in x

Chapter 1

Introduction

The properties of metal alloys and thin films have attracted significant interest due to their use in a variety of applications including solar cells, optoelectronic devices, thermoelectric devices, hard coatings, computer components, and biomedical devices. In this dissertation, we present the results of our computational explorations of the properties of bulk alloys and thin films. The benefit of these studies is that they allow us to gain a better understanding of key atomic and nanoscale properties such as defect structure, vacancies, dynamic behavior, and stability which cannot be easily obtained directly from experiments. In addition, the ability to control the key parameters in our simulations allows us to obtain a fundamental understanding of the effects of individual parameters on their properties.

This dissertation is organized as follows. In Chapter 2, we first give a brief introduction of the methodologies used in our calculations. This includes a discussion of the density functional theory (DFT) method as well as of the molecular dynamics (MD) and temperature accelerated dynamics (TAD) methods. A brief discussion of the empirical potentials used in our MD and TAD simulations is also included. In Chapter 3, we then present the results of DFT calculations which we have carried out to understand the relative stability and mechanical properties of 3d transitional metal carbides in the rocksalt, zincblende, and cesium chloride structures [2]. We find that the valence electron concentration and bonding configuration control the stability of these compounds while the filled bonding states of transition metal carbides enable the stability of the compounds.

In Chapter 4 the results of TAD simulations which were carried out to study the effects of biaxial compressive strain on Cu/Cu(100) submonolayer growth are presented. We find that in the presence of 4% compressive strain the formation of submonolayer islands leads to substrate vacancies which in turn promote the formation of stacking faults. Interestingly, while we find that the activation barrier for stacking fault formation is quite large, the prefactor is also very large due to the large increase in entropy [1]. In Chapter 5, we continue to discuss the effects of strain in Cu/Cu(100) growth with a focus on the submonolayer island morphology. For the case of smaller (2%) compressive strain, we find that multi-atom pop-out events lead to irregular island shapes which are similar to those observed in Cu/Ni(100) submonolayer growth. In addition, in the case of very large (8%) tensile strain, we find that the preference for monomer diffusion via exchange over hopping leads to a new kinetic mechanism for the formation of strongly anisotropic islands [4]. In Chapter 6, we then study the early stages of CdTe thin-film deposition. In particular, we present results for the dependence of the Cd and Te_2 sticking probabilities and attachment sites on kinetic energy, substrate temperature, and deposition angle for the Cd- and Te-terminated (100) and (111) surfaces [5]. In Chapter 7, we then present the results of accelerated molecular dynamics simulations which were carried out in order to understand the mechanisms and kinetics of CdTe(100) sublimation [3]. We note that this is of technological interest since close-spaced sublimation is one of the leading methods to produce CdTe thin-films in solar cells. We find that Cd vacancy nucleation and growth is the rate-limiting step for sublimation at high temperature ($T > 360^o$ C) while our results are also in good agreement with experiments over this temperature range.

A possible low-barrier desorption pathway is also presented which may explain the lower value of the activation energy obtained experimentally at low temperature. Finally, in Chapter 8, we summarize our results and discuss possible future work.

Chapter 2

Methodology

2.1 Density Functional Theory

2.1.1 The Schrödinger equation

Obtaining the solution of the time-independent Schrödinger equation [20] for a many-body system which includes both ions (nuclei) and electrons in a crystal is a difficult problem. However, in many cases the Oppenheimer approximation [21], in which the nuclei are considered to be fixed, can be used. In this case, the corresponding Schrödinger equation for the electrons may be written,

$$\left[\frac{-\hbar^2}{2m}\sum_{i=1}^{N}\nabla_i^2+\sum_{i,j=1}^{N}V(|\mathbf{r}_i-\mathbf{R}_j)|)+\sum_{i<j}U(\mathbf{r}_i,\mathbf{r}_j)\right]\phi(\{\mathbf{r_i}\})=E\phi(\{\mathbf{r_i}\}) \tag{2.1}$$

where $\mathbf{r_i}$ is the position of electron i, $\mathbf{R_j}$ is the position of ion j and $\phi(\{\mathbf{r_i}\})$ is the many-electron wavefunction. In equation 2.1, the first term on the left is the kinetic energy operator, the second term corresponds to the attractive Coulomb interaction between electrons and ions, and the third term corresponds to the repulsive electron-electron Coulomb interaction. DFT provides a relatively inexpensive computational method to obtain an accurate solution for such crystal properties as the ground-state energies and forces as well as the band-structure.

2.1.2 The basic foundation of DFT

The density functional theory (DFT) method is based on the assumption that the energy of a system is a unique functional of the overall electron-density function,

$$n(\mathbf{r}) = \sum_i \phi_i^*(\mathbf{r})\phi_i(\mathbf{r}) \tag{2.2}$$

and $\phi_i^*(r)$ is the complex conjugate of $\phi_i(\mathbf{r})$. The basis of the DFT based on two theorems [22]

Theorem I. *For any system of interacting electrons in an external potential, the ground state energy is a unique function of the ground state electron density* $n_0(\mathbf{r})$.
Theorem II: *A universal functional* $E_\nu[n(\mathbf{r})]$ *that defines the energy of a system in a given potential V(r) can be defined strictly in terms of the above-mentioned electron density n(r). The global minimum value of this energy functional corresponds to the true ground state density,* $n_0(r)$.

2.1.3 The Kohn-Sham equations

With the help of the electron density n($\mathbf{r}$), the Schrödinger equation from equation 2.1 can be transformed to the Kohn-Sham equation [23], where the single-electron wavefunctions $\phi_i(\mathbf{r})$ can be found by solving,

$$\left[-\frac{\hbar^2}{2m}\nabla^2 + V(\mathbf{r}) + V_H(\mathbf{r}) + V_{xc}(\mathbf{r})\right]\phi_i(\mathbf{r}) = \epsilon_i\phi_i(\mathbf{r}) \tag{2.3}$$

where V($\mathbf{r}$) is the ionic potential and $V_H(\mathbf{r})$ and $V_{xc}(\mathbf{r})$ are the Hartree and exchange-correlation potentials respectively which can be expressed as:

$$V_H(\mathbf{r}) = e^2 \int \frac{n(\mathbf{r}')}{|\mathbf{r} - \mathbf{r}'|} d^3\mathbf{r}' \tag{2.4}$$

$$V_{xc}(\mathbf{r}) = \frac{\delta E_{xc}[n(\mathbf{r})]}{\delta n(\mathbf{r})} \tag{2.5}$$

while $E_{xc}[n(\mathbf{r})]$ is unknown and needs to be approximated.

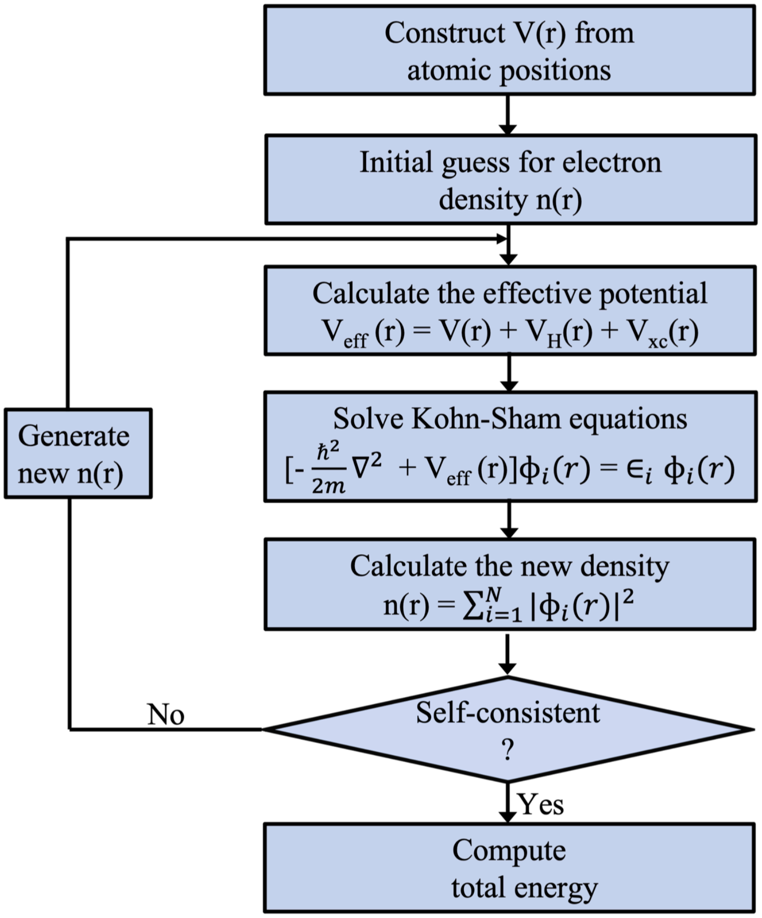

Figure 2-1: Iterative procedure of solving the Kohn-Sham equation. Adopted from Payne *et al.* [13].

The approach of solving the Kohn-Sham equation numerically is illustrated by Fig 2-1. With an initial guess for the electron density n($\mathbf{r}$), one can construct the effective potential $V_{eff}(\mathbf{r})$ and obtain the single-electron wave functions $\phi_i(r)$ by solving the Kohn-Sham equation. A new electron density from equation 2.2 based on the wave functions is found and is then used as a new trial density. The procedure is then repeated until the new density is numerically equal to the old one and the ground-state electron density $n_0(\mathbf{r})$ and energy are obtained.

2.1.4 The electronic exchange-correlation functional

As mentioned earlier, the exchange-correlation function is not precisely known and needs to be approximated. The simplest approximation is the Local Density Approximation (LDA) [24] in which the exchange-correlation energy per atom is similar to that of a homogeneous electron gas with the same density, i.e.

$$V_{xc}(n) = V_{xc}^{electrongas}[n]. \tag{2.6}$$

A commonly used and ofter more accurate approximation for the exchange-correlation energy is the Generalized Gradient Approximation (GGA). This approximation takes into account both the density and the gradient of the density, i.e.

$$E_{xc}^{GGA} = \int f((n(\mathbf{r})), \nabla n(\mathbf{r}))d^3r \tag{2.7}$$

Two popular versions of the GGA approximation are the PW91 scheme by Perdew and Wang [25, 26] and the PBE scheme by Perdew, Burke and Ernzerhof [27]. In our DFT calculations we have used the popular PBE scheme along with the code package Vienna Ab initio Simulation Package (VASP) [28–32]. The technical details and parameters used are discussed in Chapter 3.

2.2 Molecular Dynamics

In the molecular dynamics (MD) simulation method, Newton's equations of motion:

$$\mathbf{F}_i = m_i\mathbf{a}_i, \tag{2.8}$$

are used to determine the positions and velocities of a set of atoms i as a function of time. Here $\mathbf{F}_i$ is the force exerted on atom i due to its interaction with other atoms, m_i is the mass of atom i, and $\mathbf{a}_i$ is its acceleration. Numerical integration of Eq. 2.8 then yields a trajectory that describes the positions, velocities, and accelerations of the atoms. As a result, by providing an initial set of positions and velocities, the state of the system can in principle be completely determined at any time.

With an appropriate interatomic potential energy V, the force can be described as

$$\mathbf{F}_i = -\nabla_i V = m_i d^2\mathbf{r}_i/dt^2, \tag{2.9}$$

where $\mathbf{r}_i$ is the atomic coordinate of atom i. Thus, Newton's equation of motion can be related to the derivative of the potential energy to the change in position as as function of time. The probability distribution of the velocities $\mathbf{v}_i$ of atoms i at a given temperature T are often determined by the Maxwell-Boltzmann as,

$$f(\mathbf{v}_i) = \left(\frac{m_i}{2\pi k_B T}\right)^{\frac{3}{2}} exp\left[-\frac{m_i v_i^2}{2k_B T}\right], \tag{2.10}$$

where k_B is Boltzmann's constant. The temperature can be evaluated from the velocities using the following relation,

$$T = \frac{2}{3k_B}\left\langle \frac{1}{N}\sum_{i=1}^{N}\frac{|\mathbf{p_i}|^{\mathbf{2}}}{2m_i}\right\rangle, \tag{2.11}$$

where, $<$ ... $>$ denotes the time-averaged quantity, N is the number of atoms in the system, and p_i is the momentum of atom i.

2.2.1 The velocity Verlet algorithm

A variety of numerical algorithms have been used to integrate the equations of motion in MD. We use the velocity Verlet algorithm [33, 34] to integrate the equation of motion with a chosen small time step Δt. The advantages of this algorithm is that it is straightforward and the storage requirements are modest. The velocity Verlet algorithms for a new position, velocity, acceleration, are given by

$$\mathbf{r}(t+\Delta t) = \mathbf{r}(t) + \mathbf{v}(t)\Delta t + \frac{1}{2}\mathbf{a}(t)\Delta t^2 + O(\Delta t^4) \tag{2.12}$$

$$\mathbf{v}(t+\Delta t) = \mathbf{v}(t) + \frac{1}{2}\Delta t\mathbf{a}(t+\Delta t) + \mathbf{a}(t)] + O(\Delta t^2) \tag{2.13}$$

$$\mathbf{a}(t+\Delta t) = -\frac{1}{m}\boldsymbol{\nabla}V(\mathbf{r}(t+\Delta t)) \tag{2.14}$$

2.3 Thermalization

2.3.1 Berendsen temperature coupling

While the velocity-Verlet algorithm naturally leads to simulations at constant energy corresponding to the microcanonical (NVE) ensemble, in many cases it is of interest to carry out simulations at constant temperature. One method to do this is the use of a Berendsen thermostat [35]. In this case, the temperature of the system is maintained by coupling to an external heat bath at the desired temperature T_0. In particular, at each step Δt the velocities are rescaled such that the rate of change of temperature is proportional to the difference in temperature

$$\frac{dT}{dt} = \frac{1}{\tau}(T_0 - T) \tag{2.15}$$

where τ is a coupling parameter that determines how the bath and the system are coupled together. This leads to an exponential decay of the system towards the desired temperature i.e.

$$T = T_0 - Ce^{-\frac{t}{\tau}} \tag{2.16}$$

In discrete terms, Eq. 2.15 then becomes:

$$\Delta T = \frac{\Delta t}{\tau}(T_0 - T) \tag{2.17}$$

This implies that at each time-step the velocities $\{\mathbf{v}_i\}$ are all multiplied by a scaling factor λ where,

$$\lambda = \left[1 + \frac{\Delta t}{\tau}\left(\frac{T_0}{T} - 1\right)\right]^2 \tag{2.18}$$

2.3.2 Langevin Thermostat

The Langevin equation is a stochastic differential equation used to simulate the atoms which are assumed to be in a sea of much smaller frictional particles. In general the Langevin equation can be expressed as:

$$m\dot{\mathbf{v}} = \mathbf{F}_{ext} + \mathbf{F}_F + \mathbf{F}_R \tag{2.19}$$

where m is the mass of the particle, $\mathbf{v}$ its velocity, $\mathbf{F}_{ext} = \boldsymbol{\nabla} V(\mathbf{r})$ arises due to the inter-particle interactions (i.e. $V(\mathbf{r})$), $\mathbf{F}_F = -m\gamma\mathbf{v}$ is frictional force and γ as frictional coefficient, and $\mathbf{F_R}$ is the random force. The random force is assumed to have the following properties:

$$< \mathbf{F}_R(t) >= 0 \tag{2.20}$$

$$< \mathbf{F}_R(t)\mathbf{F}_R(t') >= 2A\delta(t - t') \tag{2.21}$$

where t is time, $<>$ denotes a time-average, and the fluctuation-dissipation theorem implies that $A = \frac{3}{2}m\gamma k_B T$. The acceleration on each atom i is then given by,

$$\mathbf{a}_i(t) = \frac{\mathbf{F}_i(\mathbf{r}(t))}{m} - \gamma \mathbf{v}_i(t) + \sqrt{\frac{3\gamma k_B T}{m}}\boldsymbol{\xi}_i \tag{2.22}$$

where the $\boldsymbol{\xi}_i$'s are independent Gaussian random variables satisfying $< \boldsymbol{\xi}_i >= 0$ and $< \boldsymbol{\xi}_i^2 >= 1$.

2.4 Potentials

Two popular types of potentials that were used in our simulations are the embedded atom method (EAM) potential and bond order potential (BOP).

2.4.1 Embedded Atom Method (EAM)

This method was developed by Murray Daw and Mike Baskes [36, 37] and is particularly good for metallic systems since in the original method it takes into account the local electron density but does include any angular dependence. In this type of interatomic potential, the potential energy function includes both a pair-interaction as well as a many-body interaction which takes into account each atom's interaction with the electron density due to all nearby atoms. The total energy of a system of N atoms is the sum over the atom energies as:

$$E_{tot} = \sum_{i}^{N} E_i. \tag{2.23}$$

where the energy E_i of atom i is given by,

$$E_i = \frac{1}{2}\sum_{j \neq i} \phi_{\mu\nu}(r_{ij}) + F_\mu(\rho_{i,tot}) \tag{2.24}$$

where $\rho_{i,tot} = \sum_{j \neq i} \rho_{\mu\nu}(r_{ij})$ is the total electron density at atom i due to nearby atoms, $\phi_{\mu\nu}(r)$ is a species and distance-dependent pair-interaction and $F_{\mu}(\rho_{i,tot})$ is the embedding energy which is a function of the total local electron density. Here μ and ν are the types of atoms i and j. For a binary alloy, the EAM potential requires seven functions:

a. three pair-wise interaction potentials $(\alpha - \alpha, \alpha - \beta, \beta - \beta)$

b. two embedding functions

c. two electron density function $\rho_{\mu\nu}$.

2.4.2 Bond Order Potential (BOP)

The analytical form of the BOP has been derived in the Refs. [38–42] from quantum mechanical theories which take into account of both π and σ bonding. In the tight-binding theory, the bond energy is the multiplication of bond-order Θ and bond-integral β [41]. In the BOP framework, The total energy of the system containing N atoms (i = 1, 2, 3, ..., N) can be expressed as

$$E = \frac{1}{2} \sum_{i=1}^{N} \sum_{j=i_1}^{i_N} \phi_{ij}(r_{ij}) - \sum_{i=1}^{N} \sum_{j=i_1}^{i_N} \beta_{\sigma,ij}(r_{ij}).\Theta_{\sigma,ij} - \sum_{i=1}^{N} \sum_{j=i_1}^{i_N} \beta_{\pi,ij}(r_{ij}).\Theta_{\pi,ij}, \qquad (2.25)$$

where $\phi_{ij}(r_{ij})$ is a short-range two-body potential representing the overlap repulsion between a pair of ion cores [40, 41], $\beta_{\sigma,ij}(r_{ij})$ and $\beta_{\pi,ij}(r_{ij})$ are, respectively, σ and π bond integrals, $\Theta_{\sigma,ij}$ and $\Theta_{\pi,ij}$ are σ and π bond-orders and are function of the local environment of atom i and j, and j = $i_1, i_2, ..., i_N$ represents neighbors of atom i. r_{ij} is the interatomic distance between atom i and j. We note that the expressions for $\Theta_{\sigma,ij}, \Theta_{\pi,ij}, \sigma_{\sigma,ij}$, and $\sigma_{\pi,ij}$ are quite complex and involve a variety of three-body terms as well as a large number (39) of parameters which are typically fit to experiments and DFT calculations. In the case of our CdTe simulations in Chapter 7 these parameters were fit [43] to a variety of experiments as well as density-functional theory calculations for CdTe clusters, bulk lattices, defects, and surfaces.

2.5 Temperature Accelerated Dynamics (TAD)

While molecular dynamics simulations are useful for the study of properties (such as vibrations and local ordering) which involve time-scales of μs or less, in many cases we are interested in infrequent events which involve transitions between different states separated by energy barriers which happen on much longer time-scales. Fig 2-2 shows an example of such an infrequent event (Fig 2-2. (a) corresponding to the monomer exchange of an atom from one site to another with forward (reverse) barrier 0.29 (0.55) eV) along with a schematic showing the corresponding energy barrier (Fig 2-2 (b)). One method which has been developed to deal with this issue is temperature-accelerated dynamics (TAD).

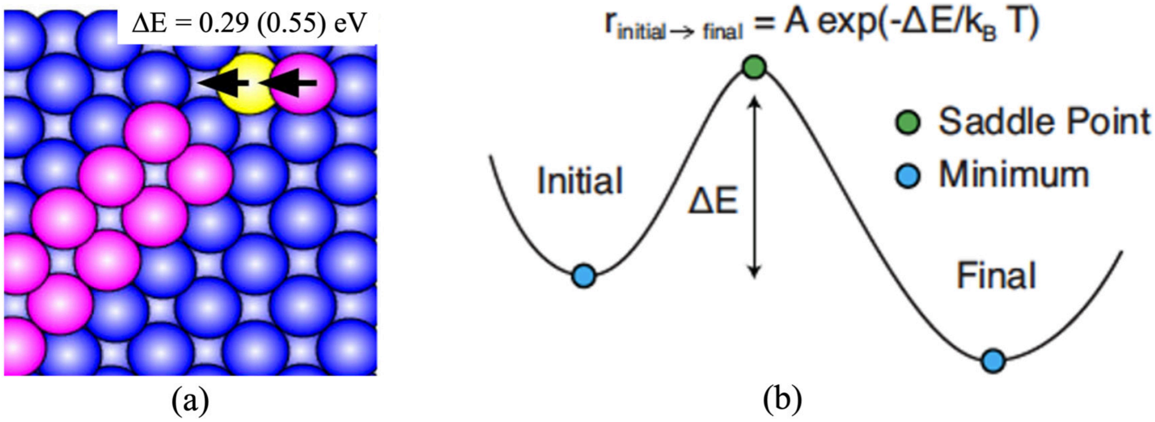

(a) (b)

Figure 2-2: (a) is an example of monomer exchange with forward (reverse) barrier 0.29 (0.55) eV and (b) is a pictorial representation of the Harmonic Transition State Theory [14].

In the TAD method a series of basin-constrained MD simulations at a high-temperature T_{high} is used to determine the state-to-state trajectory of the system at a desired low-temperature T_{low} [15, 44]. It is based on harmonic transition state theory (hTST) [15, 44–47] which states that the rate ν_i of an activated event i with energy barrier E_i can be expressed using the Arrhenius law,

$$\nu_i = \nu_{o,i}\ exp\left[\frac{-E_i}{k_B T}\right], \tag{2.26}$$

where $\nu_{o,i}$ is prefactor, k_B is Boltzmann's constant, and T is the temperature. During the high temperature MD, the system escapes from an initial state or energy basin to a final state in a time $t_{i,high}$. By determining the activation energy E_i of each event i using the nudged elastic band (NEB) method [47], the time t_{low} at which that event would have happened at low temperature T_{low} [15] can be determined using the relation,

$$t_{i,low} = t_{i,high}\ exp\left[E_i(\frac{1}{k_B T_{low}} - \frac{1}{k_B T_{high}})\right]. \tag{2.27}$$

The system is then returned to the original state and equilibrated to search for additional transitions. This process continues until one is confident, with confidence level $1-\delta$ (where typically $\delta \simeq 0.01 - 0.1$) that no transitions with extrapolated low temperature times $t_{i,low}$ which are shorter than the smallest value of $t_{i,low}$ found so far ($t_{low,short}$) will be found if additional high-temperature MD simulations are carried out. In particular, the high temperature MD run can be terminated once the high-temperature $t_{i,high}$ reaches the value,

$$t_{high,stop} = [\nu^*_{min}]^{-1}(\nu^*_{min} t_{low,short})^{\frac{T_{low}}{T_{high}}} \tag{2.28}$$

where $\nu^* = \frac{\nu_{min}}{ln(1/\delta)}$. At this point the transition corresponding to $t_{low,short}$ is accepted and the system is moved to the corresponding state in order to carry out another basin-constrained high-temperature simulation. The method is illustrated pictorially in Fig. (2-3).

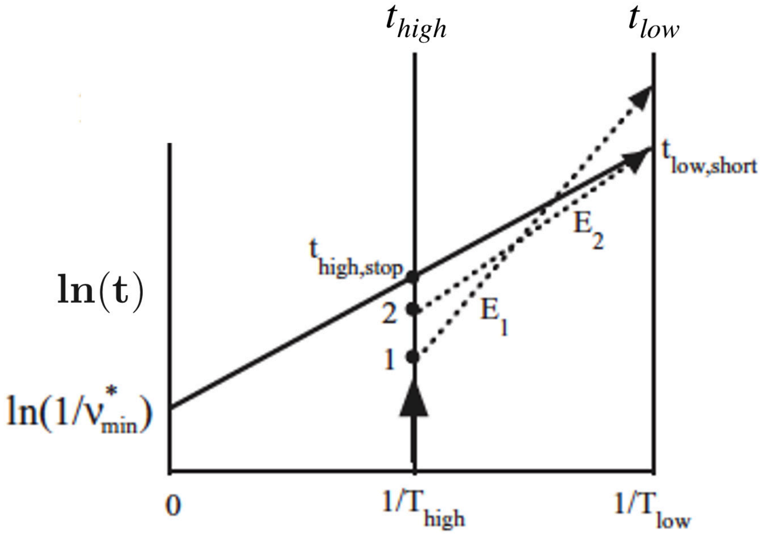

Figure 2-3: Pictorial representation of the TAD method [15].

Chapter 3

Correlating the stability and mechanical properties of 3d transition metal carbides with valence electron concentration and crystal structure

3.1 Introduction

Many transition metal carbides (TMCs), nitrides, and carbonitrides are known to display a wide range of remarkable physical and chemical properties [48–61]. These include but are not limited to exceptional hardness and wear resistance, robust stability at high operating temperatures, and high thermal conductivity [54]. Moreover, TMCs have been the subject of intense research interest in the fields of catalysis and surface science [62]. Detailed reviews of previous work on well-studied TMCs and their alloys can be found in Refs. [48–69]. Owing to their versatile properties, several TMCs have been considered for industrial applications involving hard coatings [70, 71], refractory materials, conducting barriers, energy storage devices [72, 73], catalytic agents [74], and potentially even high-temperature superconductors [75]. Depending on the application in focus, many previous studies have aimed to study the electronic structure and its influence on the bonding characteristics of the TMCs [49, 63, 76]. Because the underlying electronic structure may be tuned using both structure and composition, it is possible to fine-tune the materials by design. However, this requires a detailed understanding of the correlation between atomic-level electronic interactions and macroscopic properties. We, therefore, aim to build upon previous work [77, 78]. to illustrate a clear framework describing the factors influencing the stability and mechanical performance of TMCs.

Numerous studies have been conducted on TMCs using both experimental [79–82] and theoretical techniques, primarily focusing on the rocksalt structure which is most commonly adopted by these compounds [17, 83–91, 91–97]. With respect to their mechanical properties, Balasubramanian *et al.* [77] identified the valence electron concentration as a dominant factor controlling hardness and ductility across many rocksalt TMCs based on orbital filling. Using similar arguments, Häglund *et al.* [58] found that the cohesive energy in 3d TMCs is correlated with the filling of bonding and antibonding orbitals, with TiC showing the most exothermic cohesive energy of all compounds considered. Moving toward TMCs with higher group numbers, Singh *et al.* [86] reported that instability arises as metal-carbon bonds become weakened upon the increased filling of the antibonding orbitals, e.g., in CrC. This effect becomes more pronounced when dealing with the intermediate and late TMCs (FeC, CoC, and NiC), where previously reported mechanical properties imply relatively weak bonding [89].

While there has been extensive work done involving TMCs, a detailed and systematic investigation of 3d TMCs has not yet been reported across three unique cubic structures: rocksalt (RS), zincblende (ZB), and cesium chloride (CsCl). Here, we address this shortcoming by presenting the results of first-principles calculations based on density functional theory. We specifically choose to focus on the electronic structures, formation energies, and phonon dispersion curves calculated for all ten 3d TMCs. We restrict our main analysis to cubic structures as those are suspected to balance good hardness and ductility, whereas materials with a hexagonal (wurtzite) structure tend to be brittle owing to a lack of slip planes [98, 99]. Our calculated results comprise a theoretical guide that may be used to understand how valence electron concentration and bonding configuration each play a role in the stability of these compounds. In addition, we have also studied the mechanical properties of compounds that are predicted to be stable using calculated elastic tensors. Derived properties are then considered to reveal insight into the performance of the TMCs for hard coating applications.

3.2 Computational methods

All density functional theory (DFT) calculations were carried out using the Vienna Ab initio Simulation Package (VASP) [28–32]. The projector augmented wave (PAW) [100] method was utilized with exchange-correlation interactions treated by the generalized gradient approximation (GGA) in the Perdew-Burke-Ernzerhof (PBE) formalism [25–27]. For the early 3d transition metals Sc, Ti, and V, semi-core s and p electrons were included as valence states, whereas only semi-core p electrons were included for Cr and Mn. Only outer-core electrons were explicitly considered in the late transition metals Fe, Co, Ni, Cu, and Zn. A plane-wave basis set was constructed using a kinetic energy cutoff of 520 eV. Γ-centered grids of 4,000 k-points per reciprocal atom (KPPRA) were employed for all calculations in the Brillouin zone [101, 102]. Electron minimizations, for which Gaussian smearing of width 0.05 eV was used, were performed with a convergence criterion of 10^{-6} eV/atom as in previous work [7, 11].

Spin-polarization was taken into account for all compounds. Four possible magnetic configurations were tested with respect to the transition metal ions: (i) non-magnetic ordering with each moment set to zero, (ii) ferromagnetic ordering with all moments aligned parallel, (iii) antiferromagnetic ordering with moments alternating along the [001] direction, and (iv) antiferromagnetic ordering with moments alternating along the [111] direction. For all compounds studied in this work, a non-magnetic or ferromagnetic configuration was identified to be the lowest-energy state – these ground states were used throughout the remainder of the calculations. Ionic relaxations were performed using a conjugate-gradient algorithm with a force constant criterion of 0.01 eV/$\AA$ as described in earlier works [103]. To precisely determine equilibrium lattice constants and bulk moduli, energies were computed for each compound at six volumes about the approximate energetic minima; these values were then fit to a Birch-Murnaghan equation of state [104, 105].

To study the stability of each compound, we consider two key aspects: dynamics and energetics. Understanding the dynamical behavior of the structure is necessary to determine whether it is stable against perturbations; these include changes to the unit cell dimensions (strain), as well as collective atomic displacements (vibrational modes). To gain insight into the former, we calculated the independent elastic constants corresponding to the cubic crystal system (C_{11}, C_{12}, and C_{44}) by computing the energy of the unit cell under varied sets of strain and fitting the resulting values to a quadratic stress-strain relationship, as is described in detail throughout previous work [6, 10]. From the elastic constants, stability against cell strain was determined using the Born criteria [106, 107]:

$$C_{11} - C_{12} > 0, C_{11} + 2C_{12} > 0, \text{and } C_{44} > 0, \tag{3.1}$$

As for the effects of vibrational modes, we computed phonon dispersion curves along high-symmetry paths in the Brillouin zone. This was done by calculating the Hessian matrices for 5×5×5 supercells using density functional perturbation theory (DFPT) [32] as implemented in VASP, with post-processing conducted via the PHONOPY [108] software. Compounds are deemed dynamically stable if all phonon frequencies are real, which implies that all atoms occupy positions corresponding to local energy minima. Should this condition hold, the next question is whether they are stable with respect to decomposition into competing phases, i.e., does the compound represent the energetic ground state. Here, we calculate the formation energy per atom of each binary carbide with respect to its constituent elemental ground states using the following equation:

$$\Delta E_F = \frac{E_{MC} - E_M - E_C}{2} \tag{3.2}$$

Accordingly, compounds with $\Delta E_E < 0$ are energetically preferable to the competing elemental phases, whereas compounds with $\Delta E_E > 0$ are energetically unstable. However, we note that such compounds may still be metastable assuming kinetic barriers are significant. The ground state structures of metal and carbon were used from Ref. [109].

To study the mechanical properties of the TMCs, we used the calculated elastic constants to obtain the bulk modulus (B), Cauchy pressure (P_c), shear modulus under the Voigt (G_ν) and Reuss approximations (G_R) as well as Hill's arithmetic mean (G), Pugh's ratio (κ), Poisson's ratio (ν), and Young's modulus (Y) using the following equations:

$$B = \frac{(C_{11} + 2C_{12})}{3} \tag{3.3}$$

$$P_c = C_{12} - C_{44} \tag{3.4}$$

$$G_\nu = \frac{[(C_{11} - C_{12}) + 3C_{44}]}{5} \tag{3.5}$$

$$G_R = \frac{[5(C_{11} - C_{12})C_{44}]}{[4C_{44} + 3(C_{11} - C_{12})]} \tag{3.6}$$

$$G = \frac{(G_\nu + G_R)}{2} \tag{3.7}$$

$$\kappa = \frac{G}{B} \tag{3.8}$$

$$\nu = \frac{(3 - 2\kappa))}{[2(3 + \kappa)]} \tag{3.9}$$

$$Y = \frac{9G}{(3 + \kappa)} \tag{3.10}$$

The Vickers hardness (H_ν) was calculated using the following relation by Tian *et.al.* [110]:

$$H_\nu = 0.92\kappa^{1.137}G^{0.708} \tag{3.11}$$

To relate the macroscopic properties of TMCs to their underlying electronic structure, we calculated the density of states for each compound using the tetrahedron method with Blochl corrections [111]. Densities were further separated into elemental and orbital components to highlight the effects of the ligand field present in each structure. The ionic characters of individual bonds were revealed using metal-to-carbon charge transfer calculated within Bader's division scheme [112–114], which partitions real space to quantitatively attribute charge to each atom. On the other hand, covalent interactions were studied using Crystal Orbital Hamiltonian Populations (COHP) calculations performed with the LOBSTER package [115–119], which separates electronic occupancies into bonding and antibonding states.

3.3 Results and Discussion

3.3.1 Structure and stability

The calculated volumes (per formula unit) of the 3d transitional metal carbides (TMCs) in the ZB, RS, and CsCl structures are listed in Table 3.1, showing excellent agreement with previously reported [120, 121] data where available. Analyzing trends in volume with respect to structure, we observe an inverse correlation between the volume and the coordination number of the underlying atomic arrangement. Namely, $V_{ZB} > V_{RS} > V_{CsCl}$ owing to their respective coordination numbers of four, six, and eight. As for the effect of chemistry, there exists a nearly parabolic relationship between the volume and group number in all structures. This trend is directly related to the size of the metal element, which decreases from the early to intermediate TMs, then increases from intermediate to late TMs. As displayed in Fig. 3-1, subtle deviations from the parabolic relationship can be attributed to variations in the degree of bonding covalency versus ionicity [16]. Those elements with a large number of unpaired d electrons (e.g., Mn and Fe) tend to exhibit bond lengths representative of their covalent radii [16], whereas those with fewer unpaired electrons more clearly adopt highly ionic bonds.

Table 3.1: Calculated volumes (V), normalized per formula unit (f.u.), for all 3d transition metal carbides (TMCs) in the zincblende, rocksalt, and cesium chloride structures. Previously computed data, where available, are given for comparison. The mechanical and dynamical stability of each compound are also presented. "MS/MU" corresponds to the mechanically stable/unstable according to the Born criteria and "DS/DU" correspond to the dynamically stable/unstable as indicated by fully real-valued phonon mode frequencies.

Compound	Zincblende		Rocksalt		Cesium chloride	
	V ($\AA^3$/f.u.)	Stability	V ($\AA^3$/f.u.)	Stability	V ($\AA^3$/f.u.)	Stability
ScC	32.78	MU, DU	25.71 25.72[T,[121]]	MS, DS	23.81	MS, DU
TiC	26.50	MS, DS	20.40 20.37[T, [121]]	MS, DS	19.97	MU, DU
VC	23.04	MS, DS	18.08 18.03[T, [121]]	MS, DS	17.51	MU, DU
CrC	21.14	MS, DS	19.91 19.96[T, [120]]	MS, DS	16.12	MS, DU
MnC	20.06	MS, DS	16.31	MS, DU	15.33	MS, DU
FeC	19.27	MS, DS	15.95	MS, DU	15.00	MU, DU
CoC	19.50	MS, DS	16.14	MS, DU	15.48	MU, DU
NiC	20.60	MS, DU	16.82 16.95[T, [121]]	MS, DU	16.35	MU, DU
CuC	22.72	MU, DU	18.95	MS, DU	18.44	MU, DU
ZnC	25.72	MS, DS	21.31	MS, DS	21.06	MU, DU

^{T}: Computed value

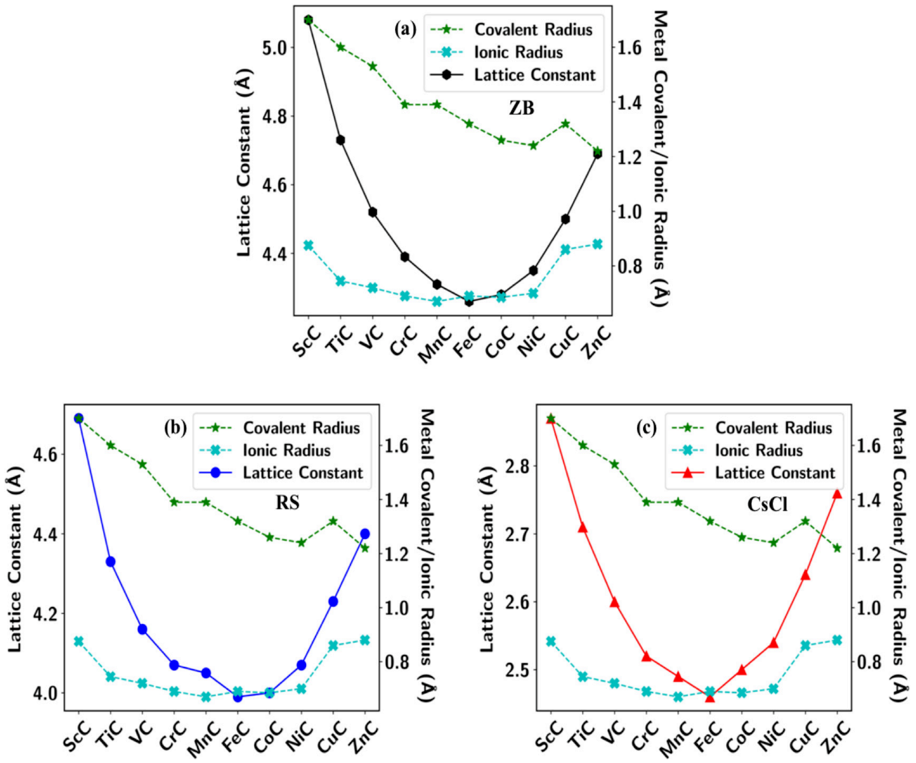

Figure 3-1: Comparison between dependence of calculated lattice constants of the 3d TMCs on valence electron concentration with corresponding ionic and metal covalent radius [16] for zincblende (ZB) (a), rocksalt (RS) (b), and cesium chloride (CsCl) (c) structures.

Calculated lattice parameters and elastic constants are listed Table 3.2 and 3.3 respectively, and are in good agreement with available experimental [122, 123] and calculated value [124]. The calculated elastic constants are used to determine whether each compound is mechanically stable, i.e., if they satisfy the Born criteria [106, 107] and are therefore able to withstand strain without undergoing a phase transformation. We find twenty total compounds to be mechanically stable; these include eight ZB, ten RS, and two CsCl structures. Interestingly, there appears to be a clear difference in the origin of mechanical instability in the ZB and CsCl configurations – the former exhibits a lower value of C_{11} than C_{12}, whereas the latter exhibits a negative value of C_{44}. This suggests that the ZB structures are prone to instabilities arising from normal (uniaxial) strain, whereas CsCl structures are more likely to transform via shear strain. This agrees with expectations based on the connectivity of each structure - the ZB arrangement favors strong directional and shear-resistant bonding but is less robust against uniaxial compression owing to its low atomic density. In contrast, the CsCl structure is amenable to isotropic bonding, which is much more susceptible to shearing instabilities, while its high density is more resistant to normal strain. An intermediate situation is found in RS, which is commonly adopted by compounds formed via strong covalent (directional) and ionic (isotropic) bonding, including titanium carbides and nitrides which are known to be exceptionally resistant to deformation. As a result of these hybrid bonding characteristics, all ten 3d TMCs are mechanically stable in the RS structure.

Table 3.2: Calculated lattice parameters (a_{calc}) for all 3d transition metal carbides (TMCs) in the zincblende structure (ZB), rocksalt structure (RS), and cesium chloride structure (CsCl). Experimental data, where available, are listed in parenthesis for comparison. The mechanical and dynamical stability of each compound are also presented. "MS/MU" corresponds to the mechanically stable/unstable and "DS/DU" correspond to the dynamically stable/unstable.

Compound	Zincblende		Rocksalt		Cesium chloride	
	a_{calc} ($\AA$)	Stability	a_{calc} ($\AA$)	Stability	a_{calc} ($\AA$)	Stability
ScC	5.08	MU, DU	4.69	MS, DS	2.87	MS, DU
TiC	26.50 4.74[T, [124]]	MS, DS	4.33 4.33[E, [125]]	MS, DS	2.71 2.72[T, [124]]	MU, DU
VC	4.52	MS, DS	4.16 4.18[E, [122]]	MS, DS	2.60	MU, DU
CrC	4.39	MS, DS	4.07 4.03[E, [123]]	MS, DS	2.52	MS, DU
MnC	4.31	MS, DS	4.05	MS, DU	2.49	MS, DU
FeC	4.26	MS, DS	3.99	MS, DU	2.46	MU, DU
CoC	4.28	MS, DS	4.00	MS, DU	2.50	MU, DU
NiC	4.35	MS, DU	4.07	MS, DU	2.54	MU, DU
CuC	4.50	MU, DU	4.23	MS, DU	2.64	MU, DU
ZnC	4.69	MS, DS	4.40	MS, DS	2.76	MU, DU

^{T}: Computed value, ^{E}: Experimental value

Table 3.3: Calculated elastic constants (C_{11}, C_{12}, C_{44}), and mechanical stability of 3d transitional metal carbides (TMCs) in zincblende (ZB), rocksalt (RS), and cesium chloride (CsCl) structures. The mechanical and the dynamical stability of each compound are also presented; “MS/MU” indicates mechanically stable/unstable and “DS/DU” correspond to the dynamically stable/unstable.

Compound	C_{11} (GPa)			C_{12} (GPa)			C_{44} (GPa)			Stability		
	ZB	RS	CsCl	ZB	RS	CsCl	ZB	RS	CsCl	ZB	RS	CsCl
ScC	85.6	298.1	103.2	107.0	82.9	175.6	23.9	61.6	-132.7	MU, DU	MS, DS	MU, DU
TiC	193.8	517.2	11.0	151.1	120.4	325.2	59.5	173.8	-342.0	MS, DS	MS, DS	MU, DU
VC	289.3	625.3	438.2	164.9	145.5	213.0	60.3	165.7	-65.3	MS, DS	MS, DS	MU, DU
CrC	301.3	621.4	665.9	194.7	179.7	161.4	25.4	138.5	109.5	MS, DS	MS, DS	MS, DU
MnC	306.3	578.7	756.3	210.8	210.8	143.6	42.3	21.6	46.3	MS, DS	MS, DU	MS, DU
FeC	342.9	589.4	769.9	208.7	205.8	132.3	65.3	77.6	-28.2	MS, DS	MS, DU	MU, DU
CoC	307.9	530.6	558.6	204.0	195.5	170.1	62.1	49.2	-19.2	MS, DS	MS, DU	MU, DU
NiC	201.1	319.5	362.4	200.0	223.5	162.6	24.1	67.8	-38.1	MS, DU	MS, DU	MU, DU
CuC	147.3	240.1	222.6	150.8	153.3	160.2	19.0	20.5	-38.0	MU, DU	MS, DU	MU, DU
ZnC	117.4	225.7	128.4	107.4	101.9	143.7	25.2	41.7	-40	MS, DS	MS, DS	MU, DU

Table 3.4: Calculated formation energy per atom (ΔE_F) in eV of the transition-metal carbides in zincblende (ZB), rocksalt (RS), cesium chloride (CsCl), and wurtzite structure.

Compound	ZB	RS	CsCl	Wurtzite
ScC	0.44	-0.17	0.37	0.09
TiC	-0.17	-0.83	0.35	-0.57
VC	0.13	-0.42	0.42	-0.34
CrC	0.51	0.16	0.68	0.05
MnC	0.44	0.33	0.70	0.19
FeC	0.43	0.56	0.92	0.45
CoC	0.57	0.80	1.24	0.67
NiC	0.93	1.10	1.44	0.94
CuC	1.70	1.71	1.90	2.14
ZnC	1.67	1.64	1.92	1.59

Table 3.5: Calculated Integrated Projected Crystal Orbital Hamiltonian Populations (ipCOHP) in eV of the transition-metal carbides in zincblende (ZB) and rocksalt (RS). M and C correspond to metal and carbon respectively.

Compound	ZB			RS		
	M-M	M-C	C-C	M-M	M-C	C-C
ScC	0.019	1.398	0.037	-0.007	1.223	0.048
TiC	0.103	2.235	0.079	0.008	1.546	0.034
VC	0.054	2.108	0.151	0.038	1.292	0.078
CrC	0.161	2.071	0.145	0.114	1.211	0.071
MnC	0.154	2.131	0.163	0.095	1.189	0.090
FeC	0.134	2.042	0.159	0.0761	1.217	0.106
CoC	0.109	1.987	0.124	0.057	1.073	0.131
NiC	0.081	2.023	0.154	0.044	1.091	0.140
CuC	0.056	1.679	0.199	0.031	1.142	0.142
ZnC	0.023	1.398	0.220	-0.016	0.889	0.083

Table 3.6: Comparison of electronegativity (χ [12] of the transition metals and calculated Bader charge transfer (q_{tran}) from the metal to the carbon atom in zincblende (ZB), rocksalt (RS), and cesium chloride (CsCl) structure.

Compound	q_{tran}-ZB	q_{tran}-RS	q_{tran}-CsCl	Electronegativity (χ)
ScC	1.59	1.64	1.56	1.20
TiC	1.69	1.66	1.43	1.32
VC	1.49	1.52	1.26	1.45
CrC	1.25	1.29	1.09	1.56
MnC	1.08	1.11	0.90	1.60
FeC	0.79	0.88	0.70	1.64
CoC	0.66	0.78	0.65	1.70
NiC	0.63	0.75	0.61	1.75
CuC	0.64	0.73	0.63	1.75
ZnC	0.83	0.90	0.86	1.66

Table 3.7: Calculated Cauchy's pressure (P_c), Poisson's ratio (ν), and Pugh's ratio (κ) of each stable 3d transition metal carbides (TMCs) in the zincblende structure (ZB) and rocksalt structure (RS). Instability is denoted by "U". Since all TMCs are unstable in the cesium chloride structure (CsCl), the corresponding values are not presented here.

Compound	P_c		ν		κ	
	ZB	RS	ZB	RS	ZB	RS
ScC	U	21.4	U	0.29	U	0.50
TiC	91.6	-53.5	0.39	0.21	0.24	0.73
VC	104.7	-20.1	0.37	0.24	0.30	0.63
CrC	167.3	41.2	0.43	0.28	0.15	0.51
MnC	168.5	U	0.41	U	0.18	U
FeC	143.4	U	0.38	U	0.26	U
CoC	141.9	U	0.39	U	0.24	U
ZnC	82.1	60.2	0.44	0.35	0.12	0.34

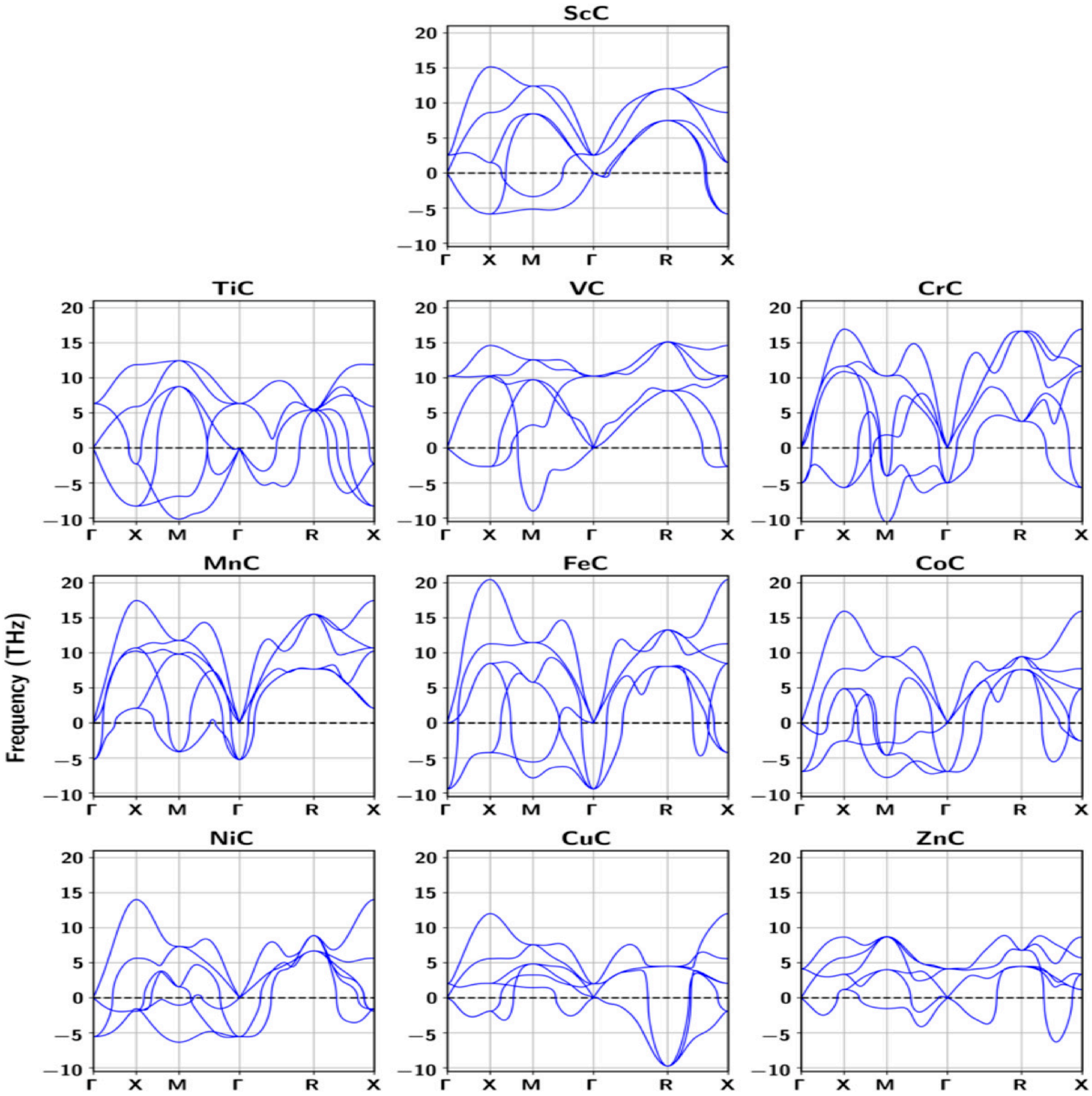

Figure 3-2: Phonon dispersion curves of 3d TMCs in cesium chloride (CsCl) structure calculated within the quasi-harmonic approximation.

To further investigate stability, we calculated the phonon dispersion curves of all 3d TMCs. As summarized in Table 3.1, we identify seven compounds as dynamically stable in the ZB structure, five in the RS structure, and zero in the CsCl structure. The presence of imaginary frequencies, as shown in Fig. 3-2, shows the dynamical instability of all the carbides in CsCl structure. The persistent instability of TMCs in the densely packed CsCl structure arises from its 8-fold coordination, which is deleterious to covalently bound systems such as the carbides studied here. The CsCl structure, with an 8-fold coordination, is commonly adopted by ionic systems as it maximizes (minimizes) the electrostatic attraction (distance) between cations and anions with a radius mismatch ratio near 0.64, according to Pauling's rules. In addition, an 8-fold coordination with square antiprismatic geometry would require sp^3d^4 hybridization, which is rare owing to its high energy cost [126, 127]. Indeed, previous works have demonstrated that TMCs may adopt the CsCl structure only at exceptionally high pressures, coupled with a transition to metallic bonding [128, 129]. As we aim to focus only on materials which may be useful under ambient conditions, we exclude the CsCl structure from consideration for the remainder of this work. With respect to the RS and ZB structures, our calculations confirm the stability of the previously reported TMCs based on the early transition metals (e.g., ScC, TiC, VC, and CrC) [124]. Purely predictive findings are proposed for the intermediate and late TMCs.

To uncover the origin of instability throughout intermediate TMCs in the RS and ZB structures, we identify any regions of the Brillouin zone in which phonon modes exhibit imaginary frequencies. Intermediate TMCs in the RS structure are found to exhibit instabilities surrounding the L point, with $\vec{k} = \frac{2\pi}{a}(0.5, 0.5, 0.5)$. As illustrated for MnC in Figure 3-3, the associated phonon mode yields an off-center displacement of the central transition metal atom toward an edge of the octahedral complex, therefore shortening the 2nd nearest-neighbor metal-metal bond. Specifically, the energy of the system is minimized when the separation between adjacent metal atoms is equal to 2.605 $\mathring{A}$, reflecting the formation of Mn^{4+} dimers [130]. From an orbital occupation perspective, this effect can be related to the nominal d^1 configuration which Mn adopts owing to the tetravalent state of the carbides. Each metal ion contributes one electron to the metal-metal bond, therefore forming an energetically preferred singlet state. Based on our calculated maps of the electron localization function (i.e., ELF maps displayed in Figure 3-4), the metal-metal interactions are mostly metallic in nature as electrons are delocalized between adjacent metal atoms with low ELF values (< 0.5) [131]. The effects of metallic dimerization are further illustrated by the projected electronic density of states displayed in Figure 3-6. While the early TMCs exhibit complete occupation of the hybridized p-e$_g$ orbitals and little to no occupation of the higher-energy p-t$_{2g}$ orbitals, the latter frontiers display increasing occupation as the electron count is raised throughout the intermediate TMCs, including MnC and NiC. Since the apices of the t$_{2g}$ orbitals lie directly between metal-carbon bonds within the octahedral coordination, they show some degree of overlap between the 2nd-nearest neighbor metal atoms. As a result, the initially non-bonding electrons occupying the t$_{2g}$ orbitals begin to interact with one another, encouraging the formation of metal dimers. Moreover, the distortions associated with dimerization face only weak resistance from the exceedingly weak metal-carbon bonds found in the intermediate TMCs, as will be discussed in Section 3.3.2. These combined effects of increased metal-metal interactions and decreased metal-carbon strengths yield the dynamic instabilities found in the RS configurations of MnC, FeC, CoC, NiC, and CuC.

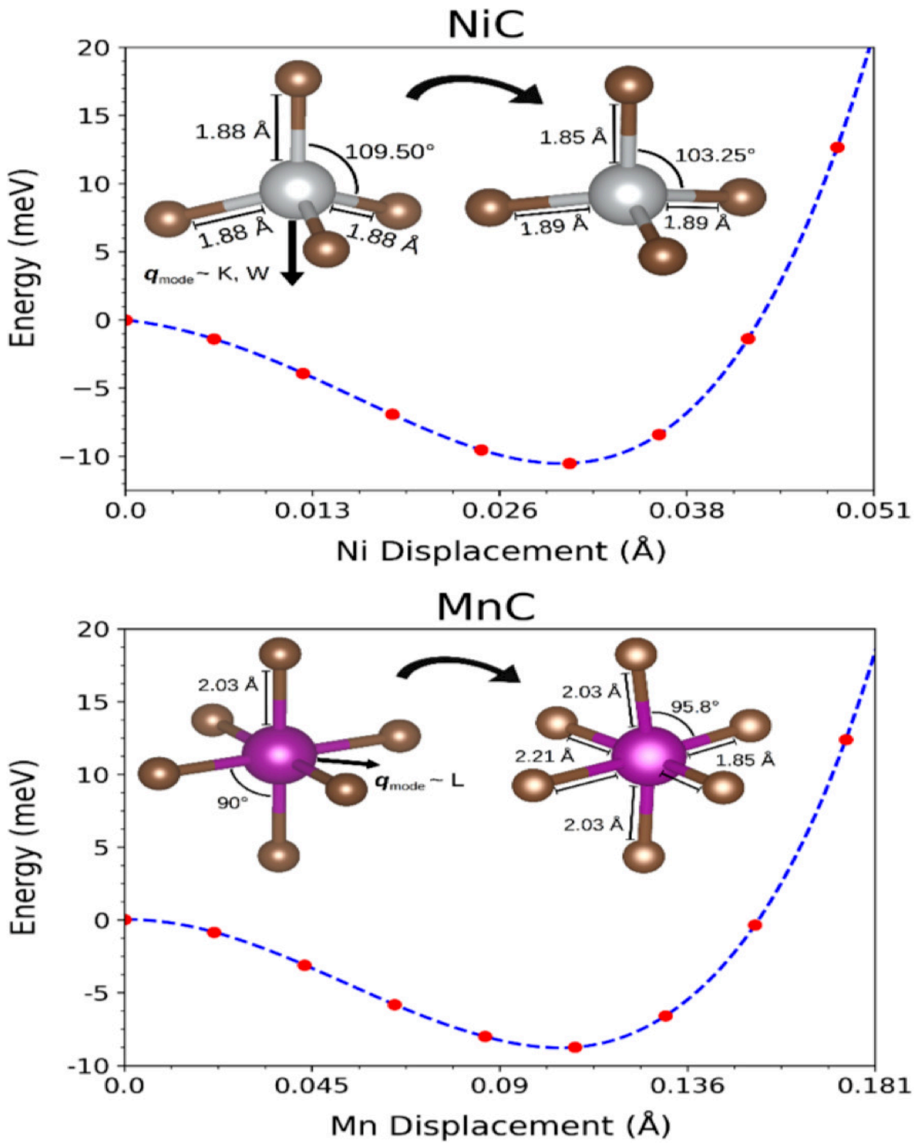

Figure 3-3: Illustration of the energy landscapes, modulated along instabilities at high-symmetry points according to phonon dispersion calculations, for NiC (top) and MnC (bottom) in the zincblende and rocksalt structures respectively. Insets show local bonding configurations (tetrahedra and octahedra) before and after application of distortions. For the latter, bond lengths and angles corresponding to a minimum in energy are listed.

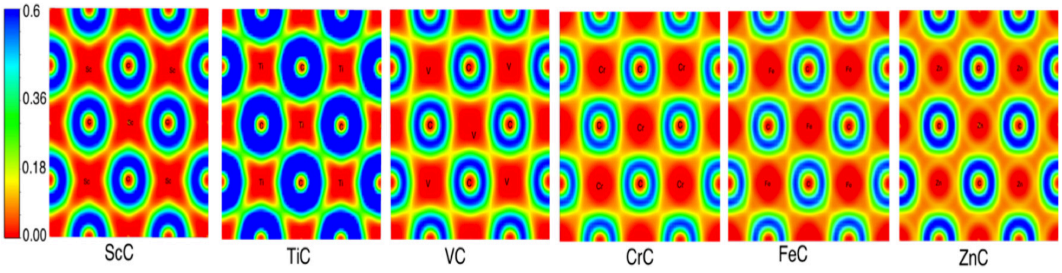

Figure 3-4: Electron localization function of stable/metastable 3d transition metal carbides in rocksalt (RS) structure.

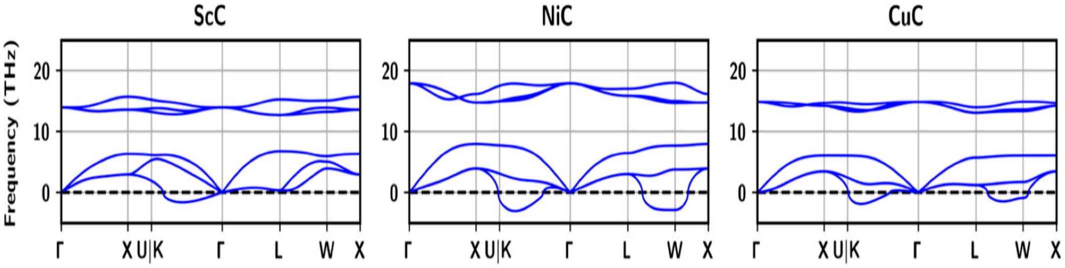

Figure 3-5: Phonon dispersion curves of the 3d TMCs in zincblende (ZB) structures which were found to be dynamically unstable in the harmonic approximation.

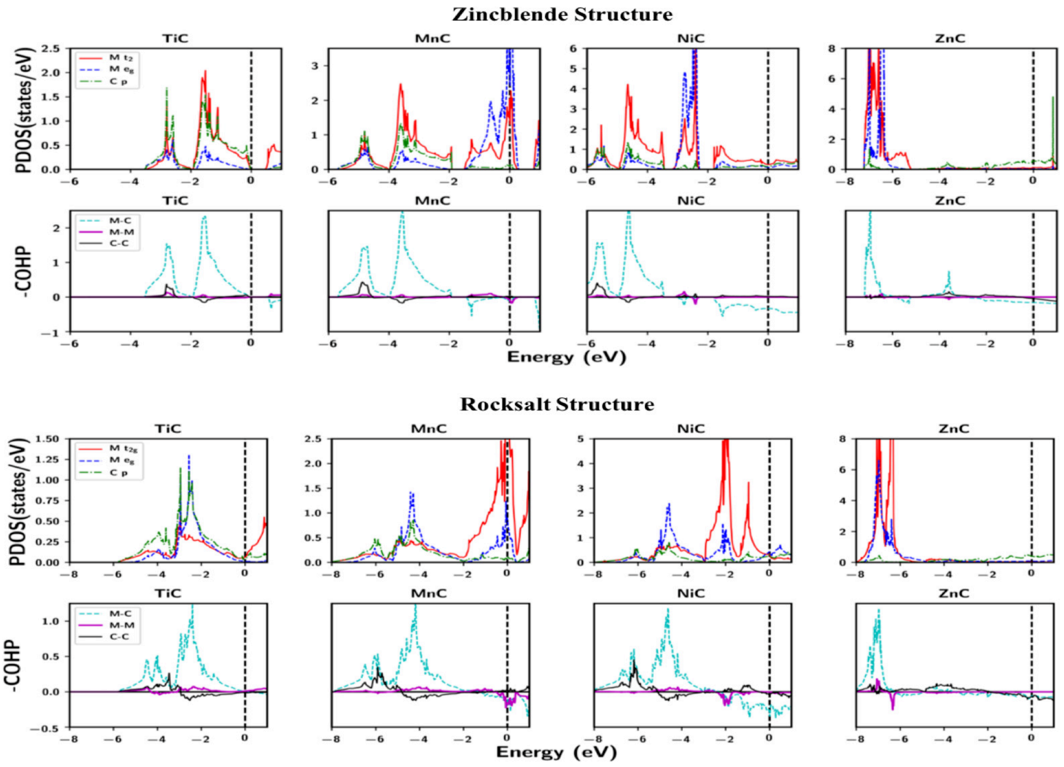

Figure 3-6: Projected density of states (PDOS) and Crystal Orbital Hamiltonian Populations (COHP) of four unique TMCs spanning the 3d row. Compounds considered in the zincblende and rocksalt structures are presented in the top and bottom panels respectively. For the PDOS, 3d densities are separated into t_{2g} and e_g components to illustrate the effects of crystal field splitting. In the COHP curves, covalent interactions among metal-carbon (M-C), metal-metal (M-M), and carbon-carbon (C-C) bonding pairs are shown. Positive and negative values of COHP represent bonding and antibonding respectively. For all plots, the Fermi energy is set to 0 eV.

For compounds adopting the ZB structure, the origin of instability can be divided into two major categories: those occurring in ScC, an early TMC, and those occurring in the intermediate-to-late TMCs of Ni and Cu. The former case of ScC is characterized solely by elastic instabilities, as demonstrated by the aforementioned low value of C_{11} and equivalently the soft acoustic phonons surrounding the Γ zone-center shown in Figure 3-5. In addition to the effects of connectivity and density discussed earlier in this Section, the instability of ScC can also be attributed to its unsaturated metal-carbon bonds, given that Sc may only contribute three valence electrons per atom. In contrast to the CsCl and RS structures, wherein respective metallic and ionic interactions may play a significant role, the ZB configuration relies heavily on covalent bonding. These bonds are insufficiently supported by the partially occupied orbitals in ScC, and therefore its structure is unstable with respect to cell distortions. In contrast, there is an excess of valence electrons available to participate in covalent bonding for both NiC and CuC, with nominal configurations of d^6 and d^7 respectively. Further distinguishing from ScC, these intermediate TMCs are prone to dynamic instabilities associated with imaginary phonon frequencies surrounding the K and W points of the Brillouin zone, with coordinates of $\vec{k} = \frac{2\pi}{a}(0.75, 0.75, 0.5)$ and $\vec{k} = \frac{2\pi}{a}(0.5, 1.0, 0.0)$ respectively. By following the corresponding atomic displacements, we identify an off-center displacement of the central metal atom parallel and away from the direction of one of the coordinated carbon atoms, essentially flattening the tetrahedral complex. This effect, illustrated for NiC in Figure 3-3, leads to a decrease in energy of 10 meV when the nickel atom is displaced by about 0.03 $\AA$. The distortions found in NiC and CuC are suggestive of a Jahn-Teller instability [132–134]. In the tetrahedral ligand field of the ZB structure, the 3d orbitals are split into two low-energy e orbitals and three high-energy t_2 orbitals. When t_2 orbitals become sufficiently occupied, as in the d^6 configuration of NiC, there are three degenerate electron configurations possible. By Jahn-Teller distorting (i.e., by displacing the central atom and lowering the symmetry of the tetrahedeal ligand field), a lower-energy configuration is adopted. This is further supported by the projected electron density of states, shown for NiC in Figure 3-6, which display partially occupied, nonbonding t_2 orbitals near the Fermi level. These states are initially degenerate and high-energy in the ideal tetrahedral coordination. However, as the orbitals are only partially filled by the d^6 configuration of NiC, the total energy of the system can be decreased via the aforementioned displacement of the central metal atom, which serves to enhance hybridization between the t_2 and p orbitals of the three nearest carbon atoms. Accordingly, both NiC and CuC are unstable in the ZB structure, whereas earlier TMCs may retain their ideal tetrahedral geometries owing to their decreased electron count serving to mitigate the incentive for Jahn-Teller [134, 135] distortions.

Lastly, we study the thermodynamic stability of the TMCs in each structure by calculating the formation energy with respect to the constituent elements in their ground states, with results displayed in Figure 3-7. Agreeing with their previously discussed dynamic instability in the earlier paragraph, all compounds adopting the CsCl structure are highly unstable with respect to decomposition, as signified by large, positive formation energies. In contrast, compounds in the RS and ZB structures generally exhibit much lower formation energies than those in the CsCl structure. Between these two configurations, RS is preferred for earlier TMCs owing to the substantial ionic character of their bonds, whereas ZB becomes energetically favorable for intermediate to late TMCs for which covalent interactions play a greater role. We emphasize that the vast majority of TMCs, regardless of structure, are thermodynamically unstable – agreeing with previous reports in the literature suggesting the difficulty to synthesize a variety of crystalline, stoichiometric carbides containing elements beyond Ti and Cr [17, 90]. Indeed, the calculated stability and experimental synthesizability of TMCs are both restricted to the early transition metals. ScC, TiC, and VC are thermodynamically stable and experimentally synthesizable [79, 136, 137]. Although CrC is thermodynamically unstable, its formation energy is relatively low, and it can be accessed using low-temperature synthesis techniques [138].

Trends in formation energy across the period can be directly correlated with the effects d orbital filling, which influence the occupation of bonding and anti-bonding states. To more clearly illustrate this effect, we analyze the COHP curves displayed in Figure 3-6 wherein positive values (above the y-axis) and negative values (below the y-axis) represent bonding and anti-bonding interactions respectively. First, ScC is shown to contain only partially filled bonding states resulting from the inability of Sc (s^2d^1) to contribute four electrons to its metal-carbon bonds. Despite this shortcoming, its high ionicity yields negative formation energies in the RS and ZB structures. Next, the increase in electron count allows all metal-carbon bonds to saturate as reflected by completely filled bonding states in the COHP curves. For this reason, TiC displays the lowest negative formation energy out of all TMCs studied here. From TiC on to the intermediate and late TMCs, the increasing electron count causes the antibonding states to become partially filled. These unfavorable interactions, mediated by electron repulsion, cause the formation energies to continuously increase moving from left to right across the period.

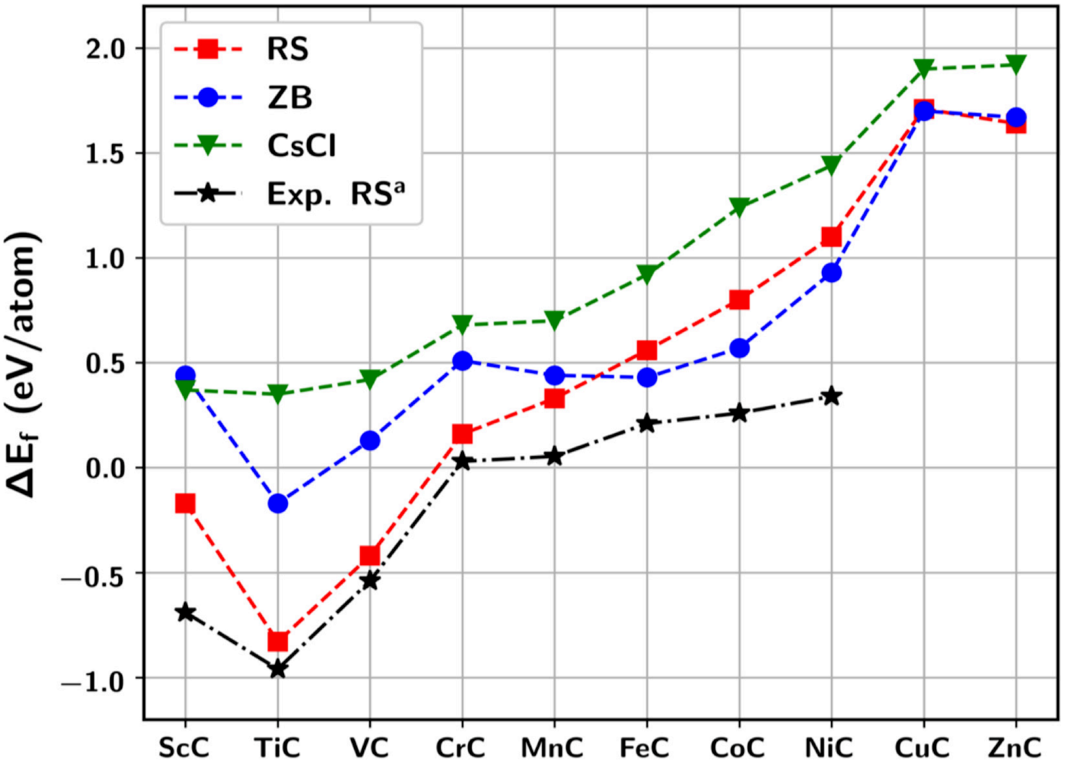

Figure 3-7: : Calculated formation energies of all 3d transition metal carbides in the rocksalt structure (RS), zincblende structure (ZB), and cesium chloride structures (CsCl). Symbols represent calculated values, whereas the lines represent interpolations plotted to highlight general trends. a: Experimental formation energies are from Ref. [17]

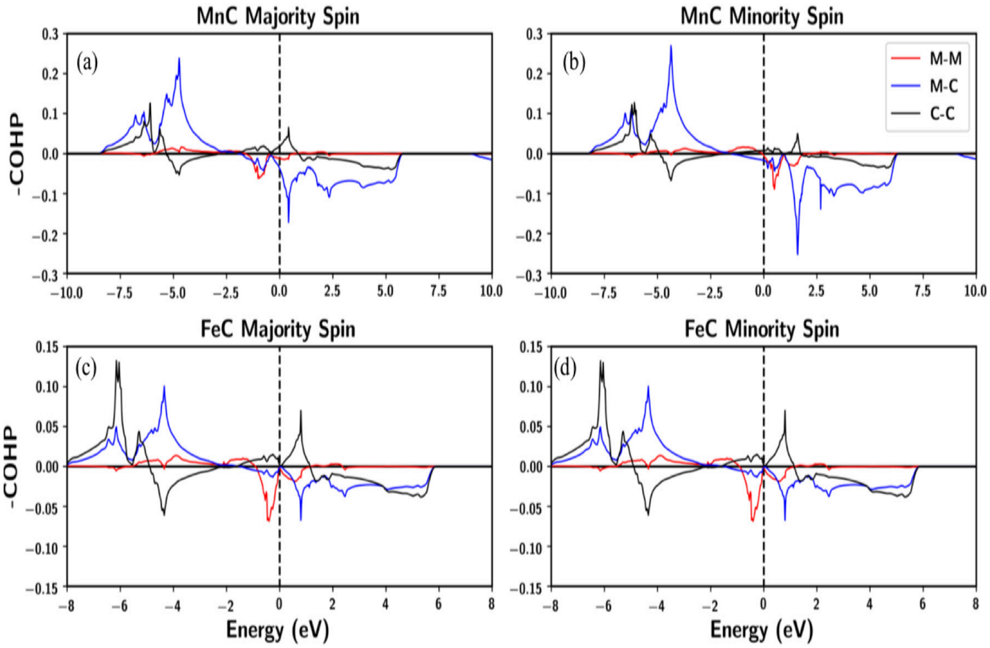

Figure 3-8: -Crystal Orbital Hamiltonian Populations (-COHP) of MnC (a and b) and FeC (c and d) individual bonding pairs, metal-carbon (M-C), metal-metal (M-M), and carbon-carbon (C-C), in rock-salt (RS) structures are shown. Positive values represent bonding states, whereas negative values represent anti-bonding states. The Fermi level is set to 0 eV.

Subtle deviations from the monotonic trend in formation energy described above are observed in TMCs where magnetic ordering plays a significant role. Both MnC and FeC adopt a ferromagnetic ground state caused by a Stoner instability [139] in which the intra-atomic exchange and electronic occupation at the Fermi level become sufficiently strong such that ferromagnetic ordering is preferred. The ferromagnetic rearrangement of electrons allows the majority-spin M-M bonding states to become fully occupied (fall below the Fermi level), while the minority-spin M-M antibonding states become unoccupied (rise above the Fermi level). This is illustrated by our spin-polarized COHP plots provided in Figure 3-8. A more in-depth analysis of ferromagnetic instabilities in RS TMCs can be found in our previous work [10].

Lastly, ZnC acts independently owing to its filled, nonbonding d shell, resulting in a slightly lower formation energy than the carbides of nearby metals. Because Zn has no unpaired electrons, it is more electropositive than nearby metals – e.g., Zn has an electronegativity of 1.66, whereas Cu has an electronegativity of 1.75 [12]. Therefore, the ionic contribution to the metal-carbon bonding is greater in ZnC than in TMCs with a comparable (lower) atomic number. Despite this difference, ZnC remains highly thermodynamically unstable, with an energy of 1.64 eV/atom above the convex hull formed by Zn and C.

As mentioned previously, we chose to focus on cubic structures as they are suspected to have promising mechanical properties. However, for the sake of completeness in our analysis, we also tested all ten TMCs in the hexagonal (wurtzite) structure, with the corresponding formation energies listed in Table 3.4. The results indicate the a hexagonal structure is preferred only for CrC and MnC. However, these still remain unstable with respect to decomposition into elemental ground states. We note that while most of the intermediate and late TMCs are thermodynamically unstable, many of those identified as dynamically stable may still be synthesizable using chimie douce techniques, which are commonly employed to access metastable states.

3.3.2 Bonding and mechanical properties

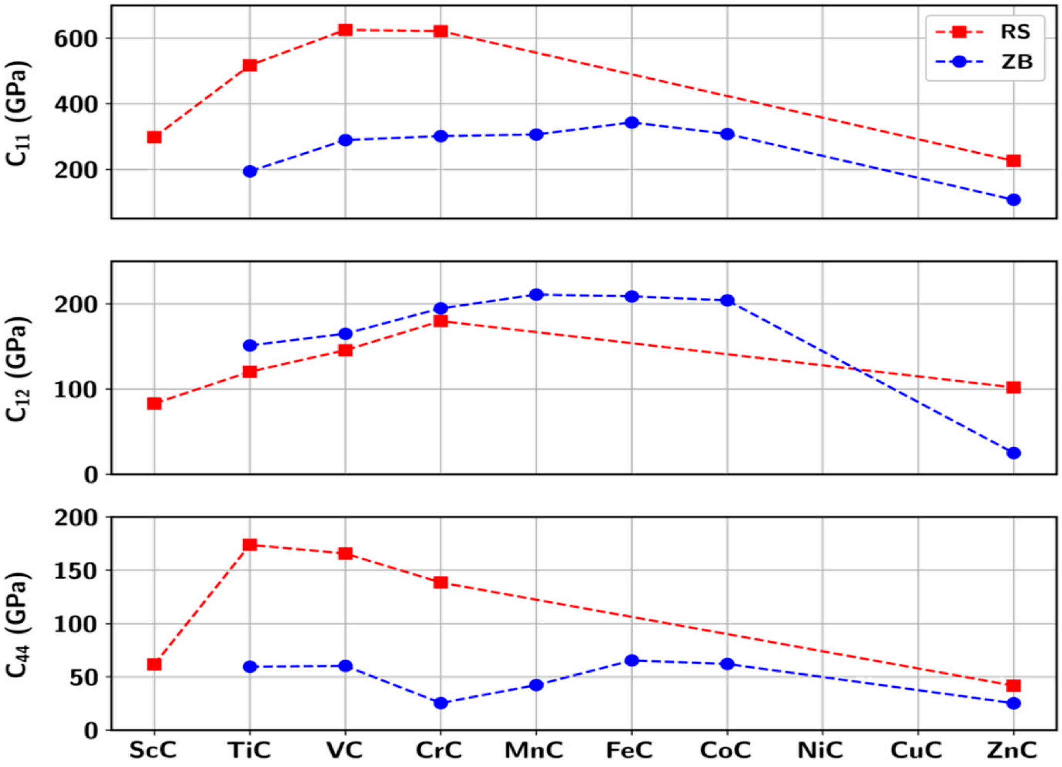

Figure 3-9: Calculated elastic constants (C_{11}, C_{12}, C_{44}) shown for all the stable/metastable compounds in the rocksalt structure (RS) and zincblende structure (ZB). Symbols represent calculated values, whereas the lines represent interpolations plotted to highlight general trends.

To study the mechanical properties, we look to the calculated elastic constants displayed in Figure 3-9 and provide an explanation of any trends throughout the TMCs by analyzing their electronic structure. From the elastic constants, derived quantities including bulk moduli, shear moduli, Vicker's hardness, Cauchy's pressure, Poisson's ration and Pugh's ratio are listed in Table 3.3, and are in good agreement with available experimental [140, 141] and calculated [79] values. The derived quantities such as bulk moduli, shear moduli, and Vicker's hardness are displayed in Figure 3-10 to gain insight into directly observable properties. For both the ZB and RS structures, we find that increasing valence electron concentrations leads to higher values of C_{11} and C_{12} throughout many of the stable TMCs. These changes raise the bulk moduli across the intermediate TMCs, with maxima occurring at FeC and CrC in ZB and RS respectively, corresponding to calculated bulk moduli of 252.9 GPa and 326.4 GPa.

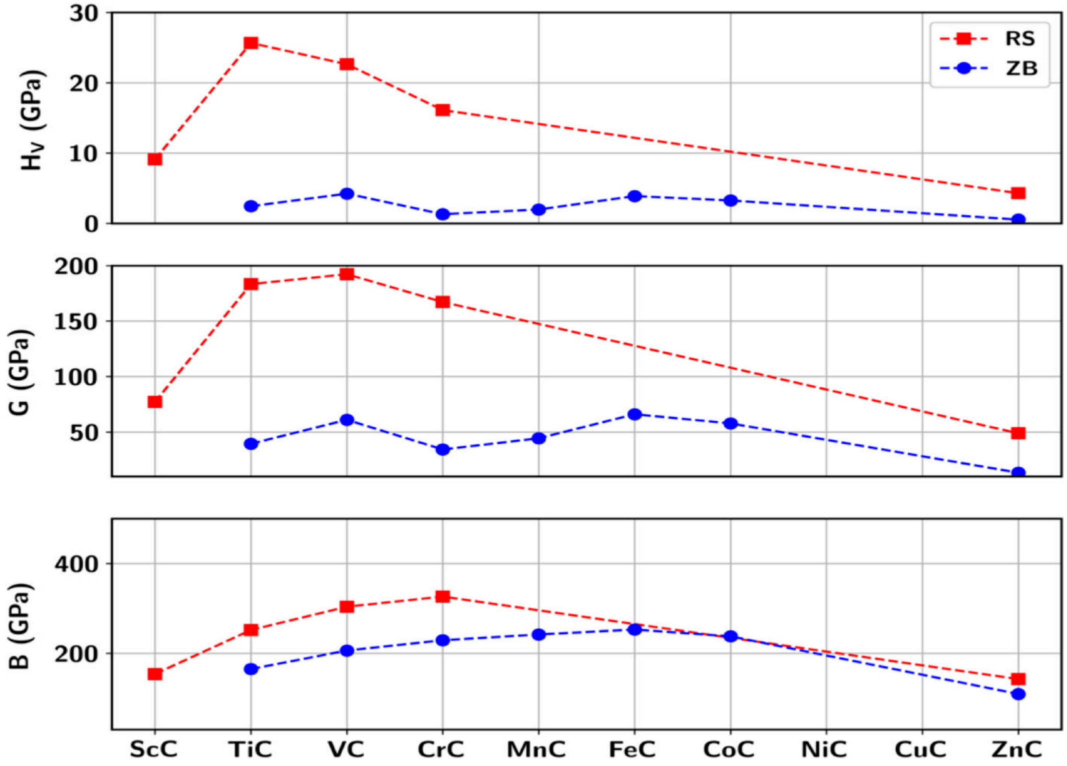

Figure 3-10: Correlation of Vickers hardness (H_V), shear modulus (G), and bulk modulus (B) with increasing group number across all stable/metastable 3d TMCs in the rocksalt structure (RS) and zincblende structure (ZB). Symbols represent calculated values, whereas the lines represent interpolations plotted to highlight general trends.

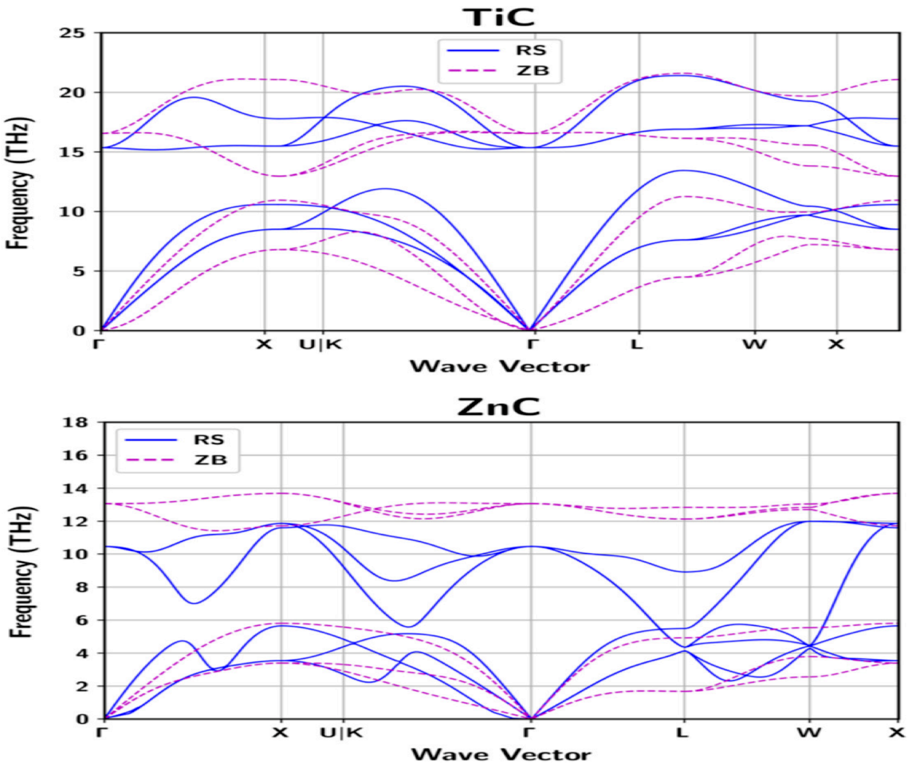

Figure 3-11: Phonon dispersion curves for TiC and ZnC, each of which represents extrema in the valence electron concentration of all stable compounds. To illustrate dynamic differences arising from varying structural factors, individual curves are plotted for the rocksalt (RS) and zincblende (ZB) structures.

The observed correlation between bulk modulus and group number can be attributed to three effects. First, the introduction of additional valence electrons (beyond a configuration of d^0 in TiC) mediates increased filling of the antibonding states. In this respect, the PDOS plots in Figure 3-6 illustrate that the Fermi level monotonically increases moving left to right across the periodic table, leading to enhanced occupation of the high-lying t_2 and e_g states in the ZB and RS structures respectively. From the COHP curves, these states are confirmed to be strongly antibonding in nature. Consequently, a higher occupation of the antibonding orbitals ensures that the structures are more resistant to compression given that such deformation will decrease the metal-carbon bond lengths and therefore raise the energy of the antibonding levels [142, 143]. The changing occupation of the antibonding orbitals are quantified by integrating COHP curves below the Fermi level, yielding ipCOHP values whereby larger (more positive) values signify enhanced bonding and decreased antibonding. As shown in Table 3.5, a maximum ipCOHP is achieved for TiC in both structures (2.23 eV and 1.55 eV for ZB and RS, respectively), whereas ipCOHP decreases across the later TMCs as the covalent interaction strength weakens. Second, the amount of electronic charge transferred between the metal and the carbon ions varies with the electronegativity of the TM. These changes, quantified by our Bader charge transfer values listed in Table 3.6, show that less charge is transferred between the ions in the late TMCs. Those TMCs with lower charge transfer tend to have higher bulk moduli as their attractive electrostatic force is decreased – hence, compression is favored less. Third, intermediate TMCs adopt structures with higher atomic densities owing to their short ionic radii. The increased strength of electrostatic repulsions acting across shorter distances encourages a more robust resistance to compression and therefore higher bulk moduli. In contrast, both electronic and steric effects lead to lower values of C_{11} and C_{12} in the late TMCs. ZnC, for example, has a filled d shell in which many of its valence electrons occupy non-bonding states as confirmed by the COHP curves shown in Figure 3-6. The corresponding orbitals respond weakly to compression, thus contributing little to the mechanical properties. Moreover, the atomic density of ZnC is relatively low, further reducing its bulk modulus.

There appears to be a more subtle relationship between C_{44} and group number across the TMCs that correlate quite closely with the calculated formation energies. Initially, C_{44} exhibits a large increase from ScC to TiC owing to a complete filling of the bonding orbitals as shown in the PDOS and COHP curves. For RS-structured compounds beyond TiC, a clear monotonic decrease in C_{44} is observed with increasing group number due to enhanced filling of the antibonding orbitals. Electrons occupying these states favor shearing as it reduces overlap between σ orbitals mediating nearest-neighbor bonds in the RS structure, thereby lowering the energy of the antibonding levels. Moreover, an increased electron count favors shearing as it enhances d orbital overlap between TM neighbors, thereby enabling metal dimer formation as discussed in the previous section. This further contributes to low values of C_{44} in the intermediate-late TMCs. Interestingly, changes in C_{44} are somewhat different for TMCs adopting the ZB structure. In this case, C_{44} displays a minimum for CrC before increasing back to relatively high values across the intermediate TMCs with a maximum at FeC. Then, a return back to low C_{44} is shown for the late TMCs such as ZnC. We propose that magnetic ordering likely plays a large role in lowering the occupation of antibonding states in the intermediate TMCs, as the splitting of majority- and minority-spin states reduces Pauli repulsion between like electrons. Similar trends may indeed be observed throughout compounds in the RS structure. However, most intermediate TMCs are not stable in this structure and therefore cannot be reliably considered.

To further investigate the effect of structure on the resulting mechanical properties, we directly compare the elastic constants calculated for each compound adopting RS and ZB structures. Figure 3-9 shows that C_{11} and C_{44} are consistently larger in the RS structure, C_{12} is more dominant in ZB. These differences arise from the underlying bonding configurations of each structure, as the direct σ overlap between metal d and carbon p orbitals in the RS structure ensure is highly resistant to uniaxial compression (C_{11}) and shearing (C_{44}). However, this same configuration is relatively dense and displays weaker resistance to transverse strain (C_{12}). In contrast, direct σ-bonding in the ZB structures requires some energy cost associated with hybridization as the original (atomic) d orbitals do not directly overlap with the carbon p orbitals. Furthermore, the tetrahedral coordination environments comprising the ZB structure are more readily distorted without causing substantial compression or elongation of individual bond lengths. These features lower the observed values of C_{11} and shearing C_{44}. Though, because compounds adopting the ZB structure have larger volumes, they readily accommodate volume dilation associated with higher values of C_{12}.

Differences in atomic interactions can also be illustrated through analysis of the phonon dispersion curves, which are plotted for TiC and ZnC in Figure 3-11. Between RS and ZB structures, there are several key distinguishing features. First, the slope of the acoustic branch near the Γ point is higher in the RS structure for the early TMCs (as shown by TiC), which suggests increased hardness and is in good agreement with our calculated elastic cosntants. In contrast, ZnC has very soft (low-frequency and weakly sloped) acoustic phonon modes near Γ when adopting the RS structure, which reflects weaker metal-carbon bonding due to the filled 3d states as supported by our earlier COHP analysis. On the other hand, increased covalent interactions in the ZB structure stabilize a raised slope in the acoustic branches near Γ for ZnC. Second, while the RS phonon dispersion curves display large anomalies (e.g., deviations in the longitudinal acoustic mode along Γ-X) that indicate strong electron-phonon coupling, in accordance with previous work [11], the ZB phonon dispersion curves display no noticeable anomalies. This highlights the difference in local interactions between metal d orbitals; electron-phonon coupling in RS is mediated by significant d-d overlap between nearest metal neighbors, whereas the distance between metal atoms in the ZB structure is too large to support any significant coupling via d-d interactions. Hence, unconventional superconductivity is suspected in the RS structure, but not in the ZB structure. Last, the optical frequencies of the ZB structure are shown to be higher than those in the RS structure for TiC and ZnC, possibly due to enhanced C-C interactions [144]. Despite the longer C-C bond lengths in the ZB structure relative to the RS structure, the tetrahedral coordination of the ZB structure is suspected to mediate stronger overlap of the p orbitals when compared to the octahedral coordination of the RS structure. This is supported by our calculated ipCOHP values, which show enhanced C-C interaction in the ZB structure (80 meV) relative to the RS structure (30 meV) for TiC. Interestingly, despite the increased mass mismatch between Zn and C (as opposed to Ti and C), significant acoustic/optical overlap is observed in RS-structured ZnC, further signifying the anomalous behavior of that compound due to its filled d shell and strong electron-phonon coupling.

Last, to consider these TMCs as applications in hard coatings, it is of interest to determine their hardness (measured by Vicker's hardness) and ductility. A material is expected to be ductile if its Pugh's ratio is below 0.5-0.6, its Poisson's ratio is above 0.25-0.28, and its Cauchy pressure is greater than zero [99] Here, we find that TMCs maintain much higher values of Vicker's hardness in the RS structure as opposed to ZB. This difference can be traced back to the lower values of C_{44} found in the ZB structure as discussed in the previous paragraph, which preclude them from being used for high-hardness coating applications. As for the RS materials, a maximum hardness of 25.66 GPa is identified in TiC, matching with previous findings [145]. Though, both VC and CrC also display reasonably high hardnesses of 22.63 and 16.11 GPa respectively. Of these compounds, both TiC and VC are predicted to be brittle according to their reported values of Pugh's ratios, Poisson's ratios, and Cauchy pressures in Table 3.7. For the remaining stable TMCs, their properties instead show ductile behavior. Therefore, although TiC is the hardest material studied here, we propose that CrC may be preferred in applications where toughness is also required.

3.4 Conclusions

The work presented here illustrates how valence electron concentration and structure play dominant roles in controlling the stability and mechanical performance of 3d TMCs. In particular, for early TMCs adopting the RS structure, our findings confirm the importance of filled bonding states to enable robust stability and exceptionally high hardness. Our results also provide insight into the source of the instability of the RS structure for the intermediate TMCs, which we have shown to be due to enhanced metal-metal interactions and weakened metal-carbon bonds. With regards to the ZB structure, our calculations reveal several new compounds that are metastable and potentially synthesizable if the thermodynamic ground state can be avoided (e.g., via *chimie douce* techniques). Our results also indicate that - although their mechanical properties are not as promising as those displayed by TMCs in the RS structure - due to their potentially interesting and unexpected electronic properties, they may warrant further investigation. Our results also indicate that all 3d TMCs are unstable under ambient conditions in the CsCl structure, due to the fact that the resulting dense eight-fold coordination is inconsistent with covalent bonding. However, if these structures can be stabilized in high-pressure conditions, then there exists a possibility to find new and interesting properties such as unconventional superconductivity previously reported [11] in several RS TMCs.

Based on the findings presented above, we focus on the RS structure and propose several guiding principles for the design of novel TMCs that may be used in next-generation hard coating applications. First, to maximize hardness and stability, a valence electron count of four (e.g., TiC) is critical. In this case, covalent M-C interactions dominate owing to the completely filled bonding orbitals, whereas metallic M-M interactions are minimized because of the d^0 configuration (empty metal orbitals). Second, if ductility rather than hardness is to be optimized, then a valence electron count well beyond four is favorable. In this case, M-M interactions play a larger role as the non-bonding d orbitals become filled, which favor shearing deformations that allow the d orbitals to overlap. However, it is also important to prevent over-filling of the d orbitals so that the structure does not become dynamically unstable with respect to metal dimer formation (e.g., as in MnC). Third, to achieve tough materials with a balance between hardness and ductility, one may consider a valence electron count that is only slightly higher than four. Because an increase beyond four electrons causes enhanced ductility but worsened hardness, we suggest that an optimal tradeoff may be realized through ion substitution – e.g., between TiC and CrC. By forming solid solutions with controllable compositions, the mechanical properties may be fine-tuned by varying Ti-Cr content. Although past works suggest that high temperatures are necessary to form such solutions [146], alternative techniques such as high-energy ball milling or doping (e.g., high-entropy alloys) may be considered in the future.

Chapter 4

Mechanism of Stacking Fault Formation in Metal(100) Heteroepitaxial Growth

4.1 Introduction

Strain in heteroepitaxial thin-film growth can lead to a variety of interesting morphological and structural effects [18, 19, 147–162] including dislocation formation [149, 155, 162] and the Asaro-Tiller-Grinfeld instability [147, 148, 161], as well as island-shape transitions [18, 19, 150, 151, 153, 154, 156, 158–160] and stacking faults [19, 157]. Of particular interest are the experiments carried out by Müller *et al.* [18, 19, 152, 153] in which both submonolayer and multilayer Cu islands grown on a Ni(100) substrate (corresponding to 2.7% compressive strain) were found to form ramified island shapes followed by the subsequent formation of 'stripe' defects corresponding to stacking faults.

While it was initially thought [18] that the ramified island shapes might be due to the coalescence of anisotropic (rectangular) islands whose anisotropy was due to strain [151, 163], theoretical calculations of the critical island-size or armwidth L_c for anisotropy [164] indicate that for Cu/Ni(100), L_c is many orders of magnitude larger than the critical value (22 b, where b is the nearest-neighbor distance) observed for the formation of ramified islands. Instead, it was found [164] that this corresponds to the critical island-size for strain-induced in-plane multi-atom 'pop-out' events which lead to a competition between open and closed island step-edges as is observed experimentally [18].

Kinetic Monte Carlo (KMC) simulations [164] which take these events into account were found to reproduce the experimentally observed submonolayer island morphologies at 250 K and 300 K. However, since these were on-lattice simulations, they were unable to explain the subsequent formation of stacking faults. We note that stacking faults have been found to play an important role in determining the quality of strained thin films. For example, by blocking the extension of threading dislocations in GaN growth [165], as well as by blocking dislocation motion in ultra-hard high-entropy alloy thin films [166], stacking faults have been shown to improve the quality of strained thin films. Accordingly, in order to gain a better understanding of the energetics and kinetics of stacking fault formation as well as to separate out chemical effects from strain effects, we have carried out fully off-lattice temperature-accelerated dynamics (TAD) simulations of the submonolayer growth of Cu islands on a biaxially strained Cu substrate.

In order to maximize the boost due to accelerated dynamics so that we can simulate growth on time-scales close to experiments, our simulations were carried out using a relatively low substrate temperature T = 200 K. This value also implies that the average island size will be significantly smaller than the typical system-size that can be efficiently simulated using TAD [45, 164]. In addition, since the substrate temperature was relatively low compared to experiment, our simulations were carried out using a value of the compressive strain (4%) which is somewhat larger than the value (2.7%) for Cu/Ni(100) growth. The choice of this value was also motivated by preliminary calculations in which we found that the barrier for vacancy diffusion in a Cu monolayer on a Ni(100) substrate decreases linearly with increasing compressive strain, and then abruptly goes to zero at a strain value of 4.7%.

Somewhat surprisingly, we find that stacking fault formation occurs in our simulations. Our results also indicate that the formation of islands plays a key role in promoting stacking fault formation by lowering the barrier for vacancy formation as well as decreasing the vacancy formation energy. Once two substrate vacancies are formed and diffuse to form the appropriate configuration near an island, this leads to the formation of a stacking fault in both the substrate and island, with a morphology very similar to the structures suggested by Müller *et al.* [18, 19, 153] based on their experiments.

Our results also indicate that while the activation barrier for stacking fault formation is very high (1.0 eV), due to the presence of a large number of low-frequency vibrational modes which increase the saddle-point entropy, the transition rate prefactor is also unusually large (8.8×10^{27} s^{-1}). As a result, the average time-interval for this transition is only 3.2 msec. Similarly, an analysis of the entropy of the stacking fault (SF) state indicates that the reverse prefactor is much smaller, and that the free energy of the SF state is lower than that of the initial state. These results indicate that in the presence of compressive strain, the formation of stacking faults is both kinetically and thermodynamically favorable at sufficiently high temperatures.

The organization of this Chapter is as follows. We first briefly discuss our TAD simulations in Sec. 4.2 and then present our results in Sec. 4.3. Finally, in Sec. 4.4 we summarize our results and also discuss the implications for stacking fault formation in Cu/Ni(100) growth.

4.2 Temperature-accelerated dynamics simulations

In order to access experimental time-scales while including both the effects of strain and on-lattice and off-lattice transition pathways, we have carried out temperature-accelerated molecular dynamics (TAD) simulations [15, 44, 46, 47]. As discussed in more detail in Refs. [15, 44–46], TAD simulations are based on the assumption of harmonic transition-state theory along with the use of a molecular dynamics simulation at a high temperature (T_{high}) which is used to accelerate the search for the state-to-state pathways and transition times at a lower temperature (T_{low}). In particular, for each visited state, a high temperature basin-constrained MD simulation is first carried out to determine the possible escape pathways along with the corresponding high-temperature transition times and activation barriers. Once sufficient information has been accumulated, the time and pathway for the first transition which will occur at the desired low temperature T_{low} can be determined and this transition is then accepted. This process is then repeated for a given, desired interval of low-temperature time.

Our simulations were carried out using an embedded-atom method (EAM) potential [167] with a Cu substrate consisting of six (100) layers with width L = 10 a (where a is the lattice constant of copper). The three bottom layers were held fixed while the temperature of the three top layers was controlled by a Langevin thermostat [168] with a friction coefficient of 10^{12} s^{-1}. In order to include the effects of strain, the substrate was compressed biaxially by 4% while periodic boundary conditions were assumed in the $x-y$ (in-plane) directions. In order to simulate submonolayer growth, Cu atoms were deposited randomly with a deposition rate of 1 monolayer (ML)/sec while the substrate was equilibrated at 200 K. Since one monolayer corresponds to 200 atoms this implies a deposition rate of 200 atoms/sec or equivalently an average time-interval between depositions of 0.005 sec. We note that while this deposition rate is still significantly faster than that used in experiments (typically $10^{-3} - 10^{-2}$ ML/sec) it is still many orders of magnitude slower than is typically used in molecular dynamics simulations.

For each deposition, the Cu atoms were launched normally from a random position above the substrate at a height equal to that of the highest point of the film plus the cutoff distance $r_{cut} = 5.51$ Å with an initial kinetic energy $K_i = 2\ k_B T_m = 0.23$ eV (where k_B is the Boltzmann constant and $T_m = 1358$ K is the melting temperature of Cu). Molecular dynamics of the entire system was then carried out for 4 ps before continuing TAD simulations until the time for the next deposition event.

In order to maximize the acceleration or "boost" while minimizing the number of attempted (but not accepted) high-temperature transitions, our TAD simulations were carried out with a high temperature $T_{high} = 650$ K. In our TAD simulations a minimum value of the prefactor $\nu_{min} = 10^{12}/s$ was also assumed along with an uncertainty $\delta = 0.1$. The total number of atoms deposited in our simulations (27) corresponded to 0.135 monolayers (ML), while the total time simulated (at 200 K) until the formation of a SF was approximately 0.14 sec. While TAD automatically calculates the activation barriers for all accepted events, for selected events we also calculated the corresponding forward and reverse prefactors (ν) using the Vineyard expression [169] $\nu = \frac{\prod_{i=1}^{3N} \nu_i}{\prod_{i=1}^{3N-1} \nu_{s,i}}$ where ν_i ($\nu_{s,i}$) are the normal mode frequencies for the initial state (saddle point) respectively, and N is the number of moving atoms. In order to monitor the evolution of the free energy, including vibrational contributions, we have also calculated the change in free energy at $T = 200$ K with respect to a reference state with energy E_0 using the harmonic approximation expression $F = (E - E_0) + k_B T_{low}\ ln \prod_{i=1}^{3N} \frac{\nu_i}{\nu_{0,i}}$ where E (E_0) and ν_i ($\nu_{0,i}$) are the minimized energy and normal mode frequencies of the selected (reference) state.

4.3 Results

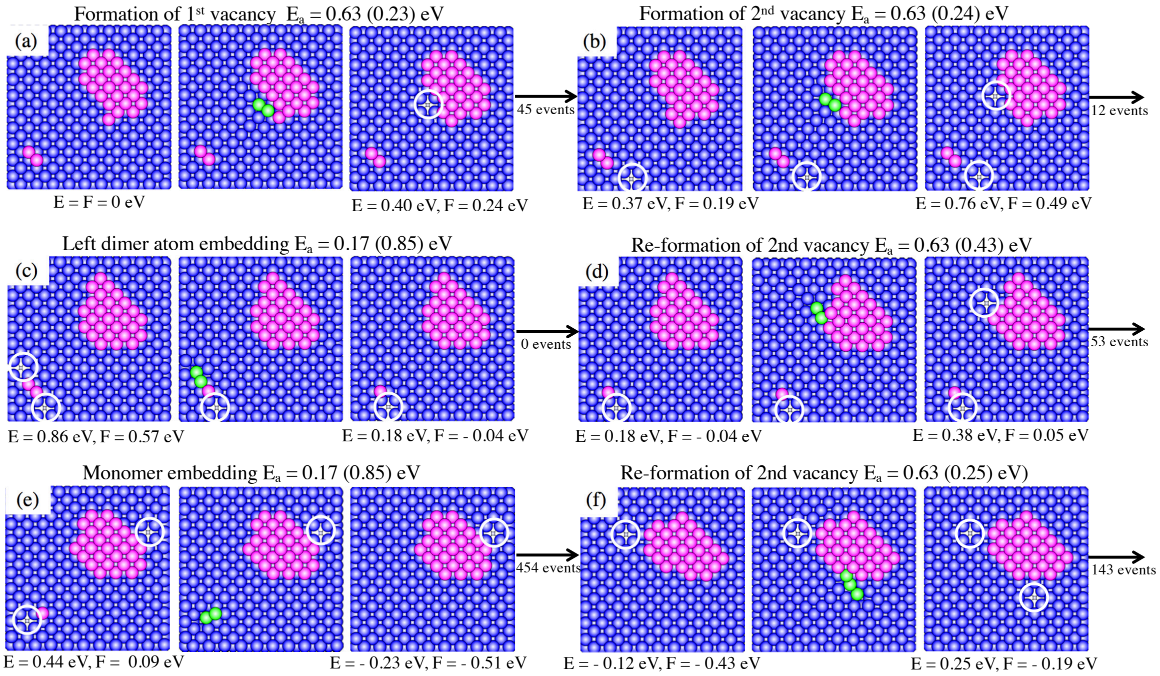

Figure 4-1: Sequence of key events leading up to stacking fault formation (a) Formation of first vacancy (b) Formation of second vacancy (c) Left dimer atom embedding and vacancy annihilation (d) Re-formation of second vacancy (e) Monomer embedding and vacancy annihilation (f) Re-formation of second vacancy.

Fig. 4-1 shows 6 of the key events which occur after the deposition of 0.135 ML and prior to the formation of a stacking fault at $t \simeq 0.14$ sec. For each event, the initial, saddle, and final minimized configurations are shown along with the corresponding forward activation barriers. (The reverse activation barriers are shown in parentheses.) Also shown for both the states before and after each transition are the energy (E) and free energy (F) relative to the starting configuration in Fig. 1(a). As can be seen, due to the small system size as well as the relatively large rate of monomer diffusion (624 hops/sec) and dimer diffusion (8,532 hops/sec) at 200 K, at this coverage there is only one island containing 25 atoms in the system, along with a dimer.

As indicated in Fig. 4-1 (a), the first key event leading to the formation of a stacking fault corresponds to the pop-out of a Cu atom from the substrate, leading to the formation of a substrate vacancy. As indicated by the middle (saddle-point) configuration, this involves a collective move of two atoms, in which one atom leaves the substrate and attaches to the island at a kink site, while the second atom replaces the first atom, leaving a vacancy behind. We note that the barrier for vacancy formation in this case (0.63 eV) is significantly smaller than that for vacancy formation on the bare substrate away from the island (0.92 eV) or for vacancy formation at a straight island edge away from a kink (0.81 eV). In addition, the reverse barrier (0.23 eV) is higher than the barrier (0.13 eV) for the vacancy to diffuse away from the island, thus allowing the vacancy to diffuse away before it can be annihilated. As also shown in Fig. 4-1 (a), while the energy increases significantly due to the increase in the number of missing nearest-neighbor bonds, the increase in the free energy is significantly smaller due to the increase in vibrational entropy.

Due to the relatively low diffusion barrier for vacancy diffusion, one would expect the vacancy to migrate rapidly via single hops away from the island. Instead, since the barriers for a variety of collective string-like moves are comparable, while the corresponding prefactors are on the order of 100 times higher, after a few hops back and forth near the island edge, the vacancy then moves by a sequence of 3 long-distance string-like moves [167] involving 4-6 substrate atoms, until it is near the dimer as shown in Fig. 4-1 (b). A variety of additional long-distance vacancy diffusion moves are then carried out along with a number of island re-arrangements after which the island returns to its initial state.

As shown in Fig. 4-1 (b), a second vacancy is then formed near an island kink site with the same activation energy as for the first. A variety of low-barrier collective vacancy diffusion moves then occur, including a 7-atom move which includes both the island and substrate, after which both vacancies are near the dimer as shown by the first picture in Fig 4-1 (c). This leads to the very low activation barrier vacancy annihilation event shown in Fig. 4-1 (c) in which the left dimer atom pushes a nearby substrate atom into the vacancy and replaces it. While the free energy at this point is slightly lower than that of the initial state, immediately after embedding the free energy is again increased by the re-formation of a second vacancy at a kink site, as shown in Fig. 4-1 (d). Even though the activation barriers are the same, as discussed in more detail below, the energy increase for this event is almost 0.2 eV smaller than for the vacancy formation event shown in Fig. 4-1 (b).

Figs. 4-1 (e) and (f) show the two key remaining transitions leading up to the stacking fault transition shown in Fig. 4-2. In particular, Fig. 4-1 (e) shows the embedding of the remaining monomer via an exchange process which involves a nearby substrate atom and one of the two substrate vacancies. The barrier for this process (0.17 eV) is equal to that for the first embedding process, while the resulting free energy is now significantly lower than that for the initial state. This is then followed by a large number (454) of low-barrier collective vacancy diffusion processes as well as some island re-arrangement, leading to the initial configuration shown in Fig. 4-1 (f). A second substrate vacancy is then re-formed near an island kink site via a collective 3-atom pop-out event with the same barrier (0.63 eV) as for the other two vacancy formation events. As can be seen, the system now consists of two substrate vacancies and one island containing 27 atoms, while the free energy remains negative with respect to the configuration shown in Fig. 4-1 (a).

While a total of 570 events take place during the time from the first configuration in Fig. 4-1 (a) to the final configuration in Fig. 4-1 (f) - due to the relatively low barriers of these events - this corresponds to a time difference of only 1.3 msec. A comparison of the island configurations indicates that while the vacancy formation transitions in Fig. 4-1 (b) and Fig. 4-1 (f) correspond to the creation of two additional first-, second-, and third-neighbor "bonds" in the island, for the transition shown in Fig. 4-1 (d) only one additional second-neighbor bond is created. This leads to a reduction in the total strain energy and explains the reduced increase in the total energy for the vacancy formation event in Fig. 4-1 (d) compared to those shown in Fig. 4-1 (b) and (f).

As shown in Fig. 4-2, after 143 additional low-barrier events (including primarily vacancy diffusion events and some island re-arrangement) a collective move involving 69 atoms occurs, leading to the formation of a stacking fault. We note that the activation barrier for this event is extremely large (1.01 eV) which implies that with a normal prefactor of the order of $10^{13}s^{-1}$ it would take a time of the order of 10^{12} sec before occurring. However, the Vineyard prefactor for this event is also extremely large ($\nu = 8.8 \times 10^{27}$ s^{-1}). This implies an average waiting time at 200 K of only 3 msec, which is somewhat larger than but still consistent with the elapsed low-temperature time of approximately 1.5 msec. As indicated in Fig. 4-2 the reverse prefactor is significantly smaller, and as a result the reverse transition rate is negligible at 200 K.

Examination of the normal modes also indicates that the extremely large forward prefactor is primarily due to the presence of a large number of vibrational modes at the saddle-point whose frequencies are slightly lower than for the initial state. Similarly, the much smaller reverse prefactor is due to the presence of a large number of low-frequency modes in the final stacking fault state. These results indicate that both the transition state and the final SF state have much higher vibrational entropy than the initial state. This is consistent with the fact that even though the energy of the stacking fault state is 0.3 eV higher than that of the initial state, the total relative free energy at 200 K (-0.25 eV) is reduced by 0.27 eV. We have also carried out TAD annealing simulations at 200 K in order to test the stability of the stacking fault configuration. As expected, for the maximum annealing time studied (1.1 sec) the stacking fault remains stable.

Fig. 4-3 (a) shows a close-up of the stacking fault (SF) configuration which includes two rows of the top substrate layer as well as two rows of the island, each of which have shifted by one-half the nearest-neighbor distance. As can be seen, there is still a vacancy in the substrate next to the stacking fault as well as a partial vacancy in the stacking fault itself. Fig. 4-3 (b) shows a view of the same configuration in which the top substrate layer in the bottom right corner of the system has been removed (see caption). As can also be seen, one row of atoms in the layer below the substrate has also shifted by one-half the nearest-neighbor distance, thus indicating the formation of small (111) facets along the stacking fault defect.

For comparison, the suggested structure [152] for the formation of stripe defects in Cu/Ni(100) growth after 3 ML have been deposited at 350 K is also shown in Fig. 4-3 (c). As can be seen, except for the difference in the number of layers, the two structures are essentially identical. In addition, an analysis of the configuration in Fig. 4-3 (b) indicates that for the minimized (0 K) state, the atoms in the surface stripe (stripe below the surface) have also shifted up by an amount $\Delta h = 0.35$ Å (0.33 Å) from their initial positions. Due to the presence of relaxation, this amount is close to but somewhat smaller than the prediction ($\Delta h \simeq 0.4$ Å) based on a "hard-sphere model" which takes into account the difference in geometry between a four-fold hollow site and a bridge site. We note that the experimentally measured value [19] obtained for single-row stripes formed in second-layer Cu/Ni(100) islands at 350 K ($\Delta h = 0.5 \pm 0.15$ Å) is slightly higher than this value, perhaps due in part to the effects of thermal expansion. For comparison, also shown in Fig. 4-3 (d) is an STM picture which indicates a single-row stripe SF in one of the Cu islands grown on Ni(100) at 350 K after only 0.35 ML have been deposited.

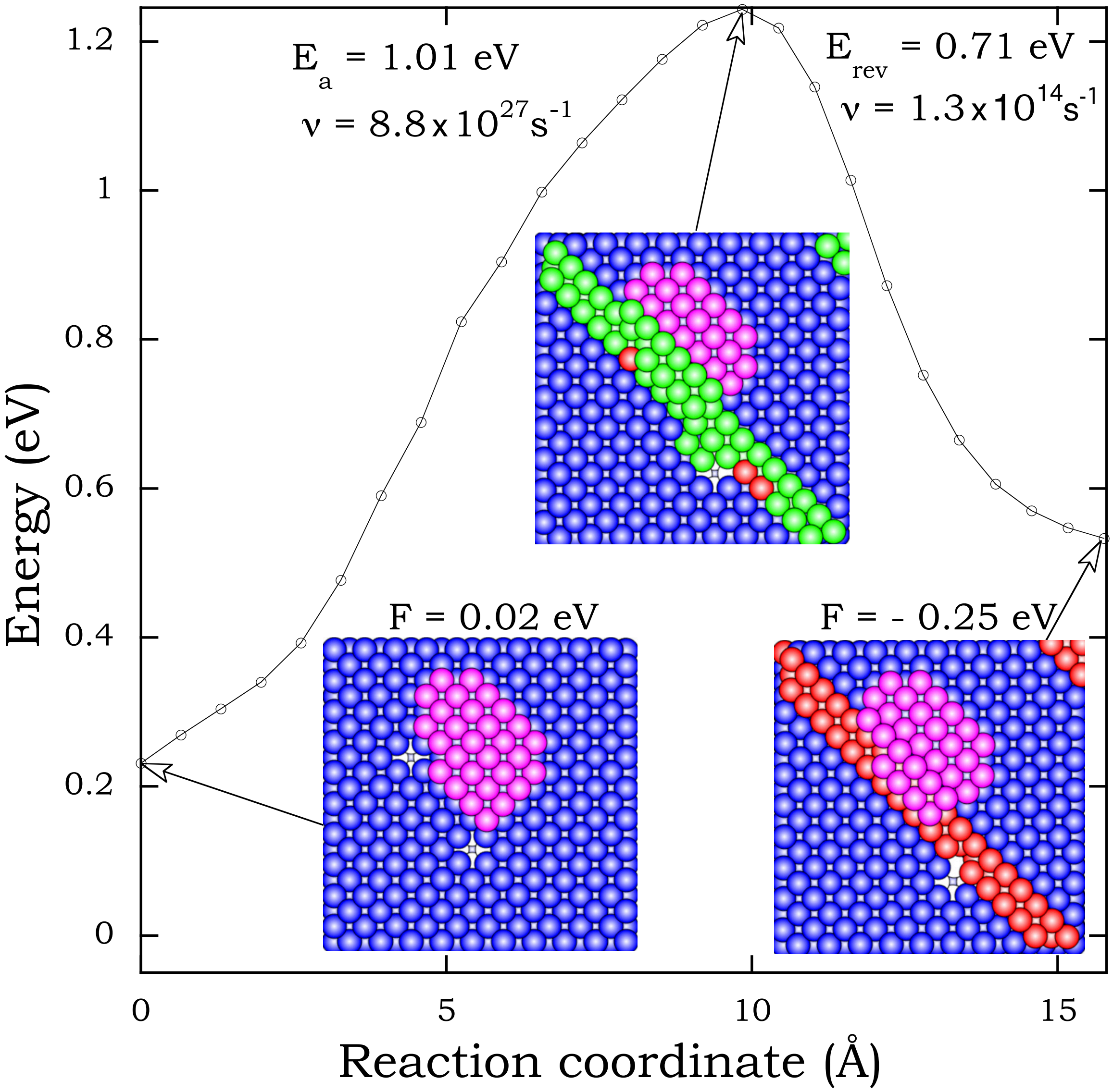

Figure 4-2: Nudged elastic band results for stacking fault formation transition. Top picture indicates saddle-point configuration while bottom two pictures correspond to initial and final minimized configurations.

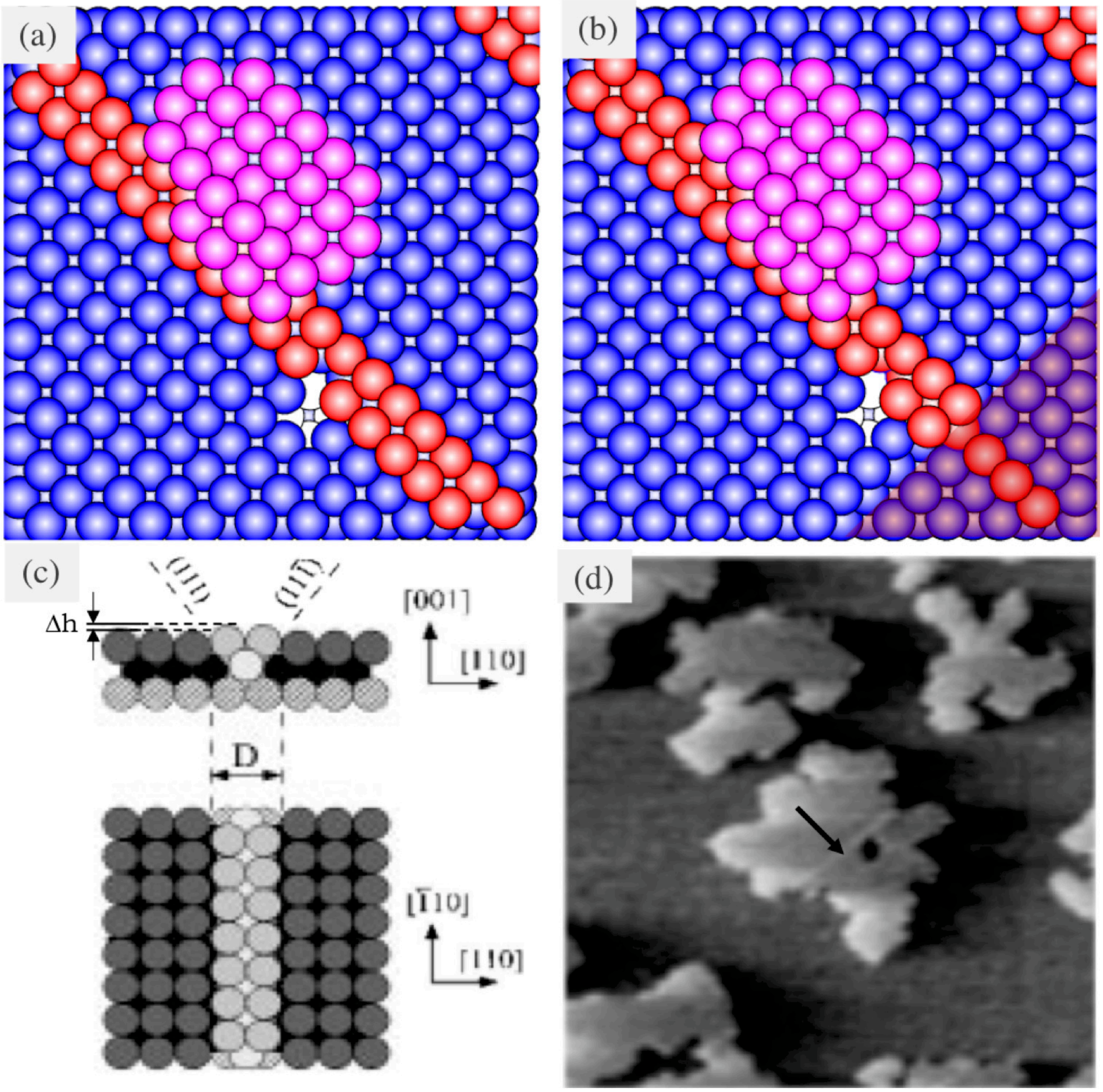

Figure 4-3: (a) Close-up of final configuration shown in Fig. 2 (b) Same as (a) but with top substrate layer atoms removed in bottom right-hand corner. Stacking fault atoms in row below substrate layer are shown in red, while remaining atoms are purple. (c) Faceting model for Cu/Ni(100) [18] (d) STM picture (from Ref. [19]) showing single-Cu islands grown on Ni(100) at 350 K after 0.35 ML have been deposited. Arrow points to single-row stripe in center island.

4.4 Summary

In order to understand the effects of strain on defect formation in the early stages of heterepitaxial growth, as well as to separate out chemical effects from strain effects, we have carried out temperature-accelerated dynamics simulations of the growth of Cu on a strained Cu(100) substrate at $T = 200$ K, with a deposition rate (1 ML/s) close to typical experimental values. Since our simulation temperature is somewhat lower than typical experimental temperatures (T $\geq$ 300 K), in order to observe defect formation on the time scale of our simulations, our simulations were carried using a somewhat larger value of compressive strain than that in Cu/Ni (100) growth.

Our results indicate that, in addition to compressive strain, the formation of both islands and vacancies is crucial to stacking fault formation. In particular, we find that when two substrate vacancies have formed and have reached the right configuration near an island, a stacking fault is formed. Interestingly, while the activation barrier for this many-atom collective event is extremely large (1.0 eV), the prefactor is also "gigantic" (e.g. $8.8 \times 10^{27} s^{-1}$), and as a result the average time-interval for this transition is only approximately 3.2 msec. The large prefactor is due to the presence of a large number of vibrational modes at the saddle-point whose frequencies are slightly lower than for the initial state. Similarly, the much smaller reverse prefactor is also due to the presence of a large number of low-frequency modes in the final stacking fault state. As a result, even though the energy is higher, the free energy of the stacking fault state is lower than that of the initial state. We note that in previous work on the transformation of 20-45 atom vacancy voids to stacking fault tetrahedra in unstrained bulk Cu, a very large prefactor with a correspondingly large energy barrier and number of atoms involved in the transition has also been observed due to entropic effects [170].

Our results also indicate that the presence of islands is crucial for the formation of vacancies. In particular, while the presence of compressive strain lowers the energy for vacancy formation in the bare substrate from 1.54 eV to 1.32 eV, this still leads to a negligible equilibrium vacancy density. Similarly, at 200 K, the difference in free energy of a vacancy-monomer pair and that of the bare substrate is approximately 1.27 eV. In contrast, in the presence of compressive strain the formation energy of a vacancy at an island kink site is significantly lower (ranging from 0.2 eV to 0.4 eV depending on the kink site) while the free energy increases by only 0.1 - 0.3 eV depending on the island configuration. Thus, island formation and growth play a crucial role in promoting vacancy formation.

In addition to these results, a number of other interesting effects have been observed in our simulations. In particular, we found that - rather than migrating via single-atom hops - since the barriers for collective moves are comparable in the presence of compressive strain while the prefactors are on the order of 100 times higher, substrate vacancies diffuse primarily via collective (3-6 atom) string-like moves. In contrast, in the absence of strain the barriers for vacancy diffusion are significantly higher ranging from 0.44 eV for single-atom moves to 0.6 - 1.0 eV for string-like moves. We also found that while the value of the barrier for monomer diffusion is significantly reduced (from 0.51 eV to 0.42 eV) in the presence of strain, the key barrier for dimer diffusion (for which the corresponding transition involves one atom of the dimer hopping from a nearest-neighbor site of the other dimer atom to that atom's next-nearest neighbor site) is also significantly reduced (from 0.49 eV to 0.38 eV). Interestingly, the next-nearest neighbor dimer separation was also found to be significantly reduced in the presence of strain (2.72 Å with strain versus 3.3 Å without strain) even though the nearest-neighbor separation (2.47 - 2.49 Å) is almost the same with and without strain.

Finally, it is interesting to compare our simulation results with those obtained experimentally for Cu/Ni(100) growth at 350 K. While there is no compressive strain in the substrate in this case, there is a 2.7% compressive strain in the islands. As a result, the initial (single row) stripes occur in the islands (see Fig. 4-3 (d)) rather than the substrate-plus-island as in our simulations. In addition, the formation of multilayer SFs only occurs after the deposition of more than one layer.

Since our results indicate that vacancies play an important role in the formation of SFs during the growth of Cu on strained Cu(100), we conjecture that this is also the case in Cu/Ni(100) growth. As discussed in the Introduction, it has been previously shown [164] that for Cu/Ni(100) growth, the barrier for in-plane pop-out events at island edges with kinks decreases significantly with island-size. While these events have already been demonstrated [164] to lead to the ramified island shapes observed experimentally, they can also lead to vacancy formation within the island. Accordingly, we speculate that one possible pathway for stacking fault formation in Cu/Ni(100) submonolayer islands might involve the simultaneous formation of two or more vacancies in an island, perhaps due to in-plane pop-out events, since such events are kinetically favorable for sufficiently large islands and/or temperatures. It would be of interest to carry out simulations of Cu islands on Ni(100) for larger island-sizes and higher temperatures to see if this is the case.

Chapter 5

Dependence of island morphology on strain in Cu/Cu(100) growth

5.1 Introduction

In addition to the results discussed in Chapter 4 for the case of growth on a 4% compressively strained Cu(100) substrate, we have also carried out additional TAD simulations for both 2% compressive strain and 8% tensile strain. We have also studied the general strain dependence (ranging from -6% to +8%) of the activation barriers for Cu monomer and dimer diffusion via hopping and exchange on a biaxially strained Cu(100) substrate.

5.2 Simulations and Calculations

Our growth simulations and calculations of the strain-dependence of the activation barriers for monomer and dimer diffusion were carried out using an embedded-atom method (EAM) potential [167] with a substrate consisting of six Cu(100) layers with width L = 10 a (where a is the lattice constant of Cu) with the three bottom layers held fixed. In order to include the effects of strain, the substrate was strained biaxially, with the misfit ranging from -6% (compressive strain) to +8% (tensile strain) while periodic boundary conditions were assumed in the in-plane directions. In order to study the dependence of the dominant transport mechanisms on strain, nudged elastic band calculations were carried out for both the case of hopping and exchange.

In order to simulate submonolayer growth on time-scales close to experiment while also taking into account strain-induced activated events, our simulations were carried out using temperature-accelerated dynamics (TAD) [15, 44, 46, 47, 164]. While we have already described this method in detail in Ref. [1], here we note that it involves the use of a basin-constrained molecular dynamics (MD) simulation at a high temperature T_{high} to accelerate the search for the next activated event which will occur at low temperature T_{low}. In order to maximize the "boost" or acceleration, we have carried out our growth simulations at a relatively moderate value of T_{low} ($T_{low} = 200$ K) while the high-temperature MD simulations were carried out with $T_{high} = 650$ K. In our simulations, Cu atoms were deposited randomly with a deposition rate of 1 monolayer (ML)/sec. While this deposition rate is still somewhat faster than that used in experiments it is still many orders of magnitude slower than is typically used in molecular dynamics simulations. As already indicated, our growth simulations were carried for both the case of 2% compressive and 8% tensile strain.

5.3 Results

5.3.1 Dependence of dominant diffusion mechanisms and barriers on strain

Fig. 5-1 shows our results for the dependence of the activation barriers for monomer and dimer hopping and/or exchange on strain. As can be seen, in the absence of strain. monomer and dimer hopping dominate over exchange, while the barrier for dimer diffusion (0.49 eV) is actually slightly lower than that for monomer diffusion (0.51 eV). With increasing compressive strain the activation barriers for hopping decrease further while the barriers for exchange increase. As a result, for the case of compressive strain and/or less than 2% tensile strain, hopping dominates over exchange. In contrast, for greater than 2% tensile strain, the activation barriers for monomer and dimer exchange are smaller than for hopping. As a result, exchange dominates over hopping.

We note that these results are qualitatively similar to those previously found by Ratsch [171] for Ag monomer diffusion on Ag(100), while the approximately linear dependence on strain is also in good agreement with the theoretical prediction [172] that the activation barrier should depend linearly on misfit. In the case of monomer hopping the increase in the activation barrier with increasing tensile strain may be explained [171] by the fact that this leads to a greater variation in the potential energy surface. In contrast, the decrease in the exchange barrier with increasing tensile strain is due to the fact that this leads to more space, which is needed for the exchange mechanism, and also weakens the strength of the interatomic bonds in the substrate layer.

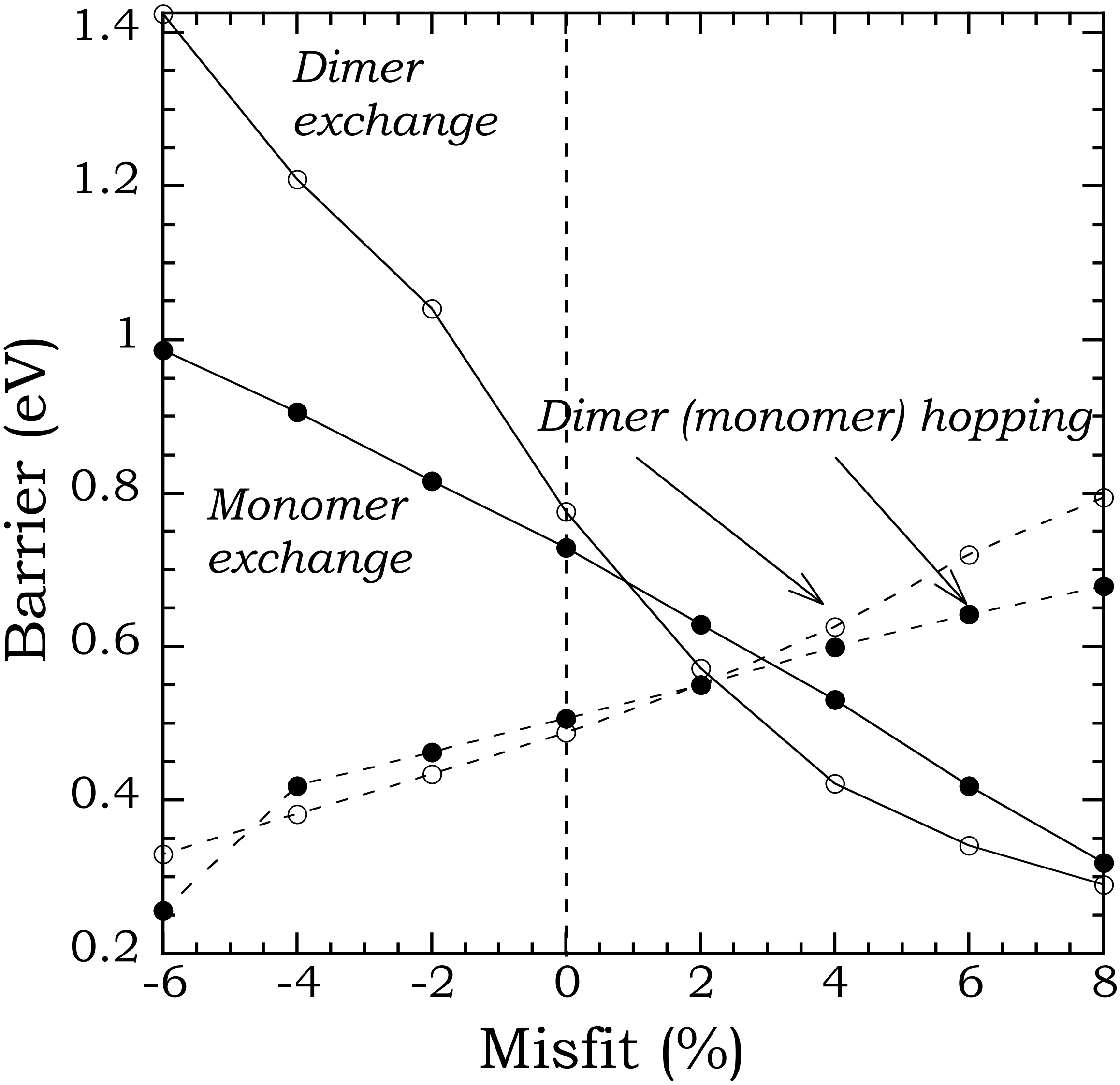

Figure 5-1: Energy barriers for monomer and dimer hopping and exchange on strained Cu(100) as a function of misfit.

5.3.2 Submonolayer growth with 2% compressive strain

Previously we have carried out KMC simulations of Cu/Ni(100) growth [164] with the same deposition rate and island density as in experiments [18, 153] which were able to explain the observed ramified island morphology. However, due to the low experimental deposition rate (0.0015 ML/sec) and island density, and high growth temperature (250 K) we were unable to carry out full TAD simulations in this case. Accordingly, in order to compare with these results and also take into account all possible collective events which might not be included in KMC simulations, here we present the results of full TAD simulations for the case of 2% compressive strain at a somewhat lower temperature (T = 200 K) and higher deposition rate (1 ML/sec).

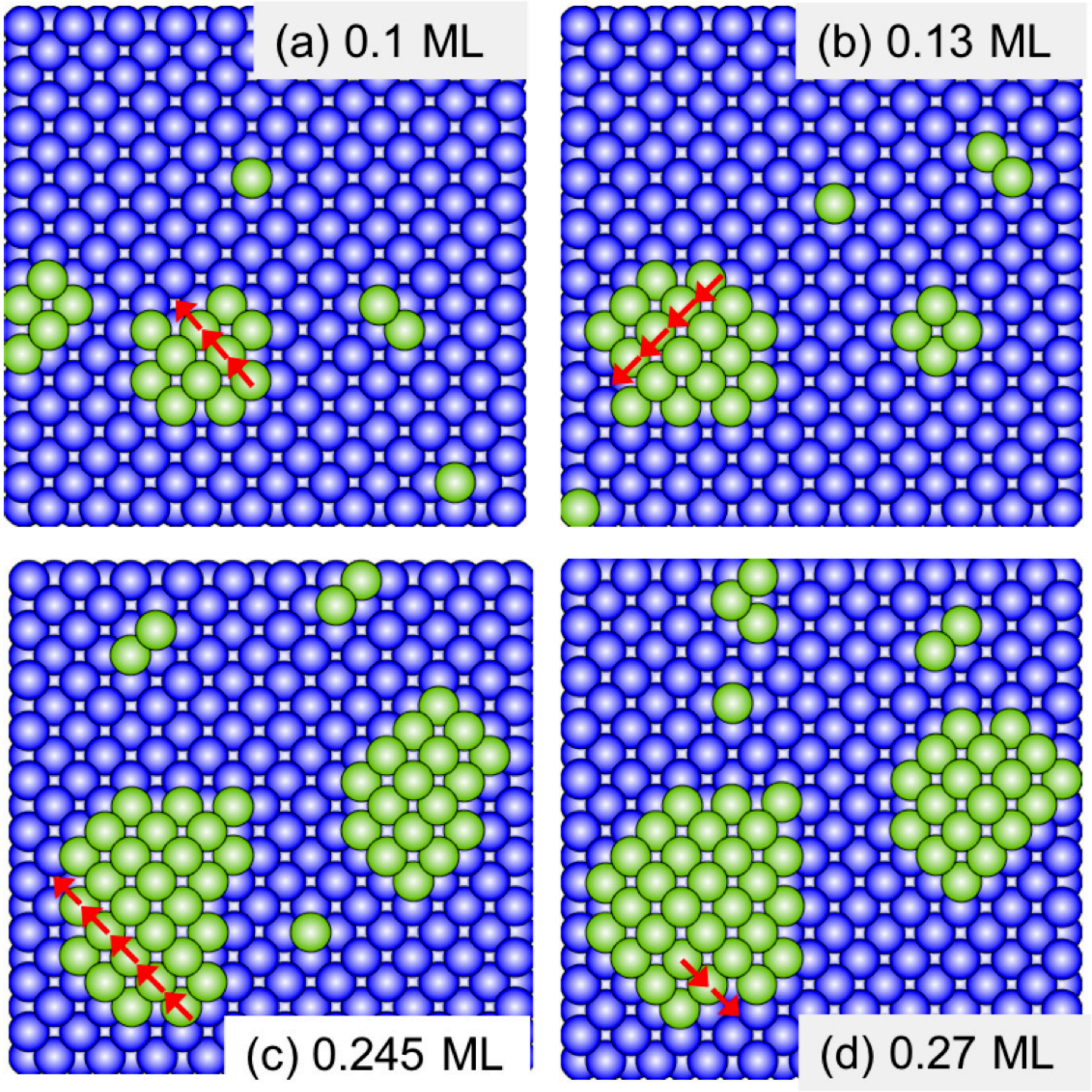

Figure 5-2: Evolution of system during growth of Cu on Cu(100) with 2% compressive strain. Also, shown (arrows) are typical multi-atom pop-out events (see text). The corresponding barriers with (without) strain are: (a) 0.32 (0.46) eV, (b) 0.43 (0.63) eV, (c) 0.46 (0.72) eV, and (d) 0.49 (0.79) eV.

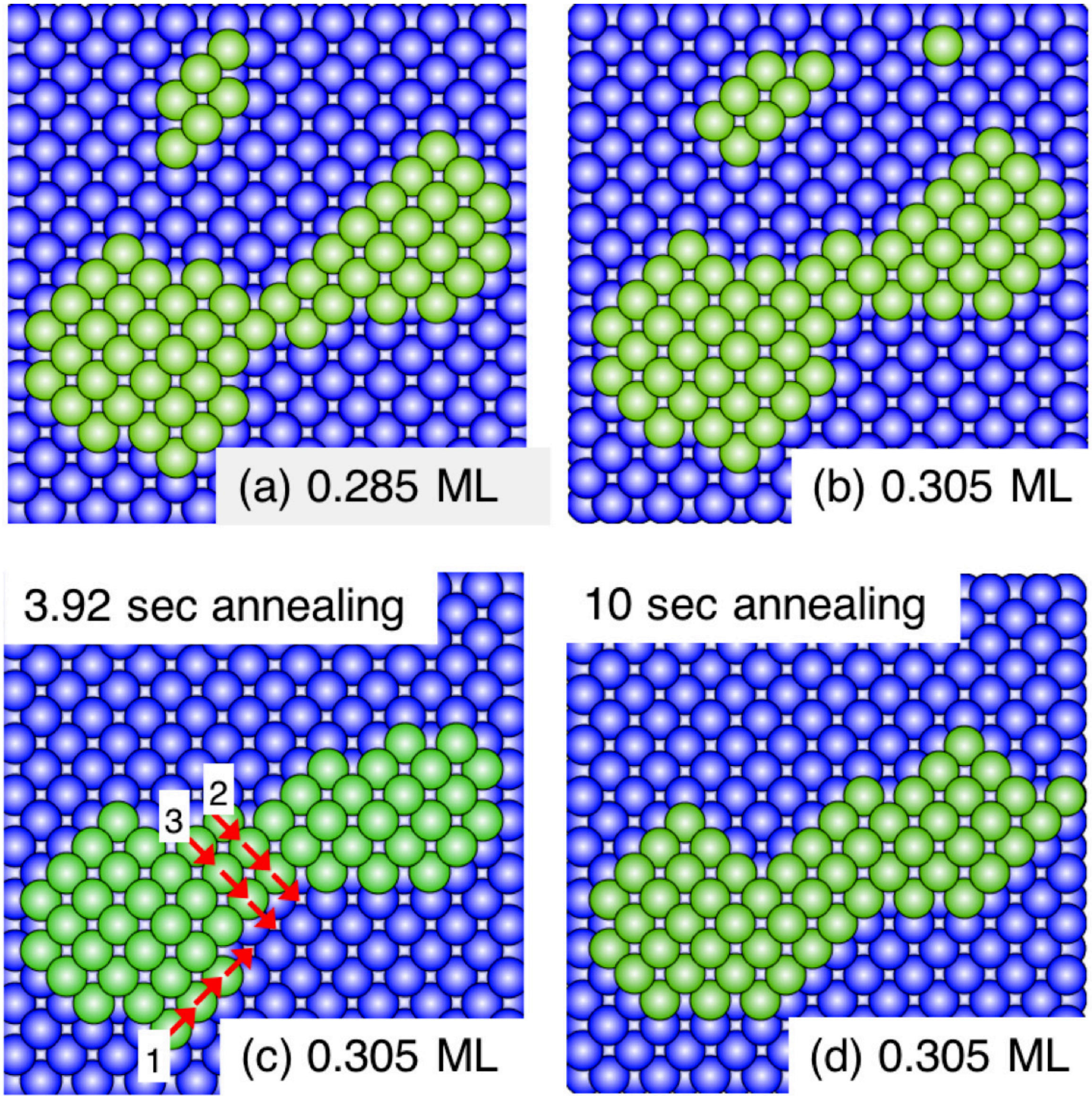

Figure 5-3: (a) and (b): Same as Fig. 5-2 but at higher coverage. (c) and (d): Evolution of elongated island during annealing. Barriers with (without) strain for events indicated in (c) are: (1) 0.62 (0.73) eV (2) 0.44 (0.63) eV and (3) 0.32 (0.51) eV

Fig. 5-2 shows the evolution of the island morphology in this case. As can be seen, once the coverage reaches 0.245 ML there are two relatively large islands in the system. As in our previous kinetic Monte Carlo simulations of Cu/Ni(100) growth [164], the two larger islands in Figs. 5-2(c) and (d) have a mixture of open ([100]) and closed ([110]) step-edges. As indicated by the arrows in Fig. 5-2, a variety of multi-atom in-plane pop-out events - whose barriers are significantly reduced due to strain - play an important role in determining the island morphology. The coalescence of the two small islands on the left-hand side of Fig. 5-2 (a) to form the larger island in Fig. 5-2(b) also involves a large number of similar 2-, 3-, and 4-atom moves.

At a coverage of 0.285 ML (see Fig. 5-3 (a)) the two large islands in Fig. 5-2(d) have coalesced to form one large elongated island with both open and closed step-edges, while at the end of deposition (0.305 ML, see Fig. 5-3(b)) four additional atoms have been deposited two of which have attached to the island. Interestingly, the resulting elongated structure is similar in shape to but approximately one-third the size of some of the elongated islands obtained in KMC simulations of Cu/Ni(100) growth at 250 K with a much lower deposition rate (0.0015 ML/s) after 0.5 ML have been deposited [164].

To study the morphological evolution of the large island over a longer time-scale (10 sec) we then annealed the system at 200 K with the heptamer removed to eliminate repetitive low-barrier edge-diffusion events. Fig. 5-3 (c) shows the island morphology after 3.92 sec of annealing at which point the total system energy has been reduced by 0.76 eV. A portion of this reduction (0.13 eV) was due to island re-arrangement events which occurred during the first 1.85 sec (just before the monomer attached to the island) while the system energy was further reduced by 0.51 eV after monomer attachment at a kink site. As a result of additional island re-arrangement events the energy was then further reduced by an additional 0.12 eV. As an illustration of the typical re-arrangement events, also shown in Fig. 5-3 (c) (arrows) are the next three events ((1) - (3)) which occur just after 3.92 sec of annealing along with the corresponding activation barriers with and without strain. As can be seen, all of these moves correspond to 3-atom events while the corresponding barriers are significantly reduced due to strain.

Fig. 5-3 (d) shows the final morphology after a full 10 sec of annealing. While the number of open step-edges has been further reduced, the island remains elongated as previously found in KMC simulations of the annealing of ramified Cu/Ni(100) islands at 250 K for 10^3 sec [164]. In addition, the total system energy has been reduced by an additional 0.32 eV. While the entire annealing process involved 230 activated events including monomer hopping, the overwhelming majority corresponded to collective events involving at least 3 atoms while the corresponding barriers ranged from 0.24 eV (monomer edge-diffusion) to 0.62 eV.

5.3.3 Submonolayer growth with 8% tensile strain

For comparison with our results for compressive strain, we have also carried out TAD simulations of Cu/Cu(100) submonolayer growth for the case of 8% tensile strain. As indicated in Fig. 5-1, the dominant mechanisms for adatom transport in this case are monomer and dimer diffusion via exchange with the substrate. As can be seen in Fig. 5-4 (corresponding to the end of growth with 0.215 ML deposited) due to the relatively low barriers for monomer and dimer diffusion only one island is formed. However, starting with a stable tetramer (atoms labeled ‘1’ in Fig. 5-4) the island growth becomes highly anisotropic. In particular, as indicated by the ‘atom numbers’ in Fig. 5-4 - which correspond approximately to the order of island growth - the island first forms an L-shape with both sides of the ‘L’ of width equal to two atoms (see atoms labeled ‘1 - 3’) and then grows along the ‘top’ arm, forming an extended two-atom wide rectangle, as well as at the ‘base’.

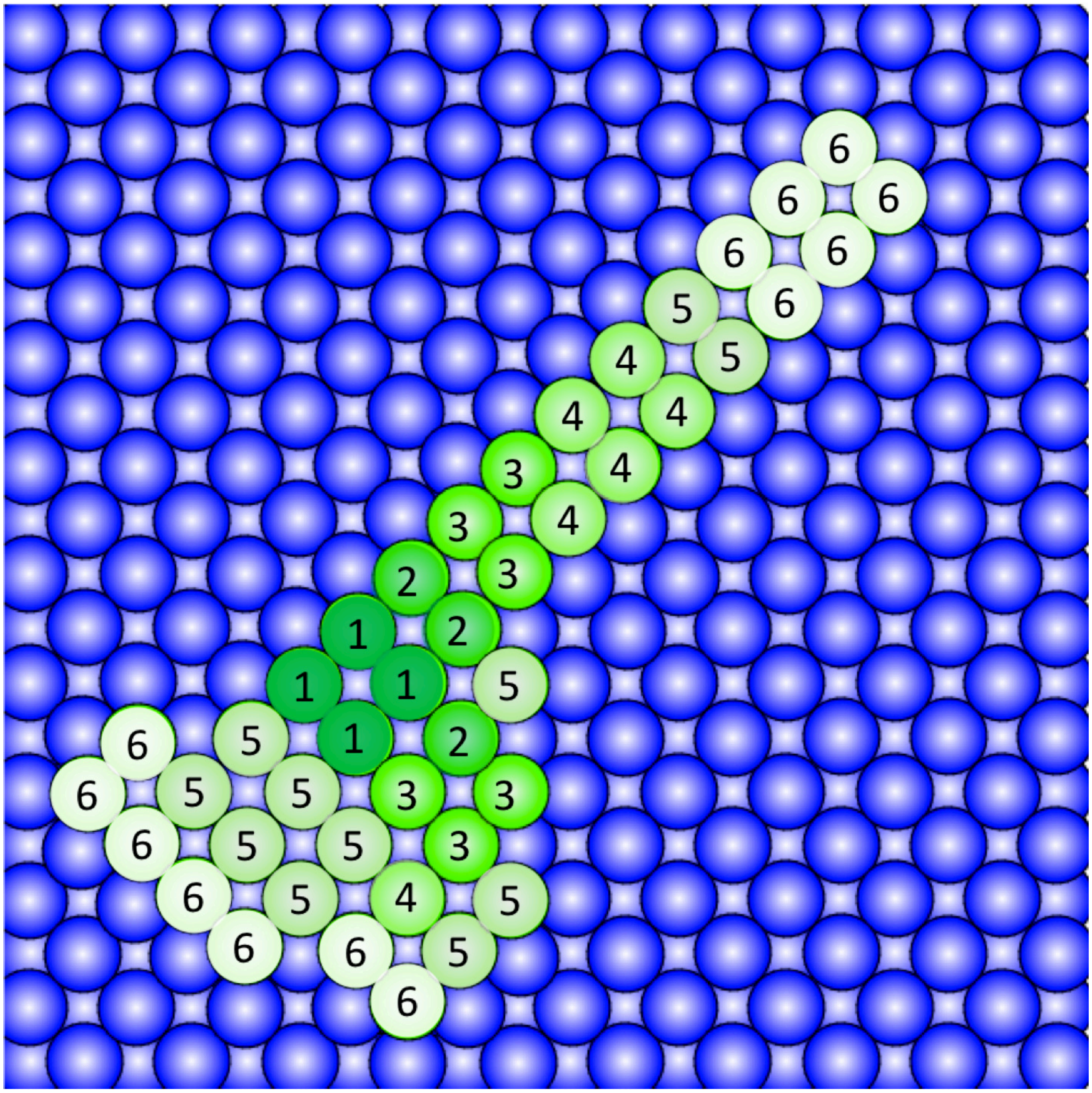

Figure 5-4: Growth of anisotropic island during deposition of Cu on Cu(100) with 8% tensile strain. Atom numbers correspond to order of island attachment (see text).

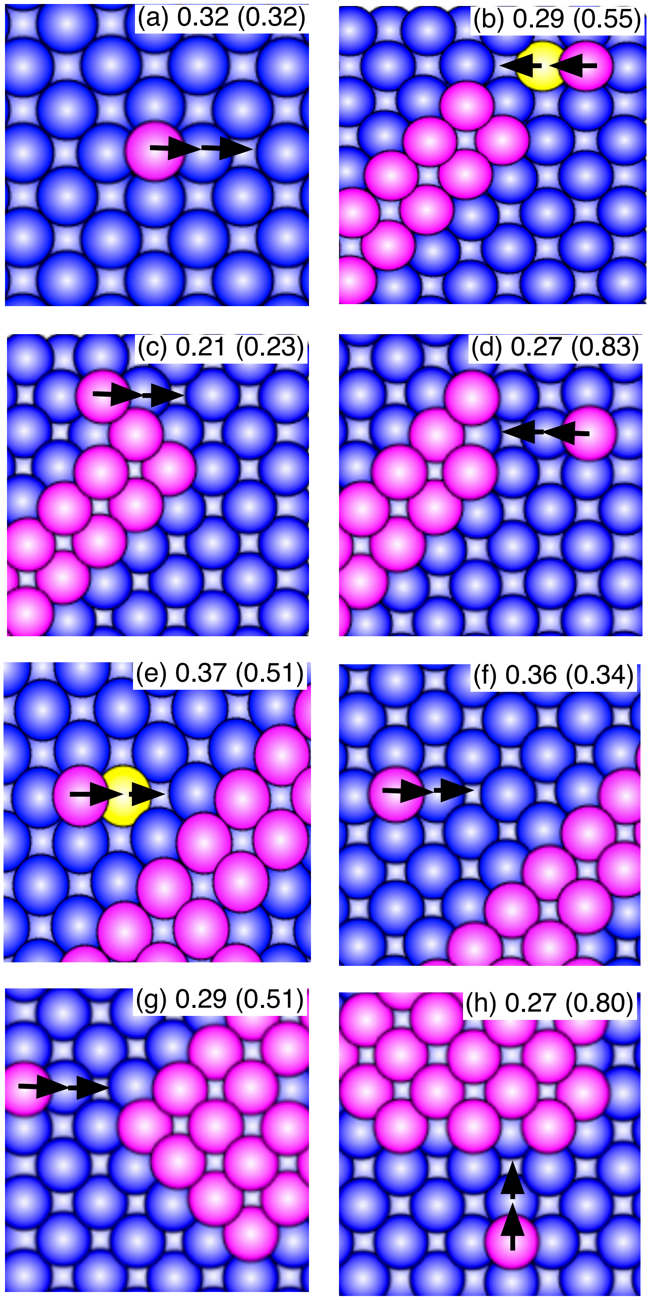

Figure 5-5: Key forward and reverse (in parentheses) barriers (in eV) involved in anisotropic island growth for case of 8% tensile strain: (a) monomer exchange on substrate (b) monomer attachment at tip (c) corner-rounding (d) attachment of 2nd monomer at tip (e) attachment to close-packed step-edge (f) approach to close-packed step-edge (g) corner-attachment (h) attachment to open step-edgel.

One possible explanation for the strongly anisotropic island growth is that the strain energy contribution to the total energy is significantly lower for anisotropic islands than for compact islands, thus compensating for the gain in perimeter energy. This is consistent with previous work on strained island growth in which a transition from square islands to anisotropic islands was found [151, 154, 156–159, 173] for sufficiently large island sizes. However, calculations which we have carried out for a variety of different island-sizes and aspect ratios indicate that at least for islands with up to 256 atoms, both the energy and free-energy at 200 K are always smaller for isotropic (square) islands than for anisotropic islands with the same number of atoms. Our calculation of the free energy takes into account the vibrational entropy as in Ref. [1]. While relatively small at 200 K, this contribution also tends to favor isotropic islands. Similarly, we find that the energy and free-energy at 200 K of an almost isotropic 43-atom island (corresponding to a compact 6 by 7 island with one edge atom) is significantly lower than the energy of the 43-atom island in Fig. 5-4. These results clearly indicate that the formation of an anisotropic island in our simulations is not due to energetics but is instead due to kinetics.

We now consider the kinetics of island growth. As can be seen in Fig. 5-5, while the barrier for monomer diffusion far away from the island (Fig. 5-5 (a)) is 0.32 eV, the barrier for attachment to the two-atom wide tip (Fig. 5-5 (b)) is only 0.29 eV, corresponding to a "negative" attachment barrier. Similarly, the barrier for a monomer to attach to the "side" corner of the two-atom wide tip (not shown) is also 0.29 eV, while the barrier for an exchange move from this corner to the front of the tip (Fig. 5-5 (c)) is only 0.21 eV. In addition, the barrier for a second monomer to attach at one of the tip corners (Fig. 5-5(d)) is only 0.27 eV.

In contrast, the barrier for attachment to a close-packed step-edge away from a corner (see Fig. 5-5 (e)) is significantly higher (0.37 eV). The activation barrier to approach one step away from a close-packed step-edge (0.36 eV, see Fig. 5-5 (f)) is also higher than the monomer diffusion barrier, while the reverse barrier (0.34 eV) is lower than the forward barrier. As a result, atoms are repelled from the long close-packed step-edges shown in Fig. 5-4 and attracted to the two-atom-wide tip. In fact, in our simulations only one atom attached to the upper close-packed step-edge of the island and that atom eventually migrated to the tip via two edge-diffusion moves with a barrier of 0.42 eV. These results clearly indicate that growth of the two-atom wide tip is strongly kinetically favored over sideways growth, thus explaining the island anisotropy.

Since Fig. 5-4 also indicates that significant island growth occurs in the lower half of the island, we have also calculated the corresponding attachment mechanisms and barriers. As can be seen in Fig. 5-5 (g), the barrier for attachment at the bottom corner (0.29 eV) is the same as for attachment at the tip (Fig. 5-5 (b)). In addition, the barrier for attachment at an open step-edge (0.27 eV, see Fig. 5-5 (h)) is the same as for the attachment of a second atom at the tip (see Fig. 5-5 (d)). As a result, in addition to growth at the tip, the island also grows at the base via attachment at open steps and corner sites, followed by multi-atom re-arrangement moves to minimize the number of open steps.

We now consider the mechanism for the decrease in the activation barrier for attachment via exchange at a corner compared to at a close-packed step-edge. Analysis of the local geometry indicates that in both cases there are three substrate atoms in front of the attaching atom (yellow atoms in Fig. 5-5 (b) and 5(e)) - one on each side of the final position and one in front. One of these substrate atoms has no island nearest-neighbors. However, in the case of attachment at a close-packed step-edge the other two substrate atoms each have two island nearest-neighbor bonds while in the case of attachment at a corner or tip, one of them has only one island nearest-neighbor bond. This implies that it is easier for nearby atoms to relax during the attachment process in the case of tip/corner attachment than during attachment at a close-packed step-edge, thus leading to a reduction in the tip/corner attachment barrier.

A similar argument also indicates that the energy reduction after tip/corner attachment should be larger than for attachment at a close-packed step-edge. In particular, we find that while attachment at a corner (Fig. 5-5 (g)) decreases the system energy by approximately 0.26 eV, attachment at a closed step-edge away from a corner only decreases the energy by 0.14 eV. Thus, the difference in the final state energy between close-packed step-edge attachment and tip attachment (0.12 eV) is consistent with but somewhat larger than the corresponding difference in the energy barriers (0.08 eV). In contrast, in the absence of strain - for which the dominant diffusion mechanism involves hopping - the activation barriers for attachment at a two-atom wide tip and a close-packed step-edge are the same (0.45 eV). Accordingly, square islands are both kinetically and energetically favored in this case.

5.4 Summary

Using an EAM potential, we have studied the strain dependence of the Cu monomer and dimer diffusion mechanisms and activation barriers on a biaxially strained Cu(100) substrate. As in previous calculations for Ag on strained Ag(100) [171] we find an approximately linear dependence of the activation barriers on strain. In particular, we found that while hopping is favored for compressive and/or small ($< 2\%$) tensile strain, for greater than 2% tensile strain the exchange mechanism is favored.

In order to compare with Cu/Ni(100) growth and also separate out chemical effects from strain effects as well as take into account all possible collective events which might not be included in KMC simulations, we have also carried out TAD simulations of submonolayer homoepitaxial Cu growth at 200 K for the case of 2% compressive strain. As in previous KMC simulations of Cu/Ni(100) growth [164], the competition between island growth and multi-atom "pop-out" events was found to lead to an island morphology with a mixture of open and closed steps. We also found that at a coverage of 0.305 ML, island coalescence leads to elongated islands as in Cu/Ni(100) growth. These results suggest that the primary cause of the ramified islands in Cu/Ni(100) growth is in fact strain rather than chemical effects.

We have also studied the annealing process for longer times (10 sec). Our simulations indicate that the primary relaxation processes involve a variety of multi-atom events involving 3 or more atoms whose barriers are significantly reduced due to strain and which tend to significantly reduce the number of open steps. These results clearly indicate that the island morphology during growth is due to a competition between island attachment (which leads to open step-edges) and multi-atom relaxation processes.

For comparison, we have also carried out TAD simulations of Cu/Cu(100) growth for the case of 8% tensile strain. In this case, due to the low barriers for monomer and dimer diffusion, the island density is relatively low and so only one large strongly anisotropic island was formed. Surprisingly, we found that despite the large strain the island anisotropy is not due to energetics but is instead due to anisotropic attachment barriers which favor the exchange-mediated attachment of monomers to corners over close-packed step-edges. We note that anisotropic islands have also been observed in the growth of Co on the reconstructed Pt(111) surface corresponding to 9.7% tensile strain [174]. However, in this case the anisotropy is a result of the Pt(111) reconstruction [175] which occurs in the absence of Co deposition and leads to highly anisotropic Co diffusion. In contrast, in our TAD simulations we have isotropic diffusion and there is no surface reconstruction. Thus, our results provide a new kinetic mechanism for the formation of anisotropic islands in the presence of isotropic diffusion and tensile strain.

Chapter 6

Energy, temperature, and deposition angle dependence of Cd and Te_2 deposited on CdTe

6.1 Introduction

Cadmium Telluride (CdTe) is an attractive absorber material for solar cell applications due to its optimal bandgap and high absorption coefficient [176, 177]. However, while CdTe thin-film solar cells are being successfully used in a variety of applications [178], the energy conversion efficiency is still significantly less than the Shockley-Queisser limit [179]. This difference may be due to a variety of effects such as deviations in stoichiometry as well as defects such as interstitials, vacancies, dislocations, and grain boundaries [180–182].

Recently, Yu and Kenny [183] have used molecular dynamics simulations based on a realistic bond-order potential [43, 184] to study the effects of the initial kinetic energy of small Cd_xTe_y clusters deposited normally on CdTe (100) and (111) surfaces at 300 K. In particular, depending on the deposition energy as well as the cluster type, surface orientation and termination type (e.g. Cd or Te), the probabilities of a variety of different outcomes (see cases 1-7 in Fig. 6-1) including reflection, dissociation, penetration, and atom replacement were determined. While a variety of results were obtained which may have an impact on the early stages of thin-film growth, these results were limited to the relatively high initial kinetic energies (e.g. 1 - 40 eV) used in sputter deposition, and were only carried out for the case of normal incidence with relatively low substrate temperature (T_{sub} = 300 K). In addition, the simulations were only carried out for the deposition of Cd atoms, Te atoms and a CdTe dimer, while the case of Te_2 cluster deposition, which is known to play an important role in vapor deposition and closed-space sublimation [185–188] was not considered.

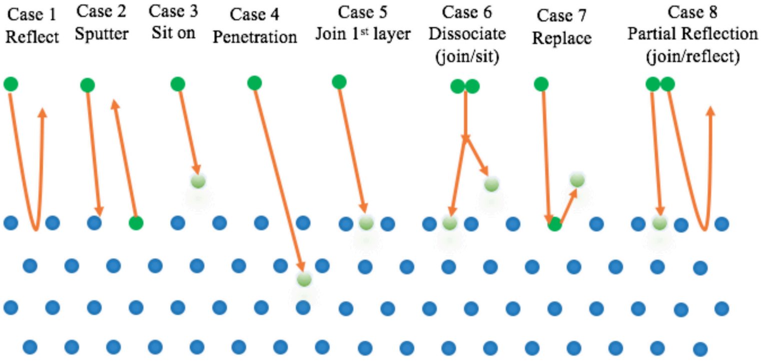

Figure 6-1: Illustration of 8 cases of the final states after impact.

Here we present the results of molecular dynamics (MD) simulations of Cd and Te_2 cluster deposition which were carried out in order to understand the dependence of the sticking probabilities and deposition modes on substrate temperature, deposition energy, and deposition angle. Our simulations are motivated in part by the fact that in both vapor deposition and close-spaced sublimation (CSS) the dominant depositing clusters are Cd atoms and Te_2 dimers (rather than Cd atoms, Te atoms and CdTe clusters as in Ref. [183]). Similarly, in both vapor deposition and CSS the deposition energy is typically much smaller than 1 eV (in the case of CSS the source temperature is typically close to 800 K) while the substrate temperature in vapor deposition may be low as in Ref. [183] or much higher. In addition, in both cases, depending on vapor pressure and target-substrate distance, it is also possible that deposition may occur at relatively large angles with respect to the substrate normal.

Our results may be summarized as follows. In general, we find that the deposition of Cd atoms and/or Te_2 clusters on the oppositely terminated surface leads to an attachment probability which is close to 1 and relatively independent of substrate temperature, kinetic energy, and deposition angle for both the (100) and (111) orientations. In contrast, the deposition of Cd atoms and/or Te_2 clusters on the same terminated surface leads to a significantly lower attachment probability which generally decreases with increasing substrate temperature, kinetic energy, and deposition angle. We also find a significantly higher attachment probability (compared to Cd atoms) for Te_2 dimers deposited on the (111) surface at both low and high temperature or kinetic energy, as well as for Te_2 dimers deposited on the (100) surface at low kinetic energy. However, in the case of deposition on the (100) surface at higher energy (1.0 eV), the excess Te sticking probability is significantly lower, and is even slightly negative for the case of normal deposition at 300 K. Since in most experiments the growth is polycrystalline but with (111) facets dominating, our results also suggest that both vapor deposition and sputter deposition at low substrate temperature ($T_{sub} = 300$ K) will tend to lead to Te-rich films. Although not discussed in detail below, we have also carried out simulations of Te atom deposition with 1 eV kinetic energy and substrate temperature $T_{sub} = 300$ K as a function of deposition angle. Consistent with the results of Ref. [183] for normal deposition - and in contrast to our results for Te_2 - we find that in this case the sticking probability is equal to 1 for all substrate terminations and deposition angles.

6.2 Molecular Dynamics Simulation Details

Our simulations were carried out using the Large-scale Atomic/Molecular Massively Parallel Simulator code [189, 190], using an analytical bond-order potential (BOP) [38–42] for CdTe which was parametrized [43, 184] by fitting to the properties of a variety of clusters, lattices, surfaces, and defects calculated using density-functional theory as well as testing crystalline growth simulations. We note that the analytical form of the BOP has been derived [38–42] from quantum mechanical theories which take into account both π and σ bonding.

Deposition on the Cd-terminated (100) and (111) surfaces as well as Te-terminated (100) and (111) surfaces was studied (see top view of all the surfaces in Fig. 6-2), while the zinc-blende structure of CdTe was assumed with lattice constant $a = 6.83 \mathring{A}$ [43]. In each case, simulations were carried out for both Cd and Te_2 cluster deposition. Starting from an initially bulk terminated surface, the system was annealed at the desired temperature for 20 ps before carrying out depositions for the case of the Te-terminated (100) surface this led to the 2×1 dimer reconstruction. In order to compare with previous work [183], we also carried out simulations of Te atom deposition for the case of normal incidence with $K_i = 1.0$ eV and $T_{sub} = 300$ K. Fig. 6-2 shows minimized configurations corresponding to each of the four CdTe terminations considered.

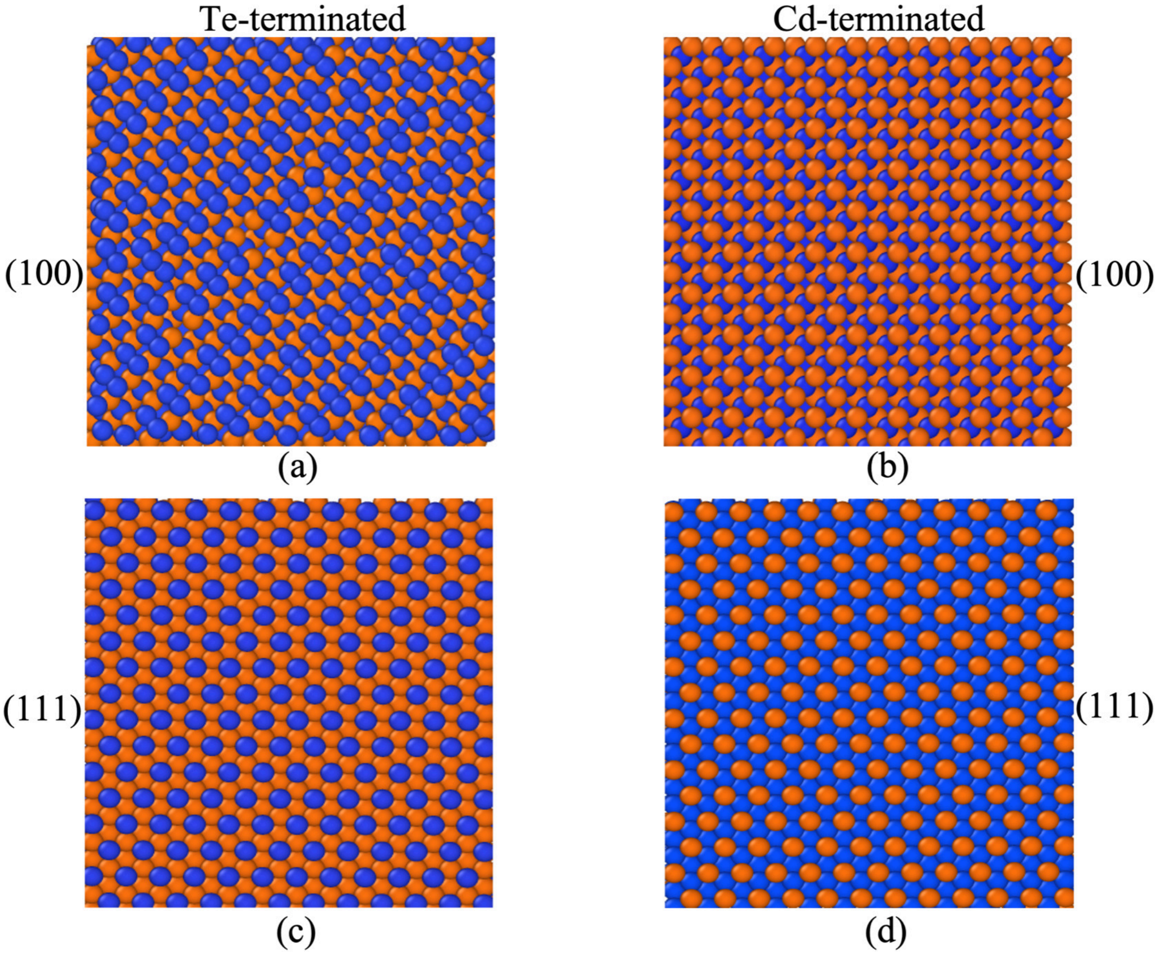

Figure 6-2: Top view of ((a) (100) and (c) (111)) Te-terminated and ((b) (100) and (d) (111)) Cd-terminated CdTe surfaces.

In order to determine the effects of deposition energy and substrate temperature on the sticking probability and mode, our simulations were carried out using two different cluster kinetic energies (K_i = 0.14 eV, and K_i = 1.0 eV) as well as for two different substrate temperatures (T_{sub} = 300 K and 800 K). Similarly, in order to study the dependence on deposition angle, simulations were carried out with six different deposition angles θ with respect to the surface normal, ranging from $\theta = 0^o$ (normal incidence) to 75^o (grazing incidence). In each case, the depositing cluster was initially placed at a height Δz above the highest atom on the surface layer which was equal to 1.5$\mathring{A}$ plus the maximum cut-off radius for the Zhou et al [43] potential (4.9 $\mathring{A}$), while the x and y positions were chosen randomly. MD simulations of the whole system were then carried out for 10 ps, after which the system was minimized and then analyzed to determine the sticking probability and deposition mode (see Fig. 6-1).

In order to determine the effects of deposition energy and substrate temperature on the sticking probability and mode, our simulations were carried out using two different cluster kinetic energies ($K_i = 0.14$ eV, and $K_i = 1.0$ eV) as well as for two different substrate temperatures ($\mathrm{T}_{sub} = 300$ K and 800 K). As shown in Fig. 6-3, in our simulations, the substrate corresponded to a total of 14 layers with 4 fixed layers, 4 layers thermostated using the Berendsen thermostat [35], and 6 non-thermostated layers at the surface (see the side view in Fig. 6-3). Both the heat bath coupling constant and the time-step were set to 1 fs. Periodic boundary conditions were assumed in the lateral (x and y) directions while growth was in the z-direction. For the (100) surface, the lateral dimensions were 10 a × 10 a, corresponding to 200 atoms in each layer. In contrast, for the (111) surface the dimensions were 6 a_1 (where $a_1 = \sqrt{8/3}a$) in the x-direction and 6 a_2 (where $a_2 = \sqrt{2}a$) in the y-direction, corresponding to 192 atoms in each layer.

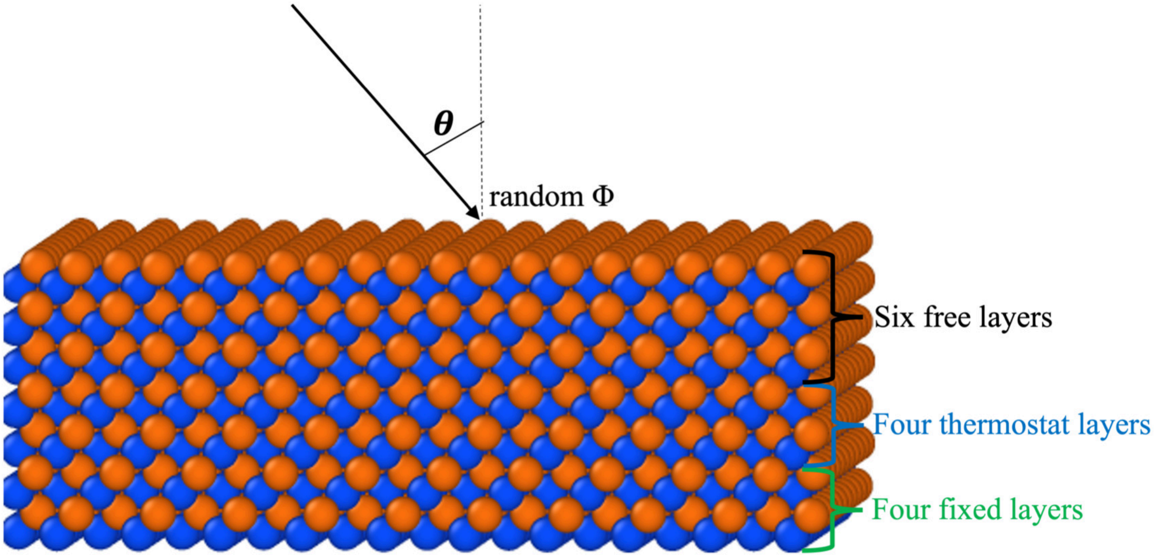

Figure 6-3: Side view of the CdTe substrate, where θ is the depostion angle to normal and ϕ is random azimuthal angle.

In order to obtain good statistics, averages were taken over 10,000 depositions for each cluster type and deposition angle with a given substrate termination, temperature, and initial kinetic energy, resulting in 32 different simulation runs for each of 6 different deposition angles. We note that the value $K_i = 0.14$ eV was motivated by the fact that at 800 K (which is approximately equal to the source temperature used in both vapor deposition and CSS) this corresponds to the average translational kinetic energy $2k_BT$ of depositing clusters. In the case of the Te_2 cluster, we have also included initial internal rotational and vibrational kinetic energies equal to $1/2\ k_BT$ per degree of freedom, with $T = 800$ K. In this case, in addition to randomly choosing the starting x and y positions, we have also randomly chosen the initial dimer axis orientation as well as the directions of the two rotational axes with respect to the Te_2 bond direction.

6.3 Results

6.3.1 (100) surface

Fig. 6-4 shows our results for the overall sticking probabilities for both Cd atoms and Te_2 clusters, deposited on the (100) Cd-terminated surface as a function of deposition angle θ for both kinetic energies (K_i = 0.14 eV and 1 eV) and substrate temperatures (T_{sub} = 300 K and 800 K). As can be seen, for the case of Te_2 deposition, the sticking probability is essentially 1 for all cases. In this case, the Te atoms sit on the top layer (case 3) which is consistent with the growth of the next Te layer. In contrast, the sticking probability for Cd atoms is significantly less than 1 even for normal deposition, and decreases with both increasing deposition angle and increasing substrate temperature. Interestingly, for low deposition angle ($\theta < 45^o$) the sticking probability for Cd atoms increases with increasing kinetic energy while the reverse is true for $\theta > 45^o$. In all cases the Cd atoms join the top layer (case 5). While the non-sticking case corresponds entirely to reflection at 300 K (case 1) which increases with deposition angle, at 800 K there is also a small amount of sputtering (1-7%), which decreases with increasing deposition angle.

The corresponding results for the (100) Te-terminated surface are shown in Fig. 6-5. As in Fig. 6-4, except for the case of both low deposition energy and substrate temperature (K_i = 0.14 eV, T_{sub} = 300 K), the deposition of Cd on the oppositely terminated (100) surface leads to a relatively high sticking probability ($P_{stick} = 0.85-0.95$) which increases slightly with deposition angle. While the dominant sticking mode corresponds to sitting on the top layer (case 3) there are also contributions from case 4 (penetration) and case 5 (join 1st layer). However, for both low kinetic energy and substrate temperature (open circles with dashed line) the sticking probability is significantly lower, especially at small angles - due primarily to the reduced probability of joining the 1st layer - although it still increases with increasing deposition angle.

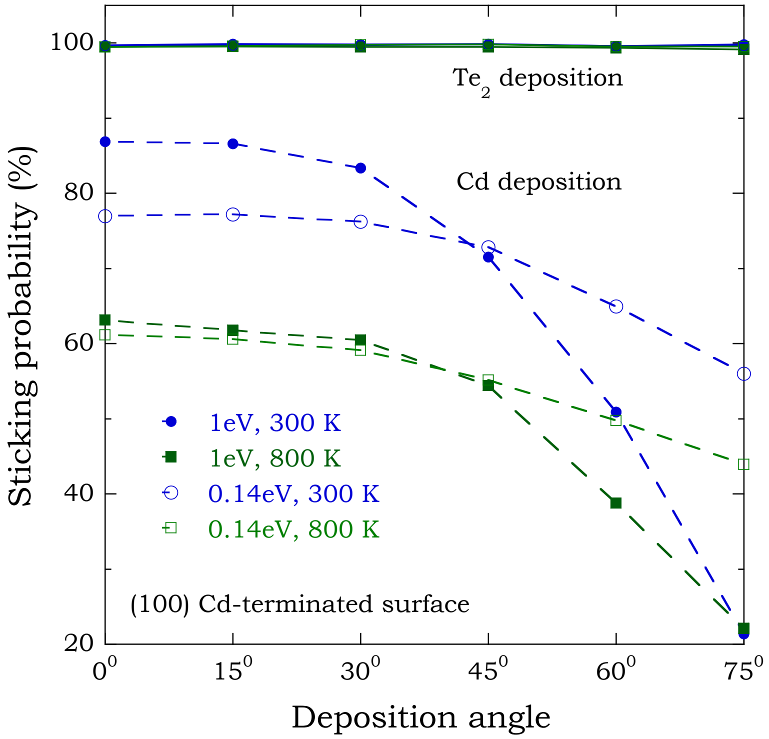

Figure 6-4: Sticking probabilities as function of deposition angle, substrate temperature, and initial kinetic energy for Cd atoms (dashed lines) and Te_2 clusters (solid lines) deposited on the (100) Cd-terminated surface.

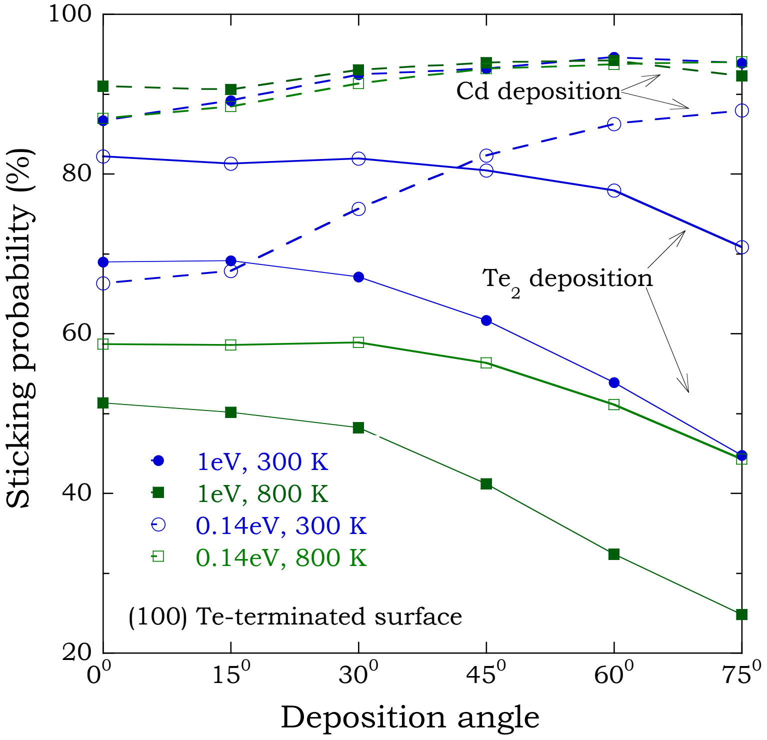

Figure 6-5: Same as 6-4 but for deposition on the (100) Te-terminated surface.

Also shown in Fig. 6-5 are our results for the deposition of Te_2 on the (100) Te-terminated surface. As for the case of Cd deposition on the Cd-terminated surface, in this case the sticking probability decreases with increasing deposition angle and temperature. In addition, it decreases for all angles with increasing kinetic energy. In this case, the sticking atoms primarily join the first layer (case 5) although the sticking probability also includes some case 3 (sit-on) and a very small amount of dissociation (case 6). As for the case of Cd deposited on the "same" (Cd-terminated) (100) surface, the dominant non-sticking mode corresponds to reflection while the probability of reflection (for fixed deposition angle) increases with increasing temperature and/or kinetic energy. In addition, the relatively large reflection probability for Te_2 clusters deposited normally with K_i = 1 eV and T_{sub} = 300 K is in contrast to the negligible reflection probability found [183] for single Te atoms deposited under the same conditions. There is also a small amount of partial reflection (case 8) in which one atom of the Te_2 dimer joins the first layer while the other is reflected. This is in contrast to the results of Ref. [183] for CdTe cluster deposition, in which partial reflection was never observed.

Using these results, we have calculated the overall excess Te sticking probability (averaged over both Cd- and Te-terminated (100) surfaces) as shown in Fig. 6-6, both for normal incidence as well as averaged over all angles (corresponding to a uniform flux). We note that in this case, the "excess Te sticking probability" also takes into account the small amount of Cd substrate atom sputtering which occurs for the case of Cd atom deposition on the (100) Cd-terminated surface at 800 K. As can be seen, the deviations from equal Cd and Te_2 sticking probability are generally larger for the case of normal incidence than the angle-average. In addition, for the case of low kinetic energy (0.14 eV) the excess Te sticking probability is particularly large, although it decreases with increasing substrate temperature. In contrast, for high kinetic energy (1 eV) the difference between Te_2 and Cd sticking probabilities is much smaller (and in some cases is even negative) due in part to the increased probability of reflection for Te_2 clusters from the Te-terminated (100) surface. This behavior is in contrast to the negligible reflection probability found [183] for single Te atoms deposited with 1 eV kinetic energy on the Te-terminated (100) surface.

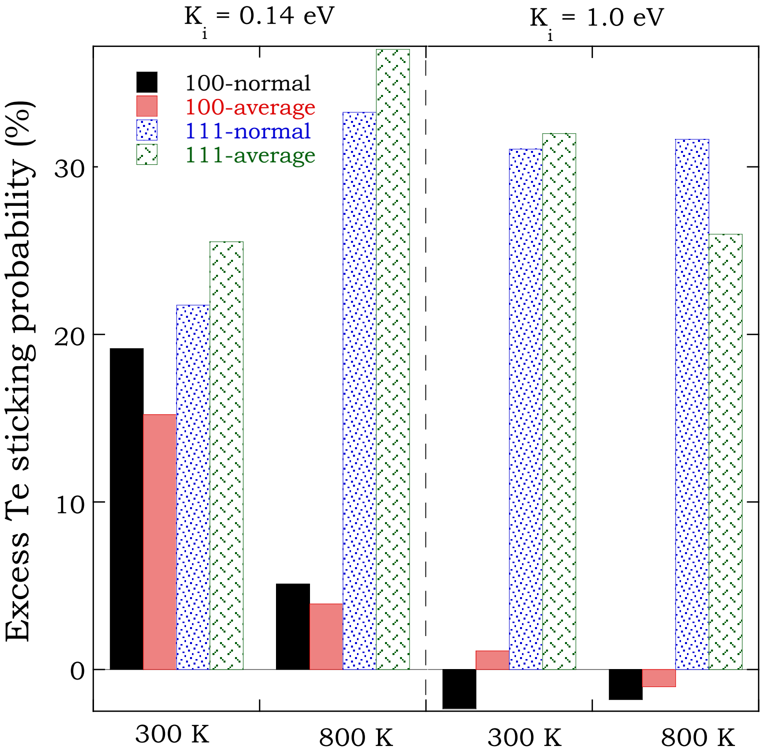

Figure 6-6: Excess Te on the substrate as function of deposition angle, substrate temperature, and initial kinetic energy for Cd and Te_2 clusters. In each case the first (black) and third (blue) bars correspond to normal deposition while the second (red) and fourth (green) bars represent the average over all deposition angles.

6.3.2 (111) surface

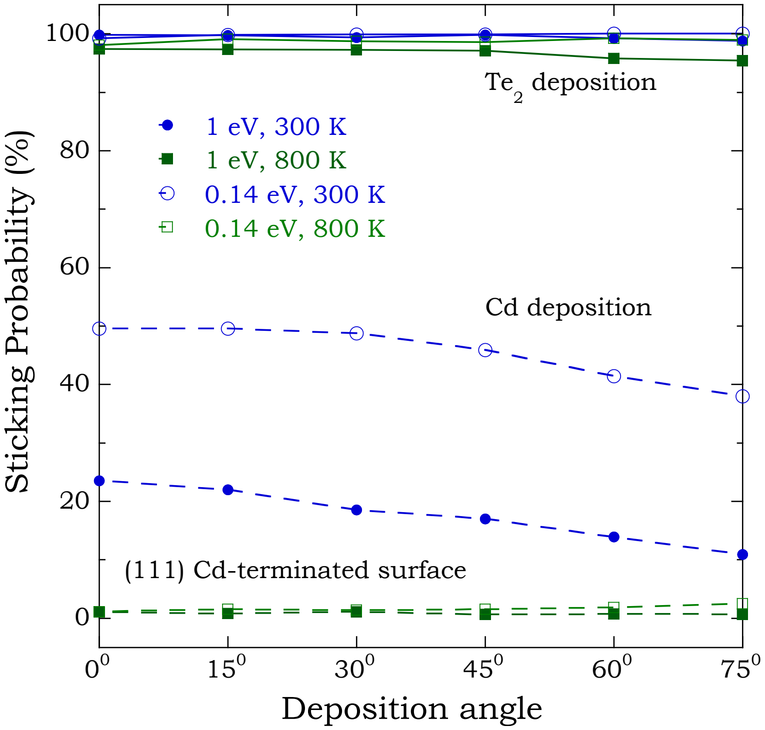

Figure 6-7: Sticking probabilities as function of deposition angle, substrate temperature, and initial kinetic energy for Cd atoms (dashed lines) and Te$_2$ clusters (solid lines) deposited on the (111) Cd-terminated surface.

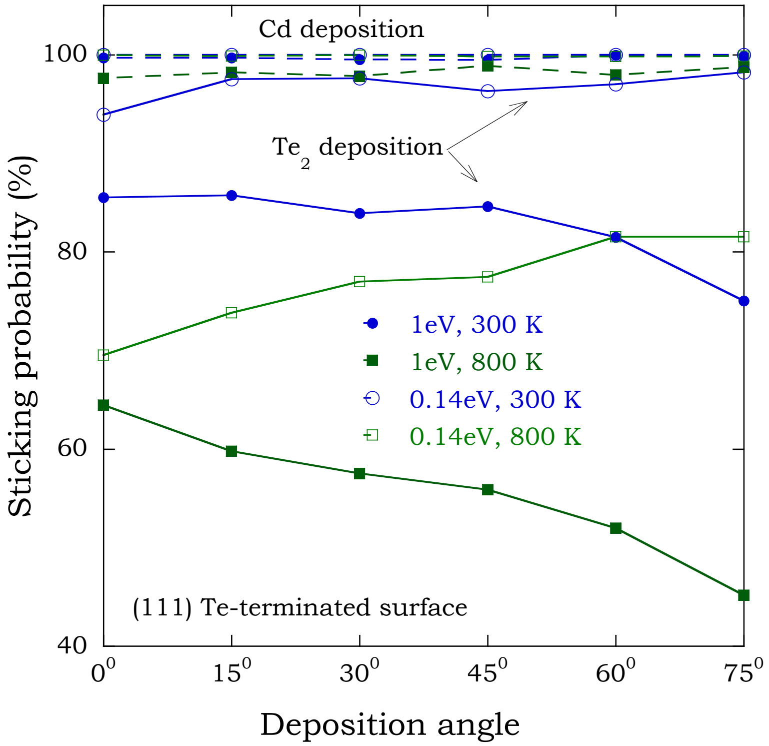

Figure 6-8: Same as Fig. 6-7 but for deposition on the (111) Te-terminated surface.

Fig. 6-7 shows our results for the (111) Cd-terminated surface. As for the (100) Cd-terminated surface, the sticking probability for Te$_2$ is close to 1 for all angles, kinetic energies and substrate temperatures, while the Te atoms sit on top (case 3). In contrast, the sticking probability for deposited Cd atoms at 300 K is significantly lower and decreases with increasing kinetic energy and deposition angle. In this case, the Cd atoms also sit on top (case 3). Surprisingly, the sticking probability for Cd atoms on the (111) Cd-terminated surface at 800 K is negligible at both low and high kinetic energies. At both 300 K and 800 K, reflection is the dominant non-sticking mode.

The corresponding results for the (111) Te-terminated surface are shown in Fig. 6-8. Just as for the case of Te$_2$ on the (100) Cd-terminated surface, the sticking probability for deposited Cd atoms is close to 1 for all angles, kinetic energies and substrate temperatures while the Cd atoms sit on top (case 3). For Te_2 deposition the attachment mode also corresponds to case 3. In this case, at low temperature and kinetic energy, the sticking probability (open circles with solid line) is also close to 1 for all angles and temperatures. However, for higher kinetic energy and/or temperature, the Te_2 sticking probability is significantly less. In addition, while for both substrate temperatures, the Te_2 sticking probability decreases with deposition angle for high kinetic energy ($K_i = 1.0$ eV) for low deposition energy ($K_i = 0.14$ eV) it increases with increasing deposition angle. Interestingly, the three cases of Cd deposited on the (100) Te-terminated surface at low kinetic energy and temperature, and Te_2 deposited on the (111) Te-terminated surface at low kinetic energy are the only cases in which the sticking probability increases significantly with increasing deposition angle.

The overall excess Te sticking probability (averaged over both Cd- and Te-terminated (111) surfaces) for this case is also shown in Fig. 6-6. As can be seen, in contrast to our results for (100) surfaces, for (111) surfaces there is a significant excess Te sticking probability for all deposition energies and substrate temperatures. In addition, the relatively close agreement between the angular average and that obtained for normal deposition is consistent with the relatively weak angular dependence.

6.4 Summary

Motivated by experiments on CdTe thin-film growth we have investigated the attachment probabilities and modes for Cd atoms and Te_2 clusters deposited on the (100) and (111) surfaces as a function of kinetic energy, deposition angle, substrate temperature, and substrate termination. Our results complement those previously obtained by Yu and Kenny [183] who focused on the case of normal deposition of Cd, Te, and CdTe clusters at low substrate temperature ($T_{sub} = 300$ K) and higher energies ($1 - 40$ eV).

In general, we find that - over the range of kinetic energies ($K_i = 0.14 - 1$ eV) and temperatures ($T = 300 - 800$ K) considered in our simulations - the deposition of Cd atoms and/or Te_2 clusters on the oppositely terminated surface leads to an attachment probability which is close to 1 and relatively independent of substrate temperature, kinetic energy, and deposition angle for both the (100) and (111) orientations. The one exception is the case of Cd deposition on the (100) Te-terminated surface with both low deposition energy and substrate temperature. In this case the attachment probability is only about 66% for normal deposition but increases to a value of approximately 88% at a deposition angle $\theta = 75^o$. While there is some penetration (case 4) and joining of the first layer (case 5), the dominant attachment mode in all cases corresponds to "sit-on" (case 3) thus leading to the growth of the next layer in the crystal.

In contrast, the deposition of Cd atoms and/or Te_2 clusters on the same terminated surface leads generally (for both the (100) and (111) orientations) to a significantly lower attachment probability which decreases with both increasing substrate temperature and deposition angle. In particular, the attachment probability for Cd deposition on the (111) Cd-terminated surface with substrate temperature 800 K is close to zero for both low and high kinetic energies and for all deposition angles. The one exception to these general results is the case of Te_2 deposition with low kinetic energy and substrate temperature on the (111) Te-terminated surface. In this case, while the attachment probability is still less than for Te_2 deposition on the (111) Cd-terminated surface, it is relatively close to 1 and increases with increasing deposition angle.

It is also interesting to consider the dependence of the deposition mode on atom/cluster type and surface termination. Interestingly, we find that for deposition on the (111) surface, the dominant deposition mode corresponds to case 3 (sit-on) regardless of cluster type, surface termination, deposition angle, substrate temperature and kinetic energy. This is also the case for opposite termination deposition on the (100) surface. In contrast, for same termination deposition on the (100) surface the dominant deposition mode corresponds to case 5 (join first layer) regardless of cluster type, surface termination, deposition angle, substrate temperature and kinetic energy. This difference may be explained by the more "open" nature of the (100) surface compared to the (111) surface which allows deposited atoms to join the first layer and form bonds with the "opposite" layer below. These results also imply that, as previously found in Ref. [183], (100) surfaces are more likely to create interstitials in the surface layer than (111) surfaces.

As shown in Fig. 6-6, for the case of deposition on (111) surfaces with both low and high deposition energy, as well as for (100) surfaces with low deposition energy, our results indicate a significant excess sticking probability for Te. This result is consistent with the simulation results of Ref. [183] obtained for the case of normal deposition of Cd, Te, and CdTe clusters and $T_{sub} = 300$ K with kinetic energies ranging from 1 eV to 40 eV. A detailed examination of our results suggests that this tendency towards an excess sticking probability of Te may be explained as follows. While Cd and Te_2 both have high sticking probabilities on oppositely terminated (100) and (111) surfaces, for the (111) surface as well as for the (100) surface with low kinetic energy, the Te_2 clusters have a higher sticking probability to the Te-terminated surface than the corresponding sticking probability of Cd atoms to Cd-terminated surfaces. This difference is consistent with the fact that the Te dimer bond is much stronger than the Cd dimer bond. In contrast, for the case of Te_2 deposition on the Te-terminated (100) surface, the probability of case 3 (sit on top layer) is reduced, while the probability of reflection also increases with increasing kinetic energy. As a result, the excess Te sticking probability tends to be much smaller and even negative in the case of normal or low angle ($\theta \leq 45^o$) deposition on the (100) surface at both high (1 eV) kinetic energy and low substrate temperature (300 K). The latter behavior contrasts with that found in Ref. [183] for the deposition of Cd atoms, Te atoms, and CdTe clusters for which the excess Te sticking probability (averaged over all deposition energies from 1 eV to 40 eV) remained positive in all cases.

While our results are restricted to the initial stages of deposition, they also suggest that for the case of low kinetic energy as well as low substrate temperature $T_{sub} = 300$ K (for which there is negligible sublimation) there will be a significant excess Te concentration in CdTe thin films grown on the (100) and (111) surfaces. This is in qualitative agreement with the experimental results of Ref. [191] for the vapor deposition of CdTe on glass substrates at 300 K. Since in most experiments the growth is polycrystalline but with (111) facets dominating [191–193], our results also suggest that both vapor deposition and sputter deposition will tend to lead to Te-rich films. However, at a substrate temperature of 800 K sublimation will play an important role [185, 186, 193]. Accordingly, in the future, it would be of interest to simulate the sublimation process in order to understand its effects during high temperature growth.

Chapter 7

Mechanisms of CdTe(100) sublimation

7.1 Introduction

Cadmium telluride (CdTe) is an attractive absorber material for solar cell applications due to its optimal bandgap and high absorption coefficient [177, 194]. As a result, CdTe thin-film solar cells have been shown to be quite efficient and commercially useful. One of the most important methods of CdTe thin-film deposition involves the process of closed-space sublimation [177]. However, while there have been a number of experimental [195–199] and theoretical [200–203] studies, the key sublimation mechanisms are still not well understood.

In particular, direct measurements of the CdTe(100) sublimation rate for T $>$ 360 °C [197, 199] indicate that the effective activation energy for sublimation E_a over this temperature range ($E_a \simeq 1.98\pm$ 0.18 eV) is significantly higher than the value ($E_a \simeq$ 1.55 eV) obtained at lower temperature [196, 199]. In contrast, the value of E_a obtained from reflection high-energy electron diffraction (RHEED) oscillation measurements [195, 198, 199] has been found to be approximately equal to 2.0 eV over the entire temperature range. While it has been proposed [199] that this may be due to a change in the sublimation mechanism from vacancy nucleation and growth to "step-flow" with decreasing temperature the detailed atomistic mechanisms have not been determined. In addition, while some calculations of the binding energies of Cd and/or Te atoms on the CdTe(100) surface have been carried out [200, 201, 203, 203], they were not able to fully explain the observed values of E_a or the overall sublimation rate. Accordingly, it is of interest to carry out further simulations to gain insight into the mechanisms for CdTe sublimation as well as to better understand the kinetics.

Here we present the results of binding energy calculations and accelerated-dynamics simulations we have carried out for the case of sublimation from the (100) CdTe surface. In particular, we have carried out accelerated molecular dynamics simulations of Cd atom and Te_2 dimer desorption for a variety of different configurations of the Cd-terminated and Te-terminated CdTe(100) surfaces. We have also calculated the corresponding binding energies as well as additional activation energies for step-edge detachment and diffusion.

This Chapter is organized as follows. In Sec. 7.2, we discuss our simulation methods. We then present our results in Sec. 7.3. Finally, in Sec. 7.4 we further analyze our results and compare with experiments.

7.2 Simulations

Our simulations were carried out using the LAMMPS molecular dynamics (MD) code [189, 190] along with an analytical bond-order potential [38] for CdTe which has been shown to provide good agreement [43] with experiments as well as density-functional theory calculations for small clusters, bulk lattices, defects, and surfaces. Using molecular dynamics, the activation barriers E_d and prefactors ν_d for desorption were determined for four different cases: (i) Te_2 desorption from the (2×1) fully Te-terminated (100) surface corresponding to a full monolayer or ML (ii) lone Te_2 dimer

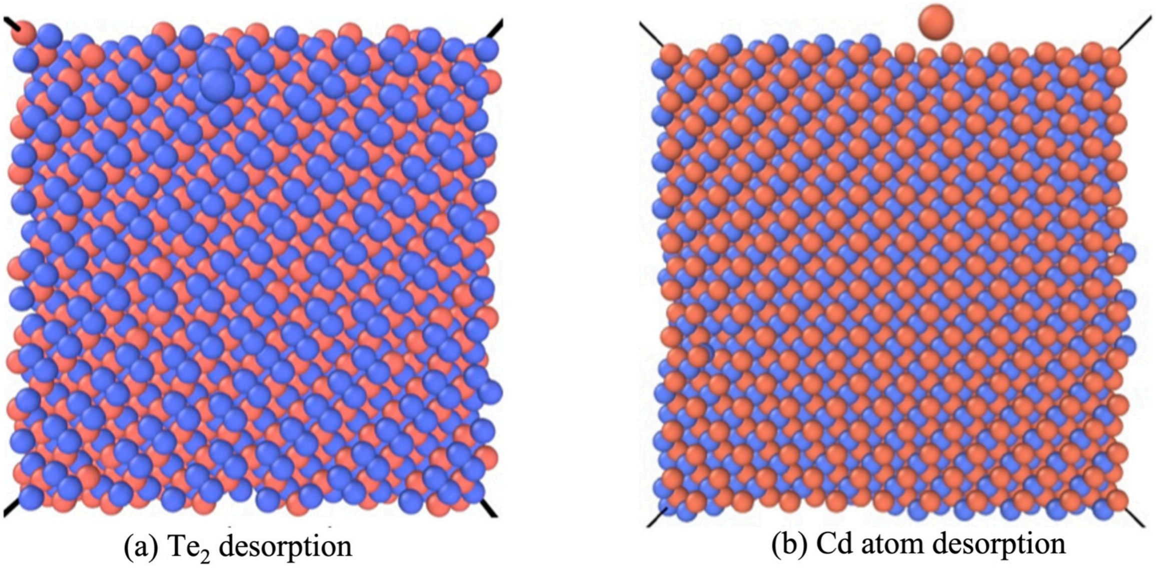

Figure 7-1: Snapshots of (a) Te$_2$ desorption from Te-terminated (100) surface after 1.5 ns of MD simulation at T = 1000 K and (b) Cd atom desorption from Cd-terminated (100) surface after 1.2 ns at T = 1100 K. Cd (Te) atoms are red (blue).

desorption on the Cd-terminated (100) surface (iii) Cd atom desorption from the fully Cd-terminated (100) surface and (iv) lone Cd atom desorption from the (2×1) fully Te-terminated (100) surface. The corresponding binding energies E_b were also calculated as well as the binding energies for four other cases: (i) a Te$_2$ dimer next to a dimer vacancy (ii) a lone Te$_2$ dimer on the fully Cd-terminated (100) surface (iii) a Cd atom next to a Cd vacancy and (iv) a lone Cd on the (2×1) Te-terminated (100) surface. Fig. 7-1 (a) and (b) show typical snapshots of a Te$_2$ dimer and a Cd atom desorbing from the fully Te-terminated and Cd-terminated surfaces.

To determine the desorption prefactors and activation energies for the first four cases, two different acceleration methods [204–206] were used. In the first temperature-accelerated (TA) method, the desorption rate $k(T)$ for a variety of temperatures T = T$_{MD}$/s (where s $\geq$ 1) was calculated from MD simulations carried out at temperature T_{MD} using the transition-state theory expression [205, 206]:

$$k(T) = \Big(\frac{4k_BT}{\pi m}\Big)^{1/2} \frac{1}{b} \Big\langle \frac{\sum_{t_i, h<z_i<h+b} W(\mathbf{R}, t_i)}{\sum_{t_i, z_i<h} W(\mathbf{R}, t_i)} \Big\rangle_{runs} \tag{7.1}$$

where the re-weighting function $W(\mathbf{R}, t_i)$ is given by,

$$W(\mathbf{R}, t_i) = exp\Big[\Big(\frac{1-s}{s}\Big)\frac{V(\mathbf{R}, t_i)}{k_BT}\Big]. \tag{7.2}$$

and $V(\mathbf{R}, t_i)$ is the total system potential energy at time t_i.

Here m and z_i are the mass and height of the desorbing species (Cd or Te_2 depending on the case) above the substrate at time t_i, h is the height of the bottom of a narrow window of width b above the substrate (where h is slightly larger than the potential cutoff distance R_c) and the angular brackets in Eq. 7.1 indicate that an average is taken over many (typically 300) uncorrelated MD runs, each starting with an equilibrated surface for which desorption has not yet occurred. In our simulations, data was taken every $\Delta t_i = 10$ fs, while the window width b ranged from 0.8 to 2.0 Å in steps of 0.2 Å. To maximize statistics, the calculated desorption rate was an average over all window widths. Depending on the case, T_{MD} ranged from 1000 K to 1100 K.

In the second repulsive potential (RP) method, a quadratic repulsive bias potential of the form $V_{rep}(r) = C\ (r - R_c)^2$ was added to the interaction between the top-layer atoms and the atoms in the layer below. In this case Eq. 7.1 above was still used to determine the desorption rate but the re-weighting function in Eq. 7.2 was replaced by the expression, $W(\mathbf{R}, t_i) = \mathrm{Exp}[-V_{rep}(r)/(k_BT)]$. In this second case, a series of separate repulsive-bias MD simulations with $s = 1$ (with the strength C of the repulsive potential appropriately adjusted) were carried out for each temperature T of interest. Depending on the temperature, species, substrate, and MD run, typical desorption times ranged from 0.5 ns to 9 ns.

In our simulations the substrate contained a total of 12 (100) planes consisting of

4 fixed (bottom) layers, 4 thermostatted Langevin (middle) layers and 4 free (NVE) top layers. The Langevin damping time was set to 1 ps while the MD time-step was 1 fs. In all cases, the lateral dimensions were 10 a (where a is the lattice constant) corresponding to 200 atoms in each layer. Periodic boundary conditions were assumed in the lateral (x and y) directions while sublimation occurred in the z- direction. In all cases the (per atom) desorption rate was calculated by dividing the total desorption rate by the total number of atoms in the desorbing layer.

7.3 Results

Fig. 7-2 shows Arrhenius plots of our results for the (per atom) desorption rate of Cd atoms from the Cd-saturated (100) surface (red symbols with solid lines) as well as the (per-atom) rate of Te_2 desorption from the (2 × 1) Te-saturated (100) surface (black symbols with solid lines). In each case, there is good agreement between the results obtained using the TA method (open symbols) and the RP method (filled symbols). In addition, the corresponding values of the activation barrier for Cd vacancy nucleation ($E_d = 2.15 \pm 0.01$ eV) are close to the values (2.0 ± 0.1 eV, see Fig. 7-3) obtained from mass-loss measurements of the total overall CdTe(100) desorption rate for $T > 360°C$ [196, 197, 199]. The corresponding binding energy E_b (see table 7.1) is also in good agreement with the activation energy while the value of E_b for a Cd atom next to a vacancy (2^{nd} Cd, see Table 7.1) is the same. In contrast, the activation barrier (2.6 ± 0.05 eV) for Te_2 dimer desorption from a full (2× 1) Te ML (corresponding to Te vacancy nucleation) is significantly larger. However, since the prefactor is approximately four orders of magnitude larger than that for Cd desorption (see Table 7.1), Cd desorption is the rate-limiting step for vacancy nucleation over this temperature range.

Also shown in Fig. 7-2 is an Arrhenius plot for the (per atom) desorption rate

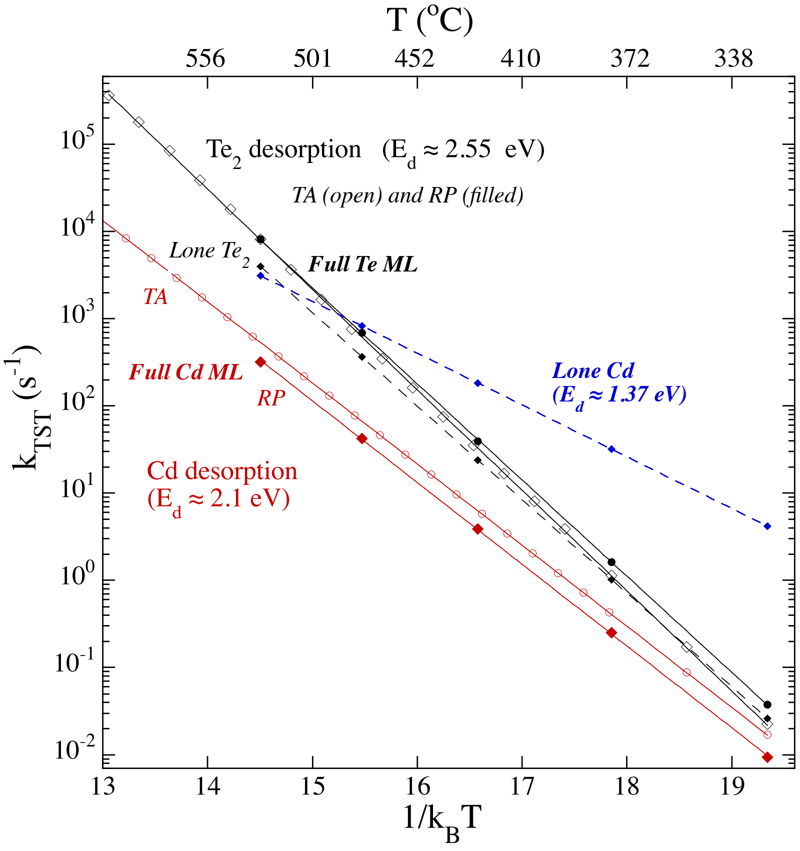

Figure 7-2: Per-atom desorption rates as function of $1/k_BT$ obtained using both RP method (solid symbols) and TA method (open symbols). Symbols with solid line fits correspond to desorption of first Te_2 (Cd) from corresponding Te (Cd) full ML while symbols with dashed line fits correspond to desorption of last Te_2 (Cd) in ML (see text). Corresponding prefactors and activation energies are given in Table 7.1.

of a lone Te_2 dimer on the (100) Cd-terminated surface. As shown in Table 7-2, the desorption barrier for a lone Te_2 adsorbed on the Cd-terminated (100) surface is close to that obtained for a Te_2 which is part of the fully Te-terminated (100) surface, although the prefactor is somewhat smaller. In addition, the corresponding binding energy is in good agreement with the estimated activation energy, while the binding energy for a Te_2 next to a dimer vacancy is also approximately the same as the other two cases. These results indicate that the (per atom) rate of Te_2 desorption is relatively independent of the Te coverage. However, the binding energy for a lone

Te adatom on the (100) Cd-terminated surface ($E_b \simeq 2.16$ eV, see Table 7.1) is somewhat lower but still significantly higher than the effective active energy found experimentally (e.g. 1.4 - 1.56 eV) at low temperature.

Table 7.1: Desorption barriers E_d (eV), prefactors ν_d (s^{-1}), and binding energies E_b (eV) for Cd and/or Te desorption from the (100) CdTe surface.

Species	Method	$\nu_d(s^{-1})$	$E_d(eV)$	E_b (eV)
1^{st} Te_2 (full Te ML)	TA	4.0×10^{20}	2.65	2.60
	RP	7.9×10^{19}	2.54	2.60
2^{nd} Te_2 (full Te ML)				2.50
lone Te_2 (full Cd ML)	RP	1.4×10^{19}	2.47	2.48
lone Te (full Cd ML)				2.16
1^{st} Cd (full Cd ML)	TA	1.7×10^{16}	2.14	2.16
	RP	1.3×10^{16}	2.16	2.16
2^{nd} Cd (full Cd ML)				2.16
lone Cd (full Te ML)	RP	1.3×10^{12}	1.37	1.33

In contrast, both the desorption barrier and prefactor for a lone Cd atom on the (2× 1) Te-saturated (100) surface ($E_d \simeq 1.37$ eV, $\nu_d = 1.3 \times 10^{12}$ s^{-1}) are significantly lower than for Cd vacancy formation. One possible explanation for this difference is the (2 × 1) Te reconstruction. In particular, for the case of large Cd coverage the Te-layer underneath is not reconstructed and so bonds more strongly to the Cd atoms above. In contrast, for the case of a lone Cd on Te, the Te_2 dimer reconstruction leads to much weaker binding with the Cd atom above. Interestingly, the activation energy in this case is close to the experimentally obtained values (1.4 - 1.56 eV, see Fig. 7-3) [196, 199] for CdTe(100) sublimation at low temperatures (T = 300 - 360 ^oC). Thus, while our simulation results indicate that CdTe(100) sublimation via vacancy nucleation and growth is limited by the large activation barriers (2.0 eV) for Cd desorption, if there exists a low barrier pathway for Cd atoms to detach from Cd clusters and/or descending Cd step-edges then the desorption of lone Cd atoms may also play an important role.

In order to investigate this possibility we have carried out additional MD simulations at T = 1000 K of a system consisting of an upper Cd terrace (with step-edges oriented along the [100] direction [207]) with a full Te-terminated terrace on each side. Our results indicate that the barriers for detachment and subsequent diffusion away from the step-edge are relatively low, ranging from 0.29 eV to 0.51 eV. Since both the prefactor and activation barrier for lone Cd desorption are significantly lower than for Cd vacancy nucleation and growth, these results indicate that at low temperatures the desorption of lone Cd atoms may play an important role. .

7.4 Summary

Using molecular dynamics simulations we have calculated the (per atom) desorption rates of both lone Cd atoms on the (2×1) Te-terminated (100) surface as well as the corresponding rates for Cd atoms which are part of a larger island or monolayer. Similar calculations were carried out for the desorption of lone Te_2 dimers from the Cd-terminated (100) surface. Our results indicate that while the barrier for Te_2 dimer desorption is relatively independent of coverage, the barrier for Cd desorption depends on the local environment. In particular, we found that, due to the Te (2×1) reconstruction, the barrier for desorption of a lone Cd atom is significantly lower than for Cd vacancy nucleation and/or growth.

Our results also indicate that, while the barrier for Te_2 desorption is significantly higher than for Cd vacancy nucleation and growth, the prefactor for Te_2 desorption is also significantly higher. As a result, for sufficiently high temperatures that vacancy nucleation and growth dominates over lower barrier processes, Cd adatom desorption is the rate-limiting step, as shown in Fig. 7-2. Accordingly, our calculated values for the corresponding Cd desorption barriers ($E_d \simeq 2.16$) are in good agreement with the experimentally obtained effective activation energies ($E_a = 1.9 - 2.0$ eV) [196, 197, 199] for T $\geq$ 360 ^{o}C. In contrast, for T $<$ 360 ^{o}C experiments [196, 199] indicate that lower barrier processes, such as the desorption of lone Cd atoms, will dominate.

In addition to comparing with the experimentally observed activation energies, we may also use our calculated desorption rates to try to predict the overall CdTe(100) sublimation rate as a function of temperature. We first consider the dominant sublimation mechanisms at high temperature corresponding to vacancy nucleation and growth as indicated by the agreement between RHEED [195, 199] and mass-measurement [196, 197, 199] experiments over this temperature range. Averaging the temperature-dependent TA and RP results for the (per atom) desorption rate of the first Te_2 shown in Table 7.1, and then averaging these values with the corresponding lone Te_2 desorption rates we obtain an estimated temperature-dependent rate of Te desorption given by R_{Te}. Similarly, averaging the TA and RP results shown in Table 7.1 for the (per atom) Cd desorption rate yields an estimated overall rate of Cd desorption via vacancy nucleation and growth given by R_{Cd}.

Assuming that the total average rate of Cd desorption is equal to the total average rate of Te desorption, and also assuming an overall average Te coverage θ_{Te} and Cd coverage $\theta_{Cd} = 1 - \theta_{Te}$, we obtain,

$$\theta_{Te} R_{Te} = (1 - \theta_{Te}) R_{Cd} \tag{7.3}$$

Solving for θ_{Te} we obtain,

$$\theta_{Te} = \frac{R_{Cd}}{R_{Te} + R_{Cd}} \tag{7.4}$$

Substituting this result in Eq. 7.3 along with the temperature-dependent values of R_{Te} and R_{Cd} and multiplying by the CdTe(100) double-layer spacing (3.24 Å) leads to the predicted sublimation rates shown by the dashed line in Fig. 7-3. As can be seen, for $T \geq 360°C$ there is good quantitative agreement between the prediction of Eq. Eq. 7.3 and the experimental results of Ref. [196]. In addition, the predicted effective activation energy over this temperature range (2.2 eV) is in reasonable agreement with the corresponding experimental values ($E_a \simeq 1.9 - 2.0$ eV) [196, 197, 199]. The good quantitative agreement with direct measurements [196, 197] is also consistent with the fact that RHEED measurements [195, 198, 199] - which measure the rate of sublimation via vacancy nucleation and growth - lead to approximately the same value of E_a. However, at lower temperatures ($T < 360°C$) the activation energies determined from direct measurements (see Fig. 7-3 and Refs. [196, 197, 199]) are significantly lower, which indicates that additional lower-barrier mechanisms become important.

As already discussed, one possible low-barrier mechanism is the desorption of lone Cd atoms. Unfortunately, since the lone Cd atom density depends on a variety of unknown factors such as the step density as well as step detachment and re-attachment rates, it is difficult to precisely calculate this quantity. Here we assume for simplicity that at all temperatures there is a fixed but small average density x of lone Cd atoms on Te terraces. Making this assumption Eq. 7.3then becomes,

$$(\theta_{Te} - x)R_{Te} = xR_{L,Cd} + (1 - \theta_{Te})R_{Cd} \tag{7.5}$$

where $R_{L,Cd}$ is the temperature-dependent rate of per-atom lone Cd desorption (see Table 7.1). Solving for θ_{Te} we obtain,

$$\theta_{Te} = \frac{R_{Cd} + x(R_{L,Cd} + R_{Te})}{R_{Te} + R_{Cd}} \tag{7.6}$$

Substituting this result in Eq. 7.5 with $x = 0.02$ While we have tried several different possible values for x in Eq. 7.6, the effective value $x = 0.02$ was found to give temperature-dependent activation energies in relatively good agreement with

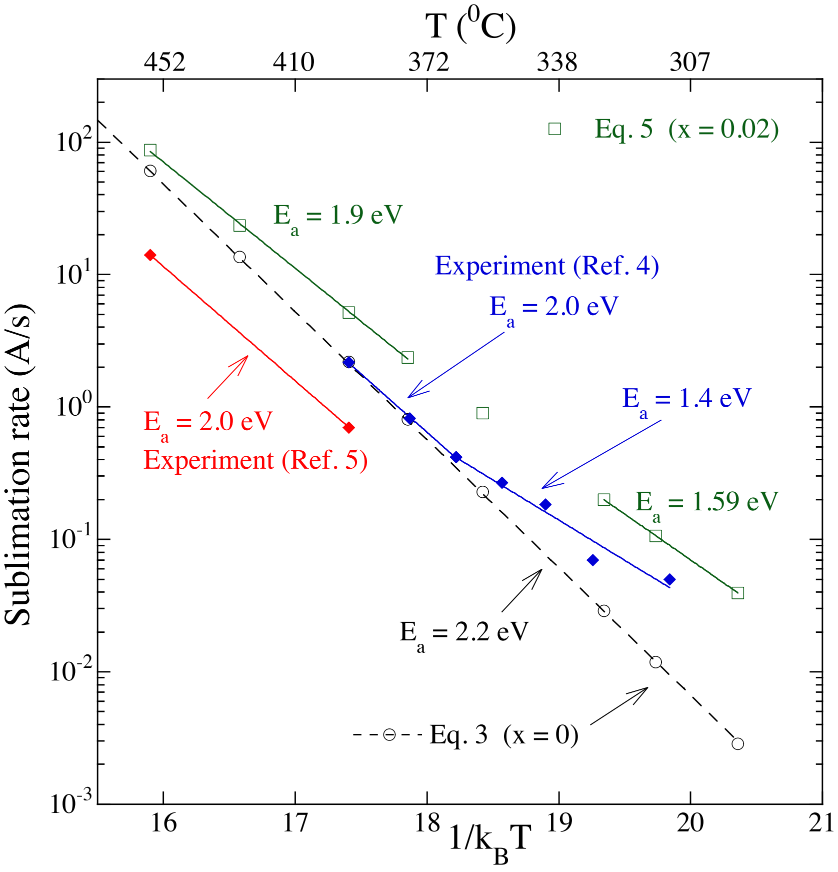

Figure 7-3: Comparison of calculated CdTe(100) sublimation rates and effective activation energies (open symbols) with experiments (filled symbols). See text for details.

experiments. In contrast, while lower values for x gave reasonable agreement with experiment for $T > 360^oC$, they also led to effective values of the activation energy for $T < 360^oC$ which were significantly larger. and again multiplying by the double-layer spacing leads to the results indicated by the open squares in Fig. 7-3. As can be seen, the predicted sublimation rates are now somewhat higher than the experiment at both low and high temperatures. However, there is now a clear transition in the effective activation energy from a value (1.59 eV) close to that obtained experimentally for $T < 360°C$ to a higher temperature value (1.9 eV) which is also in good agreement with the experiment. In the future, it would be of interest to carry out additional simulations to further elucidate the mechanisms for low-temperature sublimation.

Chapter 8

Summary and possible future work

In this dissertation, a variety of computational and analytical techniques have been used to study the properties of bulk alloys and thin films. In particular, in Chapter 3, the stability and mechanical properties of 3d transitional metal carbides in zincblende, rocksalt, and cesium chloride crystal structures are studied using DFT. In Chapter 4 and Chapter 5, the results of temperature-accelerated dynamics (TAD) simulations of the submonolayer growth of Cu on a biaxially strained Cu(100) substrate were presented. Finally, in Chapter 7, the process of CdTe(100) sublimation was studied using two different acceleration methods based on transition-state theory and umbrella sampling.

In Chapter 3 we carried out first-principles calculations based on density functional theory to tabulate the electronic structures, formation energies, and phonon dispersion curves of 3d transition metal carbides in the zincblende, rocksalt, and cesium chloride structures. Analysis of our results led to a theoretical framework that describes how valence electron concentration and bonding configuration control the stability of these compounds. In particular, we found that many early transition metal carbides are stable in the rocksalt and zincblende structures, due to the existence of filled bonding states. In contrast, the cesium chloride structure was generally found to lead to instability for the metal carbides across the 3d transition metals. For compounds that are predicted to be stable, mechanical properties were investigated through the calculation of elastic tensors, and a variety of observable properties such as Vicker's hardness and ductility were derived. We also found that robust mechanical performance was correlated with the complete filling of bonding orbitals as illustrated for rocksalt TiC and VC, which were found to have very high calculated hardnesses of 25.66 and 22.63 GPa respectively. However, we also found that enhanced ductility and toughness can be achieved by lowering the occupation of the antibonding states. One example of this is CrC, which we found to have a relatively low Pugh's ratio of 0.51.

Our results in Chapter 3 also indicate some possible directions for future work. For example, an optimal tradeoff may be realized through ion substitution – e.g., between TiC and CrC. By forming solid solutions with controllable compositions, the mechanical properties may be fine-tuned by varying Ti-Cr content. Although some past works suggest that high temperatures are necessary to form such solutions, alternative techniques such as high-energy ball milling or doping (e.g., high-entropy alloys) may be considered in the future.

In Chapters 4 - 7 we then presented the results of accelerated dynamics simulations of submonolayer metal thin-film growth as well as of MD and accelerated dynamics simulations of CdTe deposition and sublimation. In particular, in Chapter 4 the results of temperature-accelerated dynamics (TAD) simulations of the submonolayer growth of Cu islands on a biaxially strained Cu substrate at 200 K were presented. For the case of 4% compressive strain we found that stacking fault (SF) formation occurs with a morphology very similar to the structures found experimentally in Cu/Ni(100) growth. We also found that, in addition to the presence of compressive strain, islands play a key role in SF formation by lowering the barrier for vacancy formation in the substrate. In particular, we found that once two substrate vacancies are formed and diffuse to form the appropriate configuration, a SF is formed in both the substrate and island. While the activation barrier for SF formation is very high, we found that due to the presence of a large number of low-frequency vibrational modes, the saddle-point entropy is also very large. As a result, the corresponding Vineyard prefactor was found to be more than 14 orders of magnitude larger than is typical of atomic processes in fcc metals. Similarly, our analysis of the vibrational entropy of the SF state demonstrated that the free energy of the SF state is significantly lower than that of the initial state, and also explained why the Vineyard prefactor for the reverse process is much smaller. As a result, our results confirm that SF formation is both kinetically and thermodynamically favored for T > 100 K. In the future it would be of interest to carry out TAD simulations of multilayer Cu/Ni(100) growth to see if the mechanisms discovered in strained Cu/Cu(100) simulations can also explain the stacking fault "stripes" observed in experiments.

In Chapter 5, we then studied the general dependence of the diffusion mechanisms and corresponding activation barriers for Cu monomer and dimer diffusion on a biaxially strained Cu(100) substrate with both compressive and tensile strain. As in previous work for Ag/Ag(100) an approximately linear dependence was obtained. However, while hopping was found to be favored for compressive and/or small (<2%) tensile strain, the exchange mechanism was favored for greater than 2% tensile strain. We then carried out TAD simulations of submonolayer growth at T = 200 K with a deposition rate of 1 ML/s for the case of 2% compressive and 8% tensile strain. For the case of 2% compressive strain we found that, as in previous kinetic Monte Carlo simulations of Cu/Ni(100) growth [164], the competition between island growth and relaxation due to multi-atom "pop-out" events leads to an island morphology with a mixture of open and closed steps. In contrast, for the case of 8% tensile strain, a new general kinetic mechanism for the formation of anisotropic islands in the presence of isotropic diffusion was found. In particular, due to the preference for the exchange-mediated attachment of monomers to corners over close-packed step-edges, monomer attachment at the island tip was found to be strongly favored, thus explaining the observed island anisotropy. While it is known that for sufficiently large strain, the competition between surface tension and strain energy may lead to anisotropic islands for sufficiently large island-sizes, our energetics calculations indicated that the large island anisotropy in this case was not due to energetics but rather to kinetic effects. In the future, it may be of interest to carry out additional TAD simulations of submonolayer growth on (111) surfaces with tensile strain to see if a similar mechanism occurs in this case.

In Chapter 6 we then carried out molecular dynamics simulations in order to determine the dependence of the sticking probability and sticking mode of Cd atoms and Te_2 dimers on the deposition energy, angle, and substrate temperature for the case of deposition on the fully Te- and Cd-terminated (100) and (111) surfaces. In general, we found that the deposition of Cd atoms and/or Te_2 dimers on the oppositely terminated surface leads to an attachment probability which is close to 1 and relatively independent of deposition conditions for both the (100) and (111) orientations. In contrast, deposition on the same terminated surface was found to lead to a significantly lower attachment probability which generally decreases with increasing deposition angle, energy, and substrate temperature. Our results also indicated that deposition on the (111) surface leads to a significant excess Te sticking probability while the excess Te attachment probability for deposition on the (100) surface was found to be significantly smaller. In addition, while opposite termination deposition on the (111) surface was found to lead to growth of the next layer, deposition on the (100) surface was found to lead to interstitials in the surface layer. These results suggest - in agreement with a number of experiments - that the deposition of CdTe is likely to lead to excess Te as well as interstitial defects.

Finally, in Chapter 7 the results of accelerated molecular dynamics and energetics calculations of the binding energies, barriers, and prefactors for various stages of

CdTe(100) sublimation were presented. Our results indicate that while the desorption barriers for Te_2 on the Cd-terminated (100) surface are quite large, the corresponding prefactors are also extremely large. As a result, Cd desorption is the rate-limiting step for the case of sublimation via vacancy nucleation and growth, while the corresponding desorption barrier is in good agreement with the effective activation energy obtained in experiments for $T > 360°C$. A detailed analysis which takes into account the rates of both Cd and Te_2 desorption was also found to lead to good quantitative agreement with experiment over this temperature range. In contrast, our results indicate that at lower temperatures ($T < 360°C$) the desorption of isolated Cd atoms on the (2×1) Te-terminated surface may play an important role. This is supported by the fact that the corresponding desorption barrier ($E_d \simeq 1.4$ eV) was found to be close to that found experimentally over this temperature range. However, it is worth noting that while our simulations have provided insight into the kinetics of a number of important processes involved in CdTe(100) sublimation, to fully understand this process it is likely necessary to determine the desorption rates for a variety of other processes and environments beyond those which were analyzed in Chapter 7. However, an alternative approach would be to directly simulate the high-temperature sublimation of several layers of CdTe in order to directly determine the overall sublimation rate and associated mechanisms. While this is difficult to do with the methods used here, it should be possible by carrying out parallel replica simulations [208]. We believe that the development of such a method and its application to the study of high-temperature CdTe(100) and CdTe(111) sublimation would be an exciting direction to pursue in future work.

References

[1] I. Khatri, E. H. Sabbar, Y. Shim, and J. G. Amar, “Mechanism of stacking fault formation in metal (100) heteroepitaxial growth”, *Physical Review Materials*, vol. 4, no. 11, p. 113403, 2020.

[2] I. Khatri, N. Szymanski, B. Dumre, J. Amar, D. Gall, and S. Khare, “Correlating structure and orbital occupation with the stability and mechanical properties of 3d transition metal carbides”, *Journal of Alloys and Compounds*, vol. 891, p. 161866, 2022.

[3] I. Khatri and J. G. Amar, “Mechanism of CdTe (100) sublimation”, *Preprint*, 2022.

[4] I. Khatri, E. H. Sabbar, Y. Shim, and J. G. Amar, “Kinetically driven island morphology in growth on strained Cu (100)”, *The Journal of Chemical Physics*, vol. 155, no. 7, p. 074703, 2021.

[5] I. Khatri and J. G. Amar, “Energy, temperature, and deposition angle dependence of Cd and Te_2 deposited on CdTe”, *Thin Solid Films*, vol. 697, p. 137798, 2020.

[6] V. Adhikari, Z. Liu, N. Szymanski, I. Khatri, D. Gall, P. Sarin, and S. Khare, “First-principles study of mechanical and magnetic properties of transition metal (M) nitrides in the cubic M_4N structure”, *Journal of Physics and Chemistry of Solids*, vol. 120, pp. 197–206, 2018.

[7] B. Dumre, N. Szymanski, V. Adhikari, I. Khatri, D. Gall, and S. Khare, “Im-

proved optoelectronic properties in $\mathrm{CdSe}_x\mathrm{Te}_{1-x}$ through controlled composition and short-range order", *Solar Energy*, vol. 194, pp. 742–750, 2019.

[8] S. Hamadna, I. Khatri, E. H. Sabbar, and J. G. Amar, "Effects of short-range attachment barriers on submonolayer growth", *Surface Science*, vol. 715, p. 121938, 2022.

[9] V. Adhikari, N. Szymanski, I. Khatri, D. Gall, and S. Khare, "First principles investigation into the phase stability and enhanced hardness of TiN-ScN and TiN-YN alloys", *Thin Solid Films*, vol. 688, p. 137284, 2019.

[10] N. Szymanski, I. Khatri, J. Amar, D. Gall, and S. Khare, "Unconventional superconductivity in 3d rocksalt transition metal carbides", *Journal of Materials Chemistry C*, vol. 7, no. 40, pp. 12619–12632, 2019.

[11] I. Efthimiopoulos, I. Khatri, Z. T. Liu, S. V. Khare, P. Sarin, V. Tsurkan, A. Loidl, D. Zhang, and Y. Wang, "Universal link of magnetic exchange and structural behavior under pressure in chromium spinels", *Physical Review B*, vol. 97, no. 18, p. 184435, 2018.

[12] A. L. Allred and E. G. Rochow, "A scale of electronegativity based on electrostatic force", *Journal of Inorganic and Nuclear Chemistry*, vol. 5, no. 4, pp. 264–268, 1958.

[13] M. C. Payne, M. P. Teter, D. C. Allan, T. Arias, and a. J. Joannopoulos, "Iterative minimization techniques for ab initio total-energy calculations: molecular dynamics and conjugate gradients", *Reviews of modern physics*, vol. 64, no. 4, p. 1045, 1992.

[14] S. T. Chill, *Methods, software, and benchmarks for modeling long timescale dynamics in solid-state atomic systems.* PhD thesis, The University of Texas At Austin, 2014.

[15] M. R. So/rensen and A. F. Voter, “Temperature-accelerated dynamics for simulation of infrequent events”, *The Journal of Chemical Physics*, vol. 112, no. 21, pp. 9599–9606, 2000.

[16] R. D. Shannon, D. B. Rogers, C. T. Prewitt, and J. L. Gillson, “Chemistry of noble metal oxides. iii. electrical transport properties and crystal chemistry of ABO_2 compounds with the delafossite structure”, *Inorganic Chemistry*, vol. 10, no. 4, pp. 723–727, 1971.

[17] J. Häglund, A. F. Guillermet, G. Grimvall, and M. Körling, “Theory of bonding in transition-metal carbides and nitrides”, *Physical Review B*, vol. 48, no. 16, p. 11685, 1993.

[18] B. Müller, L. Nedelmann, B. Fischer, H. Brune, and J. Barth, “K. 80 kern, d. erdös and j. wollschläger”, *Surface Review Letters*, vol. 5, pp. 769–781, 1998.

[19] Müller, Bert and Fischer, Bjørn and Nedelmann, Lorenz and Fricke, Alexander and Kern, Klaus, “Strain relief at metal interfaces with square symmetry”, *Physical review letters*, vol. 76, no. 13, p. 2358, 1996.

[20] Z. Barber, *Introduction to materials modelling.* Maney Pub., 2005.

[21] M. Born and R. Oppenheimer, “Zur quantentheorie der molekeln”, *Annalen der physik*, vol. 389, no. 20, pp. 457–484, 1927.

[22] P. Hohenberg and W. Kohn, “Inhomogeneous electron gas phys. rev. 136”, *B864*, 1964.

[23] W. Kohn and L. J. Sham, “Self-consistent equations including exchange and correlation effects”, *Physical review*, vol. 140, no. 4A, p. A1133, 1965.

[24] L. Hedin and B. I. Lundqvist, “Explicit local exchange-correlation potentials”, *Journal of Physics C: Solid state physics*, vol. 4, no. 14, p. 2064, 1971.

[25] J. P. Perdew, J. A. Chevary, S. H. Vosko, K. A. Jackson, M. R. Pederson, D. J. Singh, and C. Fiolhais, "Atoms, molecules, solids, and surfaces: Applications of the generalized gradient approximation for exchange and correlation", *Physical review B*, vol. 46, no. 11, p. 6671, 1992.

[26] J. P. Perdew, J. Chevary, S. Vosko, K. A. Jackson, M. R. Pederson, D. Singh, and C. Fiolhais, "Erratum: Atoms, molecules, solids, and surfaces: Applications of the generalized gradient approximation for exchange and correlation", *Physical Review B*, vol. 48, no. 7, p. 4978, 1993.

[27] J. P. Perdew, K. Burke, and M. Ernzerhof, "Generalized gradient approximation made simple", *Physical review letters*, vol. 77, no. 18, p. 3865, 1996.

[28] G. Kresse and J. Hafner, "Ab initio molecular-dynamics simulation of the liquid-metal–amorphous-semiconductor transition in germanium", *Physical Review B*, vol. 49, no. 20, p. 14251, 1994.

[29] G. Kresse and J. Furthmüller, "Efficiency of ab-initio total energy calculations for metals and semiconductors using a plane-wave basis set", *Computational materials science*, vol. 6, no. 1, pp. 15–50, 1996.

[30] G. Kresse and J. Hafner, "Ab initio molecular dynamics for liquid metals", *Physical review B*, vol. 47, no. 1, p. 558, 1993.

[31] G. Kresse and J. Furthmüller, "Efficient iterative schemes for ab initio total-energy calculations using a plane-wave basis set", *Physical review B*, vol. 54, no. 16, p. 11169, 1996.

[32] G. Kresse and D. Joubert, "From ultrasoft pseudopotentials to the projector augmented-wave method", *Physical review B*, vol. 59, no. 3, p. 1758, 1999.

[33] L. Verlet, “Computer” experiments” on classical fluids. i. thermodynamical properties of lennard-jones molecules”, *Physical review*, vol. 159, no. 1, p. 98, 1967.

[34] W. C. Swope, H. C. Andersen, P. H. Berens, and K. R. Wilson, “A computer simulation method for the calculation of equilibrium constants for the formation of physical clusters of molecules: Application to small water clusters”, *The Journal of chemical physics*, vol. 76, no. 1, pp. 637–649, 1982.

[35] H. J. Berendsen, J. v. Postma, W. F. Van Gunsteren, A. DiNola, and J. R. Haak, “Molecular dynamics with coupling to an external bath”, *The Journal of chemical physics*, vol. 81, no. 8, pp. 3684–3690, 1984.

[36] M. S. Daw and M. I. Baskes, “Semiempirical, quantum mechanical calculation of hydrogen embrittlement in metals”, *Physical review letters*, vol. 50, no. 17, p. 1285, 1983.

[37] X. Zhou, N. Bartelt, and R. Sills, “Enabling simulations of helium bubble nucleation and growth: A strategy for interatomic potentials”, *Physical Review B*, vol. 103, no. 1, p. 014108, 2021.

[38] I. Oleinik and D. Pettifor, “Analytic bond-order potentials beyond tersoff-brenner. ii”.

[39] D. Pettifor and I. Oleinik, “Bounded analytic bond-order potentials for σ and π bonds”, *Physical review letters*, vol. 84, no. 18, p. 4124, 2000.

[40] D. Pettifor, M. Finnis, D. Nguyen-Manh, D. Murdick, X. Zhou, and H. Wadley, “Analytic bond-order potentials for multicomponent systems”, *Materials Science and Engineering: A*, vol. 365, no. 1-2, pp. 2–13, 2004.

[41] R. C. Iotti, E. Ciancio, and F. Rossi, “Quantum transport theory for semiconductor nanostructures: A density-matrix formulation”, *Physical Review B*, vol. 72, no. 12, p. 125347, 2005.

[42] D. Pettifor and I. Oleinik, “Analytic bond-order potential for open and close-packed phases”, *Physical Review B*, vol. 65, no. 17, p. 172103, 2002.

[43] D. K. Ward, X. W. Zhou, B. M. Wong, F. P. Doty, and J. A. Zimmerman, “Analytical bond-order potential for the cadmium telluride binary system”, *Physical Review B*, vol. 85, no. 11, p. 115206, 2012.

[44] R. J. Zamora, B. P. Uberuaga, D. Perez, and A. F. Voter, “The modern temperature-accelerated dynamics approach”, *Annual review of chemical and biomolecular engineering*, vol. 7, pp. 87–110, 2016.

[45] Y. Shim and J. G. Amar, “Improved scaling of temperature-accelerated dynamics using localization”, *The Journal of chemical physics*, vol. 145, no. 1, p. 014105, 2016.

[46] D. Perez, B. P. Uberuaga, Y. Shim, J. G. Amar, and A. F. Voter, “Accelerated molecular dynamics methods: introduction and recent developments”, *Annual Reports in computational chemistry*, vol. 5, pp. 79–98, 2009.

[47] G. Henkelman, “Atomistic simulations of activated processes in materials”, *Annual Review of Materials Research*, vol. 47, pp. 199–216, 2017.

[48] H. H. Hwu and J. G. Chen, “Surface chemistry of transition metal carbides”, *Chemical reviews*, vol. 105, no. 1, pp. 185–212, 2005.

[49] H. Li, L. Zhang, Q. Zeng, K. Guan, K. Li, H. Ren, S. Liu, and L. Cheng, “Structural, elastic and electronic properties of transition metal carbides TMC

(TM= Ti, Zr, Hf and Ta) from first-principles calculations", *Solid state communications*, vol. 151, no. 8, pp. 602–606, 2011.

[50] X. Zhou, D. Gall, and S. V. Khare, "Mechanical properties and electronic structure of anti-ReO$_3$ structured cubic nitrides, M$_3$N, of d block transition metals M: An ab initio study", *Journal of alloys and compounds*, vol. 595, pp. 80–86, 2014.

[51] K. Balasubramanian, S. V. Khare, and D. Gall, "Energetics of point defects in rocksalt structure transition metal nitrides: Thermodynamic reasons for deviations from stoichiometry", *Acta Materialia*, vol. 159, pp. 77–88, 2018.

[52] L. Toth, *Transition metal carbides and nitrides.* Elsevier, 2014.

[53] C. Kral, W. Lengauer, D. Rafaja, and P. Ettmayer, "Critical review on the elastic properties of transition metal carbides, nitrides and carbonitrides", *Journal of Alloys and Compounds*, vol. 265, no. 1-2, pp. 215–233, 1998.

[54] J. Chen, J. Eng Jr, and S. Kelty, "Nexafs determination of electronic and catalytic properties of transition metal carbides and nitrides: From single crystal surfaces to powder catalysts", *Catalysis today*, vol. 43, no. 1-2, pp. 147–158, 1998.

[55] S. Kodambaka, S. Khare, V. Petrova, D. Johnson, I. Petrov, and J. Greene, "Absolute orientation-dependent anisotropic tin (111) island step energies and stiffnesses from shape fluctuation analyses", *Physical Review B*, vol. 67, no. 3, p. 035409, 2003.

[56] L. I. Johansson, "Electronic and structural properties of transition-metal carbide and nitride surfaces", *Surface science reports*, vol. 21, no. 5-6, pp. 177–250, 1995.

[57] K. Zhang, K. Balasubramanian, B. Ozsdolay, C. Mulligan, S. Khare, W. Zheng, and D. Gall, "Growth and mechanical properties of epitaxial nbn (001) films on mgo (001)", *Surface and Coatings Technology*, vol. 288, pp. 105–114, 2016.

[58] J. Häglund, G. Grimvall, T. Jarlborg, and A. F. Guillermet, "Band structure and cohesive properties of 3d-transition-metal carbides and nitrides with the NaCl-type structure", *Physical Review B*, vol. 43, no. 18, p. 14400, 1991.

[59] S. Kodambaka, V. Petrova, S. Khare, D. Gall, A. Rockett, I. Petrov, and J. Greene, "Size-dependent detachment-limited decay kinetics of two-dimensional TiN islands on TiN (111)", *Physical review letters*, vol. 89, no. 17, p. 176102, 2002.

[60] N. Koutná, A. Brenner, D. Holec, and P. H. Mayrhofer, "High-throughput first-principles search for ceramic superlattices with improved ductility and fracture resistance", *Acta Materialia*, vol. 206, p. 116615, 2021.

[61] F. Benesovsky, R. Kieffer, and P. Ettmayer, "Nitrides", *Encyclopedia of chemical technology*, vol. 15, pp. 871–81, 1981.

[62] R. Levy and M. Boudart, "Platinum-like behavior of tungsten carbide in surface catalysis", *science*, vol. 181, no. 4099, pp. 547–549, 1973.

[63] J. Warner, S. Patil, S. Khare, and K. Masiulaniec, "Ab initio calculations for properties of MAX phases Ti_2TlC, Zr_2TlC, and Hf_2TlC", *Applied physics letters*, vol. 88, no. 10, p. 101911, 2006.

[64] S. T. Oyama, "Introduction to the chemistry of transition metal carbides and nitrides", in *The chemistry of transition metal carbides and nitrides*, pp. 1–27, Springer, 1996.

[65] S. Oyama, “Preparation and catalytic properties of transition metal carbides and nitrides”, *Catalysis today*, vol. 15, no. 2, pp. 179–200, 1992.

[66] S. Patil, N. Mangale, S. Khare, and S. Marsillac, “Super hard cubic phases of period VI transition metal nitrides: First principles investigation”, *Thin Solid Films*, vol. 517, no. 2, pp. 824–827, 2008.

[67] L.-L. Wang, S. V. Khare, V. Chirita, D. D. Johnson, A. A. Rockett, A. I. Frenkel, N. H. Mack, and R. G. Nuzzo, “Origin of bulklike structure and bond length disorder of Pt_{37} and Pt_6Ru_{31} clusters on carbon: Comparison of theory and experiment”, *Journal of the American Chemical Society*, vol. 128, no. 1, pp. 131–142, 2006.

[68] B. Ozsdolay, C. Mulligan, K. Balasubramanian, L. Huang, S. Khare, and D. Gall, “Cubic β-WN_x layers: Growth and properties vs N-to-W ratio”, *Surface and Coatings Technology*, vol. 304, pp. 98–107, 2016.

[69] S. Khare and T. Einstein, “Energetics of steps and kinks on Ag and Pt using equivalent crystal theory (ECT)”, *Surface science*, vol. 314, no. 1, pp. L857–L865, 1994.

[70] J. Musil, “Hard and superhard nanocomposite coatings”, *Surface and coatings technology*, vol. 125, no. 1-3, pp. 322–330, 2000.

[71] M. Yasuoka, P. Wang, and R. Murakami, “Comparison of the mechanical performance of cutting tools coated by either a TiC_xN_{1-x} single-layer or a $TiC/TiC_{0.5}N_{0.5}/TiN$ multilayer using the hollow cathode discharge ion plating method”, *Surface and Coatings Technology*, vol. 206, no. 8-9, pp. 2168–2172, 2012.

[72] Y. Zhong, X. Xia, F. Shi, J. Zhan, J. Tu, and H. J. Fan, “Transition metal car-

bides and nitrides in energy storage and conversion", *Advanced science*, vol. 3, no. 5, p. 1500286, 2016.

[73] B. Anasori, M. R. Lukatskaya, and Y. Gogotsi, "2d metal carbides and nitrides (MXenes) for energy storage", *Nature Reviews Materials*, vol. 2, no. 2, pp. 1–17, 2017.

[74] M. Nagai and T. Kurakami, "Reverse water gas shift reaction over molybdenum carbide", *Journal of chemical engineering of Japan*, vol. 38, no. 10, pp. 807–812, 2005.

[75] R. Zhan and X. Luo, "Topologically nontrivial phases in superconducting transition metal carbides", *Journal of Applied Physics*, vol. 125, no. 5, p. 053903, 2019.

[76] A. F. Guillermet, J. Häglund, and G. Grimvall, "Cohesive properties of 4d-transition-metal carbides and nitrides in the NaCl-type structure", *Physical Review B*, vol. 45, no. 20, p. 11557, 1992.

[77] K. Balasubramanian, S. V. Khare, and D. Gall, "Valence electron concentration as an indicator for mechanical properties in rocksalt structure nitrides, carbides and carbonitrides", *Acta Materialia*, vol. 152, pp. 175–185, 2018.

[78] Z. Liu, X. Zhou, S. Khare, and D. Gall, "Structural, mechanical and electronic properties of 3d transition metal nitrides in cubic zincblende, rocksalt and cesium chloride structures: a first-principles investigation", *Journal of Physics: Condensed Matter*, vol. 26, no. 2, p. 025404, 2013.

[79] L. Wu, T. Yao, Y. Wang, J. Zhang, F. Xiao, and B. Liao, "Understanding the mechanical properties of vanadium carbides: Nano-indentation measurement and first-principles calculations", *Journal of alloys and compounds*, vol. 548, pp. 60–64, 2013.

[80] D. Koelling and G. Arbman, "Use of energy derivative of the radial solution in an augmented plane wave method: application to copper", *Journal of Physics F: Metal Physics*, vol. 5, no. 11, p. 2041, 1975.

[81] A. F. Guillermet and G. Grimvall, "Cohesive properties and vibrational entropy of 3d transition-metal compounds: MX (NaCl) compounds (X= C, N, O, S), complex carbides, and nitrides", *Physical Review B*, vol. 40, no. 15, p. 10582, 1989.

[82] J. E. Krzanowski and R. E. Leuchtner, "Chemical, mechanical, and tribological properties of pulsed-laser-deposited titanium carbide and vanadium carbide", *Journal of the American Ceramic Society*, vol. 80, no. 5, pp. 1277–1280, 1997.

[83] R. Ahuja, O. Eriksson, J. Wills, and B. Johansson, "Structural, elastic, and high-pressure properties of cubic TiC, TiN, and TiO", *Physical review B*, vol. 53, no. 6, p. 3072, 1996.

[84] S.-H. Cai and C.-W. Liu, "Studies on the band structures of some layered transition metal dichalcogenides", *Journal of Molecular Structure: THEOCHEM*, vol. 362, no. 3, pp. 379–385, 1996.

[85] A. Neckel, "Recent investigations on the electronic structure of the fourth and fifth group transition metal monocarbides, mononitrides, and monoxides", *International Journal of Quantum Chemistry*, vol. 23, no. 4, pp. 1317–1353, 1983.

[86] D. J. Singh and B. M. Klein, "Electronic structure, lattice stability, and superconductivity of CrC", *Physical Review B*, vol. 46, no. 23, p. 14969, 1992.

[87] L. Benco, "Metal-to-metal bonding in transition metal monocarbides and mononitrides", *Journal of Solid State Chemistry*, vol. 128, no. 1, pp. 121–129, 1997.

[88] K. Korir, G. Amolo, N. Makau, and D. Joubert, “First-principle calculations of the bulk properties of 4d transition metal carbides and nitrides in the rocksalt, zincblende and wurtzite structures”, *Diamond and related materials*, vol. 20, no. 2, pp. 157–164, 2011.

[89] C. Paduani, “Electronic structure and fermi surfaces of transition metal carbides with rocksalt structure”, *Journal of Physics: Condensed Matter*, vol. 20, no. 22, p. 225014, 2008.

[90] M. G. Quesne, A. Roldan, N. H. de Leeuw, and C. R. A. Catlow, “Bulk and surface properties of metal carbides: implications for catalysis”, *Physical Chemistry Chemical Physics*, vol. 20, no. 10, pp. 6905–6916, 2018.

[91] Y.-H. Zhao, H.-Y. Su, K. Sun, J. Liu, and W.-X. Li, “Structural and electronic properties of cobalt carbide Co_2C and its surface stability: Density functional theory study”, *Surface science*, vol. 606, no. 5-6, pp. 598–604, 2012.

[92] A. Vojvodic and C. Ruberto, “Trends in bulk electron-structural features of rocksalt early transition-metal carbides”, *Journal of Physics: Condensed Matter*, vol. 22, no. 37, p. 375501, 2010.

[93] J. Maibam, B. I. Sharma, R. Bhattacharjee, R. Thapa, and R. B. Singh, “Electronic structure and elastic properties of scandium carbide and yttrium carbide: A first principles study”, *Physica B: Condensed Matter*, vol. 406, no. 21, pp. 4041–4045, 2011.

[94] A. F. Guillermet, J. Häglund, and G. Grimvall, “Cohesive properties and electronic structure of 5d-transition-metal carbides and nitrides in the NaCl structure”, *Physical Review B*, vol. 48, no. 16, p. 11673, 1993.

[95] J. C. Grossman, A. Mizel, M. Côté, M. L. Cohen, and S. G. Louie, “Transition

metals and their carbides and nitrides: Trends in electronic and structural properties", *Physical review B*, vol. 60, no. 9, p. 6343, 1999.

[96] F. Viñes, C. Sousa, P. Liu, J. Rodriguez, and F. Illas, "A systematic density functional theory study of the electronic structure of bulk and (001) surface of transition-metals carbides", *The Journal of chemical physics*, vol. 122, no. 17, p. 174709, 2005.

[97] Y. Yang, H. Lu, C. Yu, and J. Chen, "First-principles calculations of mechanical properties of TiC and TiN", *Journal of Alloys and Compounds*, vol. 485, no. 1-2, pp. 542–547, 2009.

[98] M. Fukuichi, H. Momida, M. Geshi, M. Michiuchi, K. Sogabe, and T. Oguchi, "First-principles calculations on the origin of mechanical properties and electronic structures of 5 d transition metal monocarbides MC (M= Hf, Ta, W, Re, Os, Ir, and Pt)", *Journal of the Physical Society of Japan*, vol. 87, no. 4, p. 044602, 2018.

[99] S. Pugh, "XCII. relations between the elastic moduli and the plastic properties of polycrystalline pure metals", *The London, Edinburgh, and Dublin Philosophical Magazine and Journal of Science*, vol. 45, no. 367, pp. 823–843, 1954.

[100] P. E. Blöchl, "Projector augmented-wave method", *Physical review B*, vol. 50, no. 24, p. 17953, 1994.

[101] H. J. Monkhorst and J. D. Pack, "Special points for brillouin-zone integrations", *Physical review B*, vol. 13, no. 12, p. 5188, 1976.

[102] J. D. Pack and H. J. Monkhorst, """ special points for brillouin-zone integrations"—a reply", *Physical Review B*, vol. 16, no. 4, p. 1748, 1977.

[103] I. Efthimiopoulos, V. Tsurkan, A. Loidl, D. Zhang, and Y. Wang, "Comparing the pressure-induced structural behavior of $CuCr_2O_4$ and $CuCr_2Se_4$ spinels", *The Journal of Physical Chemistry C*, vol. 121, no. 30, pp. 16513–16520, 2017.

[104] H. Fu, D. Li, F. Peng, T. Gao, and X. Cheng, "Ab initio calculations of elastic constants and thermodynamic properties of nial under high pressures", *Computational Materials Science*, vol. 44, no. 2, pp. 774–778, 2008.

[105] F. Murnaghan, "The compressibility of media under extreme pressures", *Proceedings of the national academy of sciences of the United States of America*, vol. 30, no. 9, p. 244, 1944.

[106] F. Mouhat and F.-X. Coudert, "Necessary and sufficient elastic stability conditions in various crystal systems", *Physical review B*, vol. 90, no. 22, p. 224104, 2014.

[107] J. F. Nye *et al.*, *Physical properties of crystals: their representation by tensors and matrices.* Oxford university press, 1985.

[108] A. Togo and I. Tanaka, "First principles phonon calculations in materials science", *Scripta Materialia*, vol. 108, pp. 1–5, 2015.

[109] L. Ward, A. Dunn, A. Faghaninia, N. E. Zimmermann, S. Bajaj, Q. Wang, J. Montoya, J. Chen, K. Bystrom, M. Dylla, *et al.*, "Matminer: An open source toolkit for materials data mining", *Computational Materials Science*, vol. 152, pp. 60–69, 2018.

[110] Y. Tian, B. Xu, and Z. Zhao, "Microscopic theory of hardness and design of novel superhard crystals", *International Journal of Refractory Metals and Hard Materials*, vol. 33, pp. 93–106, 2012.

[111] P. E. Blöchl, O. Jepsen, and O. K. Andersen, "Improved tetrahedron method for brillouin-zone integrations", *Physical Review B*, vol. 49, no. 23, p. 16223, 1994.

[112] F. W. Biegler-könig, R. F. Bader, and T.-H. Tang, "Calculation of the average properties of atoms in molecules. II", *Journal of Computational chemistry*, vol. 3, no. 3, pp. 317–328, 1982.

[113] E. Sanville, S. D. Kenny, R. Smith, and G. Henkelman, "Improved grid-based algorithm for bader charge allocation", *Journal of computational chemistry*, vol. 28, no. 5, pp. 899–908, 2007.

[114] G. Henkelman, A. Arnaldsson, and H. Jónsson, "A fast and robust algorithm for bader decomposition of charge density", *Computational Materials Science*, vol. 36, no. 3, pp. 354–360, 2006.

[115] V. L. Deringer, A. L. Tchougréeff, and R. Dronskowski, "Crystal orbital hamilton population (COHP) analysis as projected from plane-wave basis sets", *The journal of physical chemistry A*, vol. 115, no. 21, pp. 5461–5466, 2011.

[116] R. Dronskowski and P. E. Bloechl, "Crystal orbital hamilton populations (COHP): energy-resolved visualization of chemical bonding in solids based on density-functional calculations", *The Journal of Physical Chemistry*, vol. 97, no. 33, pp. 8617–8624, 1993.

[117] S. Maintz, V. L. Deringer, A. L. Tchougréeff, and R. Dronskowski, "Analytic projection from plane-wave and paw wavefunctions and application to chemical-bonding analysis in solids", *Journal of computational chemistry*, vol. 34, no. 29, pp. 2557–2567, 2013.

[118] S. Maintz, M. Esser, and R. Dronskowski, "Efficient rotation of local basis

functions using real spherical harmonics.", *Acta Physica Polonica B*, vol. 47, no. 4, 2016.

[119] S. Maintz, V. L. Deringer, A. L. Tchougréeff, and R. Dronskowski, "LOBSTER: A tool to extract chemical bonding from plane-wave based dft", 2016.

[120] H. M. Tütüncü, S. Bağcı, G. Srivastava, and A. Akbulut, "Electrons, phonons and superconductivity in rocksalt and tungsten–carbide phases of CrC", *Journal of Physics: Condensed Matter*, vol. 24, no. 45, p. 455704, 2012.

[121] A. Jain, S. P. Ong, G. Hautier, W. Chen, W. D. Richards, S. Dacek, S. Cholia, D. Gunter, D. Skinner, G. Ceder, *et al.*, "Commentary: The materials project: A materials genome approach to accelerating materials innovation", *APL materials*, vol. 1, no. 1, p. 011002, 2013.

[122] R. W. G. Wyckoff, *The structure of crystals*, vol. 1. Chemical Catalog Company, Incorporated, 1924.

[123] B. Liu and X. Cheng, "A metastable Cr carbide of NaCl structure formed by carbon-ion implantation into chromium films", *Journal of Physics: Condensed Matter*, vol. 4, no. 16, p. L265, 1992.

[124] E. K. Abavare, S. N. Dodoo, K. Uchida, G. K. Nkurumah-Buandoh, A. Yaya, and A. Oshiyama, "Indirect phase transition of TiC, ZrC, and HfC crystal structures", *physica status solidi (b)*, vol. 253, no. 6, pp. 1177–1185, 2016.

[125] A. N. Christensen, "The temperature factor parameters of some transition metal carbides and nitrides by single crystal X-RAY and neutron diffraction.", *Acta Chemica Scandinavica*, 1978.

[126] D. Kepert, "Aspects of the stereochemistry of eight-coordination", *Prog. Inorg. Chem*, vol. 24, pp. 179–249, 1978.

[127] C. Haigh, “Enumeration by pólya’s theorem of the isomerism in eight-coordinate complexes in square antiprismatic, triangular dodecahedral and hendecahedral (bicapped trigonal prismatic) geometries”, *Polyhedron*, vol. 15, no. 4, pp. 605–643, 1996.

[128] P. Bhardwaj, “Structural study of transition metal carbides”, *Acta Physica Polonica-Series A General Physics*, vol. 122, no. 1, p. 138, 2012.

[129] K. Kim, V. Ozoliņš, and A. Zunger, “Instability of the high-pressure CsCl structure in most iii-v semiconductors”, *Physical Review B*, vol. 60, no. 12, p. R8449, 1999.

[130] O. C. Gagné and F. C. Hawthorne, “Bond-length distributions for ions bonded to oxygen: Results for the transition metals and quantification of the factors underlying bond-length variation in inorganic solids”, *IUCrJ*, vol. 7, no. 4, pp. 581–629, 2020.

[131] K. Chen and S. Kamran, “Bonding characteristics of TiC and TiN”, *Modeling and Numerical Simulation of Material Science*, vol. 3, no. 1, 2013.

[132] C. E. Housecroft and A. G. Sharpe, “Chapter 22: d-block metal chemistry: the first row elements”, *Inorganic Chemistry,*, p. 716, 2008.

[133] M. A. Halcrow, “Jahn–teller distortions in transition metal compounds, and their importance in functional molecular and inorganic materials”, *Chemical Society Reviews*, vol. 42, no. 4, pp. 1784–1795, 2013.

[134] D. Reinen, M. Atanasov, G. Nikolov, and F. Steffens, “Local and cooperative jahn-teller distortions of nickel (2^+) and copper (2^+) in tetrahedral coordination”, *Inorganic Chemistry*, vol. 27, no. 10, pp. 1678–1686, 1988.

[135] R. Janes and E. A. Moore, *Metal-ligand bonding.* Royal society of chemistry, 2004.

[136] E. A. Juarez-Arellano, B. Winkler, L. Bayarjargal, A. Friedrich, V. Milman, D. R. Kammler, S. M. Clark, J. Yan, M. Koch-Müller, F. Schröder, *et al.*, "Formation of scandium carbides and scandium oxycarbide from the elements at high-(P, T) conditions", *Journal of Solid State Chemistry*, vol. 183, no. 5, pp. 975–983, 2010.

[137] E. Zhang, S. Zeng, Q. Li, Y. Bo, and M. Ma, "A study on the kinetic process of reaction synthesis of TiC: Part I. experimental research and theoretical model", *Metallurgical and Materials Transactions A*, vol. 30, no. 4, pp. 1147–1151, 1999.

[138] S. M. Schmuecker, D. Clouser, T. J. Kraus, and B. M. Leonard, "Synthesis of metastable chromium carbide nanomaterials and their electrocatalytic activity for the hydrogen evolution reaction", *Dalton Transactions*, vol. 46, no. 39, pp. 13524–13530, 2017.

[139] K. H. J. Buschow, F. R. Boer, *et al.*, *Physics of magnetism and magnetic materials*, vol. 7. Springer, 2003.

[140] V. Zhukov, V. Gubanov, O. Jepsen, N. Christensen, and O. Andersen, "Calculated energy-band structures and chemical bonding in titanium and vanadium carbides, nitrides and oxides", *Journal of Physics and Chemistry of Solids*, vol. 49, no. 7, pp. 841–849, 1988.

[141] P. Soni, G. Pagare, and S. P. Sanyal, "Structural, high pressure and elastic properties of transition metal monocarbides: A FP-LAPW study", *Journal of Physics and Chemistry of Solids*, vol. 72, no. 6, pp. 810–816, 2011.

[142] Y. Liang, X.-F. Wei, C. Gu, J.-X. Liu, F. Li, M. Yan, X. Zheng, Z. Han,

Y. Zhao, S. Wang, *et al.*, "Enhanced hardness in transition-metal monocarbides via optimal occupancy of bonding orbitals", *ACS Applied Materials & Interfaces*, vol. 13, no. 12, pp. 14365–14376, 2021.

[143] S.-H. Jhi, J. Ihm, S. G. Louie, and M. L. Cohen, "Electronic mechanism of hardness enhancement in transition-metal carbonitrides", *Nature*, vol. 399, no. 6732, pp. 132–134, 1999.

[144] N. R. Rathod, S. K. Gupta, and P. K. Jha, "First-principles structural, electronic and vibrational properties of zinc-blende zirconium carbide", *Solid state communications*, vol. 169, pp. 32–36, 2013.

[145] A. Teber, F. Schoenstein, F. Têtard, M. Abdellaoui, and N. Jouini, "Effect of SPS process sintering on the microstructure and mechanical properties of nanocrystalline TiC for tools application", *International Journal of Refractory Metals and Hard Materials*, vol. 30, no. 1, pp. 64–70, 2012.

[146] D. Bandyopadhyay, R. Sharma, and N. Chakraborti, "The Ti-Cr-C (titanium-chromium-carbon) system", *Journal of phase equilibria*, vol. 20, no. 3, pp. 325–331, 1999.

[147] R. Asaro and W. Tiller, "Interface morphology development during stress corrosion cracking: Part i. via surface diffusion", *Metallurgical and Materials Transactions B*, vol. 3, no. 7, pp. 1789–1796, 1972.

[148] M. A. Grinfeld, "Instability of the separation boundry between a nonhydrostatically stressed elastic body and a melt", *Sov. Phys. Doklady*, vol. 31, pp. 831–835, 1986.

[149] C. Humphreys, D. Maher, D. Eaglesham, E. Kvam, and I. Salisbury, "The origin of dislocations in multilayers", *Journal de Physique III*, vol. 1, no. 6, pp. 1119–1130, 1991.

[150] Y.-W. Mo, D. Savage, B. Swartzentruber, and M. G. Lagally, “Kinetic pathway in stranski-krastanov growth of Ge on Si (001)”, *Physical review letters*, vol. 65, no. 8, p. 1020, 1990.

[151] J. Tersoff and R. Tromp, “Shape transition in growth of strained islands: Spontaneous formation of quantum wires”, *Physical review letters*, vol. 70, no. 18, p. 2782, 1993.

[152] B. Müller, L. Nedelmann, B. Fischer, A. Fricke, and K. Kern, “Strain relief in metal heteroepitaxy on face-centered-cubic (100): Cu/Ni (100)”, *Journal of Vacuum Science & Technology A: Vacuum, Surfaces, and Films*, vol. 14, no. 3, pp. 1878–1881, 1996.

[153] B. Müller, L. Nedelmann, B. Fischer, H. Brune, J. V. Barth, and K. Kern, “Island shape transition in heteroepitaxial metal growth on square lattices”, *Physical review letters*, vol. 80, no. 12, p. 2642, 1998.

[154] S. Brongersma, M. Castell, D. Perovic, and M. Zinke-Allmang, “Stress-induced shape transition of $CoSi_2$ clusters on Si (100)”, *Physical review letters*, vol. 80, no. 17, p. 3795, 1998.

[155] J. Hrbek and R. Hwang, “Interaction of adsorbates on strained metallic layers”, *Current Opinion in Solid State and Materials Science*, vol. 5, no. 1, pp. 67–73, 2001.

[156] W. Ma, R. Nötzel, H.-P. Schönherr, and K. H. Ploog, “Shape transition of coherent three-dimensional (In, Ga) As islands on GaAs (100)”, *Applied Physics Letters*, vol. 79, no. 25, pp. 4219–4221, 2001.

[157] V. Fournée, J. Ledieu, T. Cai, and P. A. Thiel, “Influence of strain in Ag on Al (111) and Al on Ag (100) thin film growth”, *Physical Review B*, vol. 67, no. 15, p. 155401, 2003.

[158] N. Medhekar, V. Shenoy, J. Hannon, and R. Tromp, “Metastability in 2d self-assembling systems”, *Physical review letters*, vol. 99, no. 15, p. 156102, 2007.

[159] M. S. Marshall and M. R. Castell, “Shape transitions of epitaxial islands during strained layer growth: anatase TiO_2 (001) on $SrTiO_3$ (001)”, *Physical review letters*, vol. 102, no. 14, p. 146102, 2009.

[160] Y. Li, M. Liu, D. Ma, D. Yu, X. Chen, X.-C. Ma, Q.-K. Xue, K. Xu, J.-F. Jia, and F. Liu, “Bistability of Nanoscale Ag Islands on a Si (111)-(4× 1)- In Surface Induced by Anisotropic Stress”, *Physical review letters*, vol. 103, no. 7, p. 076102, 2009.

[161] K. Liu, I. Berbezier, T. David, L. Favre, A. Ronda, M. Abbarchi, P. Voorhees, and J.-N. Aqua, “Nucleation versus instability race in strained films”, *Physical Review Materials*, vol. 1, no. 5, p. 053402, 2017.

[162] J. de la Figuera, K. McCarty, and N. Bartelt, “Metastable misfit dislocations during thin-film growth: The case of Cu on Ru (0001)”, *Surface Science*, vol. 682, pp. 43–50, 2019.

[163] A. Li, F. Liu, and M. Lagally, “Equilibrium shape of two-dimensional islands under stress”, *Physical review letters*, vol. 85, no. 9, p. 1922, 2000.

[164] Y. Shim and J. G. Amar, “Shape transitions in strained Cu islands on Ni (100): kinetics versus energetics”, *Physical review letters*, vol. 108, no. 7, p. 076102, 2012.

[165] Z. Chen, J. Zhang, S. Xu, J. Xue, T. Jiang, and Y. Hao, “Influence of stacking faults on the quality of GaN films grown on sapphire substrate using a sputtered AlN nucleation layer”, *Materials Research Bulletin*, vol. 89, pp. 193–196, 2017.

[166] X. Feng, J. U. Surjadi, X. Li, and Y. Lu, "Size dependency in stacking fault-mediated ultrahard high-entropy alloy thin films", *Journal of Alloys and Compounds*, vol. 844, p. 156187, 2020.

[167] Y. Mishin, M. Mehl, D. Papaconstantopoulos, A. Voter, and J. Kress, "Structural stability and lattice defects in copper: Ab initio, tight-binding, and embedded-atom calculations", *Physical Review B*, vol. 63, no. 22, p. 224106, 2001.

[168] M. Allen and D. Tildesley, "Computer simulation of liquids", 1987.

[169] G. H. Vineyard, "Frequency factors and isotope effects in solid state rate processes", *Journal of Physics and Chemistry of Solids*, vol. 3, no. 1-2, pp. 121–127, 1957.

[170] B. Uberuaga, R. Hoagland, A. Voter, and S. Valone, "Direct transformation of vacancy voids to stacking fault tetrahedra", *Physical review letters*, vol. 99, no. 13, p. 135501, 2007.

[171] C. Ratsch, "Strain dependence for microscopic growth parameters for Ag on Ag (100)", *Physical Review B*, vol. 83, no. 15, p. 153406, 2011.

[172] D. Shu, F. Liu, and X. Gong, "Simple generic method for predicting the effect of strain on surface diffusion", *Physical Review B*, vol. 64, no. 24, p. 245410, 2001.

[173] G. Medeiros-Ribeiro, T. Kamins, D. Ohlberg, and R. S. Williams, "Annealing of Ge nanocrystals on Si (001) at 550 C: Metastability of huts and the stability of pyramids and domes", *Physical Review B*, vol. 58, no. 7, p. 3533, 1998.

[174] P. Grütter and U. Dürig, "Quasidendritic growth of Co induced by localized

reconstruction of Pt (111)", *Surface science*, vol. 337, no. 1-2, pp. 147–152, 1995.

[175] M. Bott, M. Hohage, T. Michely, and G. Comsa, "Pt (111) reconstruction induced by enhanced Pt gas-phase chemical potential", *Physical review letters*, vol. 70, no. 10, p. 1489, 1993.

[176] M. Gloeckler, I. Sankin, and Z. Zhao, "CdTe solar cells at the threshold to 20% efficiency", *IEEE Journal of Photovoltaics*, vol. 3, no. 4, pp. 1389–1393, 2013.

[177] J. Sites, A. Munshi, J. Kephart, D. Swanson, and W. Sampath, "Progress and challenges with CdTe cell efficiency", in *2016 IEEE 43rd Photovoltaic Specialists Conference (PVSC)*, pp. 3632–3635, IEEE, 2016.

[178] B. M. Başol and B. McCandless, "Brief review of cadmium telluride-based photovoltaic technologies", *Journal of photonics for Energy*, vol. 4, no. 1, p. 040996, 2014.

[179] W. Shockley and H. J. Queisser, "Detailed balance limit of efficiency of p-n junction solar cells", *Journal of applied physics*, vol. 32, no. 3, pp. 510–519, 1961.

[180] H. Chou and A. Rohatgi, "The impact of MOCVD growth ambient on carrier transport, defects, and performance of CdTe/CdS heterojunction solar cells", *Journal of electronic materials*, vol. 23, no. 1, pp. 31–37, 1994.

[181] C. Szeles, "CdZnTe and CdTe materials for X-ray and gamma ray radiation detector applications", *physica status solidi (b)*, vol. 241, no. 3, pp. 783–790, 2004.

[182] G. Zha, W. Jie, T. Tan, and L. Wang, "Study of dislocations in CdZnTe single crystals", *Physica status solidi (a)*, vol. 204, no. 7, pp. 2196–2200, 2007.

[183] M. Yu and S. D. Kenny, "The energetic impact of small Cd_xTe_y clusters on cadmium telluride", *Thin Solid Films*, vol. 584, pp. 41–45, 2015.

[184] D. Ward, X. Zhou, B. Wong, F. Doty, and J. Zimmerman, "Accuracy of existing atomic potentials for the CdTe semiconductor compound", *The Journal of chemical physics*, vol. 134, no. 24, p. 244703, 2011.

[185] J. L. Cruz-Campa and D. Zubia, "CdTe thin film growth model under CSS conditions", *Solar Energy Materials and Solar Cells*, vol. 93, no. 1, pp. 15–18, 2009.

[186] N. Amin and K. S. Rahman, "Close-Spaced Sublimation (CSS): A Low-Cost, High-Yield Deposition System for Cadmium Telluride (CdTe) Thin Film Solar Cells", *Modern Technologies for Creating the Thin-film Systems and Coatings*, vol. 361, 2017.

[187] T. Chu, "Thin film cadmium telluride solar cells by two chemical vapor deposition techniques", *Solar Cells*, vol. 23, no. 1-2, pp. 31–48, 1988.

[188] B. Liu, R. F. Hicks, and J. J. Zinck, "Chemistry of photo-assisted organometallic vapor-phase epitaxy of cadnium telluride", *Journal of crystal growth*, vol. 123, no. 3-4, pp. 500–518, 1992.

[189] A. P. Thompson, H. M. Aktulga, R. Berger, D. S. Bolintineanu, W. M. Brown, P. S. Crozier, P. J. in 't Veld, A. Kohlmeyer, S. G. Moore, T. D. Nguyen, R. Shan, M. J. Stevens, J. Tranchida, C. Trott, and S. J. Plimpton, "LAMMPS - a flexible simulation tool for particle-based materials modeling at the atomic, meso, and continuum scales", *Comp. Phys. Comm.*, vol. 271, p. 108171, 2022.

[190] S. Plimpton, "Fast parallel algorithms for short-range molecular dynamics", *Journal of computational physics*, vol. 117, no. 1, pp. 1–19, 1995.

[191] S. J. Ikhmayies and R. N. Ahmad-Bitar, "Characterization of vacuum evaporated CdTe thin films prepared at ambient temperature", *Materials science in semiconductor processing*, vol. 16, no. 1, pp. 118–125, 2013.

[192] S. Lalitha, S. Z. Karazhanov, P. Ravindran, S. Senthilarasu, R. Sathyamoorthy, and J. Janabergenov, "Electronic structure, structural and optical properties of thermally evaporated CdTe thin films", *Physica B: Condensed Matter*, vol. 387, no. 1-2, pp. 227–238, 2007.

[193] G. Zeng, J. Zhang, B. Li, L. Wu, W. Li, and L. Feng, "Effect of deposition temperature on the properties of cdte thin films prepared by close-spaced sublimation", *Journal of Electronic Materials*, vol. 44, no. 8, pp. 2786–2791, 2015.

[194] M. Gloeckler, I. Sankin, and Z. Zhao, "Ieee j. photovoltaics 3, 1389 (2013)", 2013.

[195] J. Arias and G. Sullivan, "The first observation of reflection high-energy electron diffraction intensity oscillations during the growth and sublimation of CdTe", *Journal of Vacuum Science & Technology A: Vacuum, Surfaces, and Films*, vol. 5, no. 5, pp. 3143–3146, 1987.

[196] J. Dubowski, J. Wrobel, and D. Williams, "Dependence of the vacuum sublimation rate of CdTe upon crystallographic orientation", *Applied physics letters*, vol. 53, no. 8, pp. 660–662, 1988.

[197] P. Juza, W. Faschinger, K. Hingerl, and H. Sitter, "Langmuir-type evaporation of CdTe epilayers", *Semiconductor science and technology*, vol. 5, no. 3, p. 191, 1990.

[198] S. Tatarenko, B. Daudin, and D. Brun, "Sublimation mechanisms of (100) and (111) CdTe", *Applied physics letters*, vol. 65, no. 6, pp. 734–736, 1994.

[199] H. Neureiter, S. Schinzer, W. Kinzel, S. Tatarenko, and M. Sokolowski, “Simultaneous layer-by-layer and step-flow sublimation on the CdTe (001) surface derived from a diffraction analysis”, *Physical Review B*, vol. 61, no. 8, p. 5408, 2000.

[200] M. Berding, S. Krishnamurthy, and A. Sher, “Surface energies for molecular beam epitaxy growth of HgTe and CdTe”, *Journal of Vacuum Science & Technology B: Microelectronics and Nanometer Structures Processing, Measurement, and Phenomena*, vol. 9, no. 3, pp. 1858–1860, 1991.

[201] A. Patrakov, R. Fink, K. Fink, and B. Engels, “Model computations for Cd adsorption on the (001) surface of CdTe”, *physica status solidi c*, vol. 4, no. 9, pp. 3191–3203, 2007.

[202] A. E. Patrakov, R. F. Fink, K. Fink, T. C. Schmidt, and B. Engels, “Density-functional study on the migration of Cd and Te adsorbates on the (001) surface of CdTe”, *physica status solidi (b)*, vol. 247, no. 4, pp. 937–944, 2010.

[203] F. Pietrucci, G. Gerra, and W. Andreoni, “CdTe surfaces: Characterizing dynamical processes with first-principles metadynamics”, *Applied Physics Letters*, vol. 97, no. 14, p. 141914, 2010.

[204] G. M. Torrie and J. P. Valleau, “Nonphysical sampling distributions in monte carlo free-energy estimation: Umbrella sampling”, *Journal of Computational Physics*, vol. 23, no. 2, pp. 187–199, 1977.

[205] E. K. Grimmelmann, J. C. Tully, and E. Helfand, “Molecular dynamics of infrequent events: thermal desorption of xenon from a platinum surface”, *The Journal of Chemical Physics*, vol. 74, no. 9, pp. 5300–5310, 1981.

[206] K. A. Fichthorn and R. A. Miron, “Thermal desorption of large molecules from solid surfaces”, *Physical Review Letters*, vol. 89, no. 19, p. 196103, 2002.

[207] D. Martrou, J. Eymery, and N. Magnea, “Equilibrium shape of steps and islands on polar II-VI semiconductors surfaces”, *Physical review letters*, vol. 83, no. 12, p. 2366, 1999.

[208] D. Perez, B. P. Uberuaga, and A. F. Voter, “The parallel replica dynamics method–coming of age”, *Computational Materials Science*, vol. 100, pp. 90–103, 2015.

Appendix A

Lammps scripts and python codes

A.1 Rotational matrix for random orientation of Te$_2$ dimer before deposition

We want to select orientation with equal probability in terms of solid angle. $\int \sin\theta d\theta = \int d\xi$, where ξ is uniform random number between 0 and 1.

$-\cos\theta = \xi$

$\theta = \cos^{-1}(\xi)$ for $0 => \frac{\pi}{2}$

$\int d\phi = \int d\xi'$

$\phi = 2\pi(\xi')$

The rotational matrix about z-axis with any arbitrary angle ϕ

$$R_z(\phi) = \begin{pmatrix} \cos\phi & -\sin\phi & 0 \\ \sin\phi & \cos\phi & 0 \\ 0 & 0 & 1 \end{pmatrix} \tag{A.1}$$

Rotational matrix about y-axis with any arbitrary angle θ', where $\theta' = \pi/2 - \theta$

$$R_y(\theta^{'}) = \begin{pmatrix} \cos\theta^{'} & 0 & -\sin\theta^{'} \\ 0 & 1 & 0 \\ \sin\theta^{'} & 0 & \cos\theta^{'} \end{pmatrix} \tag{A.2}$$

Then, $M_R = R_z(\phi) \times R_y(\theta^{'})$

$$M_R = \begin{pmatrix} \cos\phi\sin\theta & -\sin\phi & -\cos\theta\cos\phi \\ \sin\phi\sin\theta & \cos\phi & -\cos\theta\sin\phi \\ \cos\theta & 0 & \sin\theta \end{pmatrix} \tag{A.3}$$

If the initial position of atom is along x-axis

$$X = r\begin{pmatrix} 1 \\ 0 \\ 0 \end{pmatrix} \tag{A.4}$$

where r is the arbitrary distance from the axis of rotation. After the random rotation the new position is :

$X^{'} = M_R X$

$x = r\sin\theta\cos\phi$

$y = r\sin\theta\sin\phi$

$z = r\cos\theta$

$\hat{n} = (\sin\theta\cos\phi, \sin\theta\sin\phi, \cos\theta) >$ is the unit vector in direction of orientation axis of dimer.

If x_{cm}, y_{cm}, and z_{cm} are randomly chosen center of mass of the dimer above the substrate. Then

$x_1 = x_{cm} + b/2\sin\theta\cos\phi$

$y_1 = y_{cm} + b/2\sin\theta\sin\phi$

$z_1 = z_{cm} + b/2\cos\theta$

$x_2 = x_{cm} - b/2 \sin\theta \cos\phi$

$y_2 = y_{cm} - b/2 \sin\theta \sin\phi$

$z_2 = z_{cm} - b/2 \cos\theta$

Where b is the equilibrium bond length between dimer. Before doing this rotation of the dimer let's select rotation axes for velocities. The velocities of vibration are in the same direction as the axis. Let's select axes of rotation before rotating the dimer, and then rotate the velocities of vibration/rotation with the dimer. First axis is randomly chosen in y-z plane with angle $\alpha : 0 - 2\pi$

$nr1_x = 0$

$nr1_y = \sin\alpha$

$nr1_z = \cos\alpha$

$\vec{vr}1$ is paralle to $\vec{nr}2$

second rotation axis is perpendicular $\vec{nr}2 = \vec{nr}1 \times \hat{x}$

$nr2_x = 0$

$nr2_y = \cos\alpha$

$nr2_z = -\sin\alpha$

$\vec{vr}2$ is parallel to $\vec{nr}1$

We need to rotate the rotational **v**'s in the same way that x was rotated. We need to apply rotational matrix M_R to $\vec{vr}1$ and $\vec{vr}2$

$\vec{v'_{r1}} = M_R \vec{v_{r1}}$, Then

$v_{r1}(x) = -\sin\phi\cos\alpha + \cos\theta\cos\phi\sin\alpha$

$v_{r1}(y) = \cos\phi\cos\alpha + \cos\theta\sin\phi\sin\alpha$

$v_{r1}(z) = -\sin\theta\sin\alpha$

$v_{r2}(x) = -\sin\phi\sin\alpha - \cos\theta\cos\phi\cos\alpha$

$v_{r2}(y) = \cos\phi\sin\alpha - \cos\theta\sin\phi\cos\alpha$

$v_{r2}(z) = \sin\theta\cos\alpha$

A.2 Lammps script to generate fourteen layers of Cd-terminated (111) CdTe surface

```
#This lammps script generates Cd-terminated (111)CdTe surface
units metal
processors 2 2 2
atom_style atomic
dimension 3
boundary p p f
lattice custom 6.83 origin 0.1 0.1 0.1 orient x 1 1 -2 orient y -1 1 0 orient z 1 1 1 &. #Orientation for 111 surface
          a1 1.0 0.0 0.0 a2 0.0 1.0 0.0 a3 0.0 0.0 1.0 &
          basis 0.0 0.0 0.0      basis 0.0 0.5 0.5 &
          basis 0.5 0.0 0.5      basis 0.5 0.5 0.0 &
          basis 0.25 0.25 0.25   basis 0.25 0.75 0.75 &
          basis 0.75 0.25 0.75   basis 0.75 0.75 0.25
region  box block 0 10 0 10 0 12 units lattice
create_box 3 box # One extra type for depostion
group Te type 1
group Cd type 2
group adatoms type 3 #depositing atom or adatom has type 3
region substrate block 0 10 0 10 0 3.27 units lattice # For 14 layers
create_atoms  2 region substrate &
       basis 1 1 &
       basis 2 1 &
       basis 3 1 &
       basis 4 1 &
       basis 5 2 &
       basis 6 2 &
       basis 7 2 &
       basis 8 2
mass 1 0.12760300E+03
mass 2 0.11241180E+03
mass 3 0.12760300E+03
pair_style bop save
pair_coeff * * /usr/local/src/lammps/lammps-16Mar18-intelmpi/potentials/CdTe.bop.table Te Cd Cd
comm_modify cutoff 14.70
region bfix block 0 10.0 0 10.0 0 0.8 units lattice
group bfix region bfix
region isotherm block 0 10.0 0 10.0 0.8 1.75 units lattice
group isotherm region isotherm
region free block 0 10.0 0 10.0 1.8 3.25 units lattice
group free region free
region mobile block 0 10.0 0 10.0 0.8 3.25 units lattice
group mobile region mobile
compute  add mobile temp
compute_modify  add dynamic/dof yes extra/dof 0
neighbor 2.0 bin
neigh_modify delay 0 every 1 check yes
timestep 0.001
velocity all create 300 4928435 dist gaussian
fix 1 bfix setforce 0.0 0.0 0.0
fix 2 isotherm berendsen 300 300 1 5872534
fix 3 mobile nve
thermo_style custom step time atoms temp epair etotal ke pe
thermo 50
thermo_modify lost warn flush yes temp add
dump depo all custom 50 dump.Tedim1evCdter.800k.dat id type x y z vx vy vz
run 200000
write_data 111Cdterminatedsubstrate.dat
```

A.3 Lammps script to generate twelve layers of Te-terminated (100) CdTe surface

```
#This lammps script gives the 12 layers of Te terminated dimerized substrate of CdTe(100)
units metal
processors 2 3 1
atom_style atomic
dimension 3
boundary p p f
lattice custom 6.83 a1 1.0 0.0 0.0 a2 0.0 1.0 0.0 a3 0.0 0.0 1.0 &.  #Eight Basis sets for zincblende structure of CdTe
           basis 0.0 0.0 0.0       basis 0.0 0.5 0.5 &
           basis 0.5 0.0 0.5       basis 0.5 0.5 0.0 &
           basis 0.25 0.25 0.25    basis 0.25 0.75 0.75 &
           basis 0.75 0.25 0.75    basis 0.75 0.75 0.25

region  box block 0 10.0 0 10.0 0 11.7     #Creating a box
create_box 2 box
group Cd type 1
group Te type 2
region substrate block 0 10.0 0 10.0 0 2.75 units lattice
create_atoms  2 region substrate &
        basis 1 1 &
        basis 2 1 &
        basis 3 1 &
        basis 4 1 &
        basis 5 2 &
        basis 6 2 &
        basis 7 2 &
        basis 8 2
mass 1 0.12760300E+03
mass 2 0.11241180E+03
pair_style bop save
pair_coeff * * /users/PJS0245/utl0437/local/bin/lammps-potential/CdTe.bop.table Cd Te
comm_modify cutoff 14.70
region bfix block 0 10.0 0 10.0 0 0.8 units lattice #Four fixed layers
group bfix region bfix
region isotherm block 0 10.0 0 10.0 0.8 1.75 units lattice  #Four thermostat layers
group isotherm region isotherm
region free block 0 10.0 0 10.0 1.8 3.25 units lattice. #Four free layers
group free region free
region mobile block 0 10.0 0 10.0 0.8 3.25 units lattice #Eight moving layers(four thermostat + four free layers)
group mobile region mobile
compute  add mobile temp
compute_modify  add dynamic/dof yes extra/dof 0
neighbor 2.0 bin
neigh_modify delay 0 every 1 check yes
timestep 0.001
velocity mobile create 1000 8232971 dist gaussian
velocity bfix set 0 0 0
fix 1 bfix setforce 0.0 0.0 0.0
fix 2 isotherm langevin 1000 1000 1 952371
fix 3 mobile nve
thermo_style custom step time atoms temp epair etotal ke pe
thermo 10
thermo_modify lost warn flush yes temp add
#This gives the equlibrated configuration after 200 ps MD
run 200000
write_data TeMLsubstrate.dat
```

A.4 Lammps script to perform sublimation

```
#lammps script reads the equilibrated substrate and performs the MD, records the sublimated particle in the window
units metal
processors 2 3 1
atom_style atomic
dimension 3
boundary p p f
log log.sublimation append #appending all the information from log.lammps file
#Reading the substrate data file of name 'TeMLsubstrate.dat' having 12 layers of 10aX10a size
read_data /users/PJS0245/utl0437/lammps/sublimation/4M4L4FCdML1100K/Te2sublimation/TeMLsubstrate.dat
#Bond Order Potential file
pair_style bop save
pair_coeff * * /users/PJS0245/utl0437/local/bin/lammps-potential/CdTe.bop.table Te Cd
comm_modify cutoff 14.70
#Bottom four fixed layers
region bfix block 0 68.33 0 68.33 0 5.2 units box
group bfix region bfix
#Middle four thermostat layers
region isotherm block 0 68.33 0 68.33 5.25 12.85 units box
group isotherm region isotherm
#Top four free layers
region free block 0 68.33 0 68.33 12.9 22.5 units box
group free region free
#Eight (four thermostat + four free layers) moving layers
region mobile block 0 68.33 0 68.33 5.25 22.5 units box
group mobile region mobile
#Creating window layers at certain height above cutoff distance plus 1 A
region sb block 0 69.5 0 69.5 30.33 40 units box
group sublime dynamic all region sb every 1
compute ke sublime ke/atom
compute pe sublime pe/atom
compute_modify  ke dynamic/dof yes extra/dof 0
compute_modify  pe dynamic/dof yes extra/dof 0
compute  add mobile temp
compute_modify  add dynamic/dof yes extra/dof 0
neighbor 2.0 bin
neigh_modify delay 0 every 1 check yes
# 1 femto second time step
timestep 0.001
velocity all create 1000 204112 dist gaussian
fix 1 bfix setforce 0.0 0.0 0.0
#Langevin thermostat is used
fix 2 isotherm langevin 1000 1000 1 419320
#NVE ensemble is used
fix 3 mobile nve
thermo_style custom step time atoms temp epair etotal ke pe
thermo 10
thermo_modify lost warn flush yes temp add
#This records the particles if it enters into the window layer i.e if particle gets sublimated
dump vapor sublime custom 10 dump.SublimatedParticles.dat id type x y z vx vy vz c_ke c_pe
#This prints the frame in every 0.1 pico second to see the atoms sublimation
variable b loop 1 10000
label nextb
run 100
write_data Te2Sublimation.$b.dat
next b
jump script.lammps nextb
```

A.5 Python code to calculate the rate of sublimation

```
#This python code calculates the rate of sublimation for a particular temperature within a certain range of window width
import pandas as pd
import numpy as np
import math
import json
import yaml
import os
import shutil
import math
from mpmath import mp
import sys
from glob import glob
import statistics as st

def fileload(filename):
    with open(filename,"rt") as f:
      data = [[i for i in line.split()] for line in f.readlines()]
    return data

def get_constant_factor():
    KB = 8.617*10**(-5)
    T = 1000.0
    pi = 3.141592653589793
    m = 4.23779496*10**(-25)
    vel=10**10*((KB*T*1.60218*10**(-19))/(2*pi*m))**0.5 #This value we get in the unit of Angstrom/sec
    const = vel #Angstrom/s
    return const

def get_window_time(hw,b,params):
    """LAMMPS prints data in every 10 steps and time step is 0.001 ps. 1ps=>1000 stpes and it will be in 100the row in the data****1MD steps=>0.001ps***"""
    tau_old = 0; tau_in=0;tau_out=0;steps_b =0;steps_b1=0;steps_times=0
    """LAMMPS start detecting dimer if the lower atom is above 24.7 A from the top layer of bulk surface of CdTe plus 1A"""
    tau_old = params['MDsteps-sublimation'][0] #This is the MD time step when dimer enter the bottom of window
    print("MD steps when dimer reaches bottom of window:",tau_old)
    v_cm = round(params['Vzcm'][0],3) # it gets the z velocities of center of mass when the dimer enters the window
    print("Vcm:",v_cm)
    ws=abs(hw) #this is the shifting of the window height from 24.7 A
    shift_window = int(1000*ws/v_cm) # MD steps by which new window is shifted
    if(shift_window%10>=5):
        shift_window=shift_window - shift_window%10+10
    else:
        shift_window=shift_window - shift_window%10
    print("MD steps of window shift:",shift_window)
    if(hw<0):
        tau_in = tau_old-shift_window #negative when the window is lowered by certain height of original height.
    else:
        tau_in = tau_old+shift_window #This is the time when the dimer hits the bottomw of new window

    steps_b1 = int(1000*0.1/v_cm) #this is just to avoid numerical inconsitency
    if(steps_b1%10>=5):
        steps_b1=steps_b1 - steps_b1%10+10
    else:
        steps_b1=steps_b1 - steps_b1%10
    steps_times = round(b/0.1) #it helps in rounding the values not to have any numerical incosistency
```

```
    steps_b = steps_times*steps_b1#it gives the MD steps within the window of width b
    print("small steps:",steps_b1,"window size in MD steps:",steps_b,"steps_time:",steps_times,"for b:",b)
    tau_out= tau_in+steps_b #This is the MD step when the dimer leaves the window divid it by 10 gives array position
    print("MD steps when dimer eneters the bottom of window (tau_in):",tau_in,"& when it leaves the window
(tau_out):",tau_out)
    return tau_in, tau_out,v_cm

def get_avginvWR_window(params,tau_in,tau_out,s):
    iapos = int(tau_in/10) #initial position of potential in row when dimer enters the window
    fapos = int(tau_out/10)
    AvginvWR=0
    invWRA = []
    suminvWR = 0
    KB = 8.617*10**(-5)
    T = 1000
    dp=0
    delpe=0
    for j in range(iapos,fapos+1):
        delpe=float(params['PE'][j]) + 4500.0 # to make the exponential small for the size we are using
        invWR = mp.exp((-delpe*(s-1))/(s*KB*T))
        invWRA.append(invWR)
        dp=dp+1 #how  many data points we have
    for k in range(dp):
        suminvWR = suminvWR+invWRA[k]
        #print(suminvWR)
    AvginvWR = suminvWR
    #print("windosum:",AvginvWR)
    return AvginvWR

def get_avginvWR_config(params,tau_in,s,dcor_time):
    """dcor_time is given in ps. 0.001x10ps =>1 in row of data"""
    fapos = int(tau_in/10)
    iapos=int(100*dcor_time) #this gives the position in row.
    AvgconfinvWR = 0
    confinvWRA = []
    sumconfinvWR = 0
    KB = 8.617*10**(-5)
    T = 1000
    dp=0
    delpe=0
    print("decorrelation time (ps):",0.001*int(params['MDsteps'][iapos]))
    for i in range(iapos,fapos+1):#this gives the summing after decorrelation time to bottom of the window
        delpe=float(params['PE'][i]) + 4500.0 # this is to  make calculation faster
        invWR = mp.exp((-delpe*(s-1))/(s*KB*T))
        confinvWRA.append(invWR)
        dp=dp+1 #how  many data points we have
    for j in range(dp):
        sumconfinvWR = (sumconfinvWR)+(confinvWRA[j])
    AvgconfinvWR = (sumconfinvWR)
    return AvgconfinvWR

 def get_KTST(const,num_b,Denwow,Denww):
    """sum the numerator of all 100 runs and divide it by the denominaotr of each runs gives the best result"""
    ktstww = const*num_b/Denww #ksts with window in the denominator
    ktstwow = const*num_b/Denwow #ktst without window in the denominator
    return ktstww,ktstwow
```

```
def write_info(filename,s,b,ktstww,ktstwow):
    with open(filename,'w') as ft:
        #ft.write("s")
        ft.write("s")
        ft.write("\t")
        ft.write("b")
        ft.write("\t")
        ft.write("KTST(N/(N+D))")
        ft.write("\t")
        ft.write("KTST(N/D)")
        ft.write("\n")
        for i in range(len(b)):
            ft.write(str(s[i]))
            ft.write("\t")
            ft.write(str(b[i]))
            ft.write("\t")
            ft.write(str(round(ktstww[i],30)))
            ft.write("\t")
            ft.write(str(round(ktstwow[i],30)))
            ft.write("\n")

if __name__ == '__main__':
    #***********make file in run changes the following********
    dcor_time = 40 #decorrelation time in ps.
    heigt_win_shift = 0
    bmin = 0.2 #minimum value to start b (window width)
    bmax = 2.0 # maximum value for b
    db = 0.02
    #***************don't change any of the following******************

    max_value = int(bmax/db)
    b = bmin
    s=1
    b_array=[]
    AvgktstwwA=[]
    AvgktstwowA =[]
    s_array=[]

    const=get_constant_factor()
    print("constant value (Ang/sec:",const)
    dir_list = glob("../*.json")

    for i in range(0,max_value):
        KTSTww_array=[]
        KTSTwow_array=[]
        tsub_array = []
        tot_tsub = 0
        tot_ktstww=0
        tot_ktstwow=0
        print("Right now running for b:",b)

        for j in dir_list:   # This has more than 300 files for each parameters
            fnum = int(j.replace("../Results-","").replace(".json",""))
            params = fileload_json(j) #Reads the json files those have MD time and PE obtained from LAMMPS
            print("file:",j)
```

```
            #Gives the time to hit the bottom of window and time to leave window of width b
            tau_in,tau_out,vz_cm = get_window_time(heigt_win_shift,b,params)

            invWRw = get_avginvWR_window(params,tau_in,tau_out,s) #This gives reweighting funciton W-1 within
window
            invWRc = get_avginvWR_config(params,tau_in,s,dcor_time) # Reweighting function W-1 for configuration

            Denww = invWRc+invWRw #Denominator with inclusion of numerator
            Denwow=invWRc#denominator without numerator
            num_b = invWRw/b #Numerator (window) value divided by b

            ktstww,ktstwow = get_KTST(const,num_b,Denwow,Denww)
            KTSTwow_array.append(ktstwow)
            KTSTww_array.append(ktstww)

        for q in range(len(KTSTww_array)):
            tot_ktstww = tot_ktstww + KTSTww_array[q]
            tot_ktstwow = tot_ktstwow + KTSTwow_array[q]

        Avg_ktstwow = tot_ktstwow/len(KTSTwow_array)
        Avg_ktstww = tot_ktstww/len(KTSTww_array)
        print("s:",s,"b:",b,"AvgdenominatorwithoutN:",Avg_ktstww,"AvgdenominatorwithN:",Avg_ktstww)
        AvgktstwwA.append(Avg_ktstww)
        AvgktstwowA.append(Avg_ktstwow)
        b_array.append(b)
        s_array.append(s)
        b=b+db
        #To save the data
    write_info('WH0AS1.dat',s_array,b_array,AvgktstwwA,AvgktstwowA)
```